Acoustically induced spin transport in (110) GaAs quantum wells

DISSERTATION

zur Erlangung des akademischen Grades
doctor rerum naturalium
(Dr. rer. nat.)
im Fach Physik

eingereicht an der
Mathematisch-Naturwissenschaftlichen Fakultät I
Humboldt-Universität zu Berlin

von
Herr M.Sc.-Phys. Odilon D. D. Couto Jr.
geboren am 30.11.1979 in Guaxupé/Brasilien

Präsident der Humboldt-Universität zu Berlin:
Prof. Dr. h.c. Christoph Markschies

Dekan der Mathematisch-Naturwissenschaftlichen Fakultät I:
Prof. Dr. Lutz-Helmut Schön

Gutachter:

1. Prof. Dr. K. H. Ploog
2. Prof. Dr. O. Benson
3. Prof. Dr. F. Iikawa

eingereicht am: 26. Mai 2008
Tag der mündlichen Prüfung: 29. September 2008

Abstract

In this work, we employ surface acoustic waves (SAWs) to transport and manipulate optically generated spin ensembles in (110) GaAs quantum wells (QWs). The strong carrier confinement into the SAW piezoelectric potential allows for the transport of spin-polarized carrier packets along well-defined channels with the propagation velocity of the acoustic wave. In this way, spin transport over distances exceeding 60 μm is achieved, corresponding to spin lifetimes longer than 20 ns. The demonstration of such extremely long spin lifetimes is enabled by three main factors: (*i*) Suppression of the D'yakonov-Perel' spin relaxation mechanism for z-oriented spins in (110) III-V QWs; (*ii*) Suppression of the Bir-Aronov-Pikus spin relaxation mechanism caused by the type-II SAW piezoelectric potential; (*iii*) Suppression of spin relaxation induced by the mesoscopic carrier confinement into narrow stripes along the SAW wave front direction.

A spin transport anisotropy under external magnetic fields (B_{ext}) is demonstrated for the first time. Employing the well-defined average carrier momentum impinged by the SAW, we analyze the spin dephasing dynamics during transport along the [001] and [1$\bar{1}$0] in-plane directions. For transport along [001], fluctuations of the internal magnetic field (B_{int}), which arises from the spin-orbit interaction associated with the bulk inversion asymmetry of the crystal, lead to decoherence within 2 ns as the spins precess around B_{ext}. In contrast, for transport along the [1$\bar{1}$0] direction, the z-component of the spin polarization is maintained for times one order of magnitude longer due to the non-zero average value of B_{int}. The dephasing anisotropy between the two directions is fully understood in terms of the dependence of the spin-orbit coupling on carrier momentum direction, as predicted by the D'yakonov-Perel' mechanism for the (110) system.

Keywords:
semiconductor, spin transport, (110) GaAs quantum wells, surface acoustic waves

Zusammenfassung

Im Mittelpunkt dieser Arbeit stehen der Transport und die Manipulation optisch angeregter Elektronen-Spins in (110) Quantenfilmen (quantum wells, QWs) mittels akustischer Oberflächenwellen (surface acoustic waves, SAWs). Der starke räumliche Einschluss der Ladungsträger im akustisch erzeugten Potenzial erlaubt spinerhaltenden Ladungsträgertransport mit der akustischen Geschwindigkeit. Auf diese Weise wird langreichweitiger Spintransport über Distanzen $> 60\ \mu$m demonstriert, welche Spinlebenszeiten von mehr als 20 ns entsprechen. Erreicht werden diese extrem langen Spinlebenszeiten durch drei Effekte: (*i*) Der D'yakonov-Perel'-Mechanismus ist für Spins in Wachstumsrichtung von (110)-QWs in III-V-Halbleitern unterdrückt. (*ii*) Aufgrund des Typ-II piezoelektrischen Potenzials der akustischen Oberflächenwelle ist der Bir-Aronov-Pikus Spinrelaxations-Mechanismus sehr schwach. (*iii*) Der starke Einschluss der Ladungsträger in mesoskopische Bereiche stabilisiert den Spin zusätzlich.

In der vorliegenden Arbeit wird erstmals eine Anisotropie des Spintransports in einem externen Magnetfeld ($\mathrm{B_{ext}}$) nachgewiesen. Hierzu wurde die elektronische Spindynamik während des akustischen Transports entlang der [001]- bzw. $[1\bar{1}0]$-Richtung untersucht. Während des Transports entlang der [001]-Richtung führt die Präzession der Elektronenspins um das fluktuierende interne Magnetfeld ($\mathrm{B_{int}}$), das vom Fehlen eines Inversionszentrums im GaAs-Kristallgitter herrührt, zu Spinkohärenzzeiten von etwa 2 ns. Im Gegensatz hierzu ist beim Transport entlang der $[1\bar{1}0]$-Richtung die Spinrelaxation für Spins in Wachstumsrichtung um eine Größenordnung langsamer. Grund hierfür ist die endliche mittlere Größe des internen effektiven Magnetfeldes $\mathrm{B_{int}}$ für Transport entlang dieser Richtung. Die beobachtete Anisotropie in der Spindynamik für die beiden Transportrichtungen wird vollständig im Rahmen der Spin-Bahn-Kopplung und des D'yakonov-Perel'-Mechanismus beschrieben und quantitativ erklärt.

Schlagwörter:
Halbleiter, Elektronenspinrelaxation, (110) Quantenfilmen, akustischer Oberflächenwellen

Esse é o lugar onde eu deveria copiar uma frase de alguém inteligente.

Contents

List of Figures

List of Tables

Chapter 1

Introduction

This introductory chapter describes our motivation to study spin transport phenomena using surface acoustic waves (SAWs) in (110) GaAs quantum wells (QWs). We start with a brief introduction to spintronics, a broad and intensive research field devoted to the understanding and control of the spin degree of freedom in solid-state systems. In the following, we show that SAWs provide a powerful tool for transport and manipulation of carriers, as well as spins, in a variety of physical systems. In the last two sections, we comment on the special characteristics of III-V QWs oriented along the [110] direction for spin transport and, in particular, the advantages of employing them for acoustic transport. Besides basic physics interests, controllable spin transport in (110) QWs has the potential for future applications in devices based on SAW-induced spin transport.

1.1 Spintronics

The goal of spintronics is to understand the interaction between the particle spin and its environment, mostly aiming at the application of the acquired knowledge in useful devices. Fundamental studies on spintronics include investigations of spin generation, injection, transport, and manipulation. The fact that spintronics offers an opportunity for combining standard microelectronics with spin-dependent effects has recently lead to an increasing interest to this field [10, 11, 145, 151].

Some of the potential advantages of spin-based devices in comparison to charge-based ones include higher operation speeds and lower switching energies. In charge-based devices the speed is limited by the capacitance of the device and the drive current. In the case of semiconductor spintronics, the device operation relies on coherent processes, the speed limitations are given by the typical precession frequencies of the electron spins, which, in general, range from GHz to THz. For example, in order to rotate a spin by 180° at THz frequencies, an energy splitting of the order of 4 meV must be generated between the up and down spins. This energy is approximately an order of magnitude lower than the thermal energy at room temperature. The small energy differences between spin levels is, nevertheless, a benefit and a challenge for semiconductor spintronics. Thermal equilibrium cannot be relied on to keep the information 'safe', and the development of room temperature operating devices is one of the main challenges.

New ways of information processing can also be implemented using spintronics. Spin-based solid-state approaches for quantum computation provide the potential for fixing isolated quantum degrees of freedom in space, by embedding quantum dots or ions within a solid matrix, and then address those degrees of freedom optically or with small electrical contacts. This is a highly successful field of spin manipulation in semiconductors for solid-state quantum computation. For a review, see Ref. [70]. The two-level spin system has also called attention for its potential application on quantum communication [11]. The preparation of entangled pairs of qubits and the transmission of information via quantum states has focused efforts on issues like spin transport and coherence for information transmission [44]. Security of information exchange is also enhanced in such cases. Promising proposals for quantum key distribution schemes rely, in general, on the important security features provided by quantum cryptography [18]. In most of the approaches proposed for the quantum computation, communication and information security, a very small number of particles is considered. In this work, however, we focus on ensembles of spins.

Spintronic device manufacturing was boosted by the discovery of the giant magnetoresistance (GMR) [12, 19], the huge variation of electrical resistance with the magnetization. GMR enabled the development of information storage technologies based on metallic spintronic devices, such as read heads for hard disks and magnetic random access memories (MRAM). Information processing using the spin degree of freedom (not necessarily restricting the number of particles) has received considerable attention since the proposal of an electronic analog of the electro-optic modulator[1] by Datta and Das [40]. Maybe, the discovery of GMR and the Datta and Das proposal, can be considered the two spintronics headstones[2]. After them, a search for materials with intrinsic high spin polarization and/or interesting properties for applications employing spin phenomena has been witnessed. Recently, the employment of thin ferromagnetic films for injection and detection of spin polarized electrons in a Si transport channel lead to the demonstration of the first spin-FET [7, 78, 79].

Simultaneously with the materials investigations, the experimental techniques were also developed in order to accurately probe the new phenomena. With the accomplishment of time-resolved techniques [9], very long room-temperature spin-coherence times in non-magnetic semiconductors could be demonstrated [87, 88]. They were followed by the convincing demonstration of high-efficiency spin injection in semiconductors from spin-polarized materials [38, 56, 104] and by coherent spin transport in semiconductors [59, 86]. Current-induced spin orientation was also demonstrated, calling the attention for potential applications employing spin manipulation without the need of external magnetic fields [85, 124, 127]. Rapid progress towards room-temperature effects has been seen [61], suggesting that a variety of room-temperature devices based on semiconductor spintronics may soon be possible.

1.2 Acoustically induced transport

The initial interest for applications of elastic waves in electronics was motivated by their very low propagation velocities as compared to those of electromagnetic waves. Typical elastic wave velocities in solids range approximately from 1 to 10 × 10^3 m/s. These velocities are roughly 10^5 times lower than characteristic velocities for electromagnetic waves. As a result of the much smaller wavelength for a given frequency, an elastic wave resonator is typically 10^5 times smaller than an electromagnetic wave resonator for the same frequency. The typical size of acoustic resonators for the MHz-GHz frequency range used in common electronic devices lies in the micrometer

---

[1] Generally called the Datta-Das spin transistor.

[2] The term magnetoelectronics is often used by some authors for the spin-related phenomena in metals, while spintronics is left for semiconductors. Other authors use the term equivalently for both areas.

range. Acoustic filters and resonators can, therefore, be easily fabricated with dimensions comparable to those of the electronic components.

The pioneering work of Lord Rayleigh on waves propagating along solid surfaces was motivated by earth tremor studies [111]. The advantage of such waves in comparison to bulk waves for electronic applications is the compatibility with planar electronic structures. The constraint of being at the surface means that one can generate and detect SAWs using electrodes deposited on the surface and that one can alter the wave velocity or propagation direction with surface treatments involving deposited layers.

The surface propagation also opens the way for using acoustic waves for the modulation of planar solid-state systems. In nanostructured systems, the electric and strain fields associated with the SAW have been successfully used to modulate structures situated on or just below the surface like quantum wells [120], quantum wires [4, 123], and quantum dots [83]. The moving character of the acoustic fields has been applied to transport excitations in nanostructures. Acoustic charge transport dates from the 80's [76, 137]. The introduction of optical techniques to probe acoustic transport allowed for a precise analysis of carrier dynamics via the conversion of photons into carriers and the subsequent retrieval of information via the detection of the luminescence emitted due to carrier recombination [113, 114]. This tool was extremely important in studies of acoustically induced ambipolar carrier [113, 120], spin [129], and exciton transport [116] in quantum wells.

In the field of spintronics, proposals for devices based on acoustic transport for quantum computation have been considered for potential future applications [14, 60, 64]. The demonstration of acoustically-induced spin transport [129] was followed by the achievement of long-range spin transport in (001) QWs [132]. In the latter, interference between two acoustic beams was employed to induce carrier confinement into dynamic quantum dots, which allowed for the demonstration of spin transport over distances of approximately 100 μm. Spin manipulation during acoustic transport using external magnetic fields provided a feasible platform for spintronics applications.

1.3 (110) quantum wells

The general interest for spin manipulation in (110) QWs based on III-V semiconductors started after the prediction of very long spin lifetimes for these structures [47, 54]. The spin-orbit coupling associated with the bulk inversion asymmetry, which, in general, provides an important channel for spin relaxation in III-V semiconductors was predicted to be suppressed for spins parallel to the growth direction of (110) QWs. Several experiments have confirmed these predictions [45, 82, 105]. Spin lifetimes of a few nanoseconds were demonstrated, which are one order of magnitude longer than the ones achieved in (001) counterparts [39, 102].

At low temperatures, the spin lifetimes in (110) QWs appeared to be limited by spin scattering due to the electron-hole interaction [105]. Different approaches to overcome this limitation were developed and spin lifetimes up to 10 ns have been demonstrated [1]. Following the general trend of spintronics, rapid advance towards room temperature has been observed. Gate control of spin memory in GaAs QWs at high temperature (170 K) [82] was followed by room-temperature control of the electron spin in (110) InAs QWs using very low electric powers [68]. A nonmagnetic spin transistor, which explores the particular properties of (110) heterostructures, was proposed [67], calling attention for potential applications employing this system.

1.4 This work

The combination of acoustically induced transport with spin phenomena in (110) QWs is then faced as a challenge with promising perspectives. The SAW piezoelectric field can be used as a mechanism for reducing the exchange interaction between optically generated electrons and holes and lead, consequently, to longer spin lifetimes, as demonstrated in (001) QWs [129]. Carrier lateral confinement by the SAW potential offers another possibility for enhancing the spin lifetimes, analogously to the effects demonstrated in dynamic quantum dots [132] and quasi one-dimensional structures [74]. These perspectives, however, depend on a number of important accomplishments. Firstly, the development of high-quality (110) structures is necessary, since ambipolar acoustic transport requires a high degree of structural perfection. Secondly, one has to ensure the generation of strong piezoelectric fields on (110) surfaces. Calculations predict that these fields are, in general, weaker as compared to the ones associated with SAWs on (001) GaAs surfaces. High piezoelectric fields are essential for efficient carrier and spin transport.

These issues are addressed in the next six chapters of this work, which are organized as follows.

Chapter 2 briefly describes the SAW propagation dynamics in solids and, in particular, on (110) surfaces. Using a numerical procedure, we characterize the propagating acoustic modes along the in-plane [001] and $[1\bar{1}0]$ surface directions. The band gap energy modulation induced by the SAW strain and piezoelectric fields is also analyzed.

Chapter 3 discusses the most relevant spin relaxation mechanisms in undoped and symmetric (110) GaAs QWs. The description of the spin relaxation mechanisms considers the intrinsic ones, as well as the those induced by the SAW propagating fields. Firstly, spin relaxation and dephasing is discussed on the grounds of the D'yakonov-Perel' spin relaxation mechanism, which occurs due to the spin-orbit coupling associated with the bulk inversion asymmetry of the GaAs matrix. We demonstrate how it is suppressed for spins oriented along the growth direction in (110) III-V QWs, but turns out to be important when external fields interact with the electron spins. The spin relaxation via the electron-hole exchange interaction is also discussed. Considering spin relaxation mechanisms associated with the SAW fields, we show that they occur as a consequence of the structural inversion asymmetry induced by the SAW strain and piezoelectric fields.

Chapter 4 brings the experimental procedures employed in our studies. The multilayer structure growth process is discussed, as well as the sample processing for SAW generation. The optical technique for analyzing the acoustic spin transport is also explained.

Chapter 5 presents the experimental results characterizing the acoustic spin transport in (110) QWs. We demonstrate the achievement of spin lifetimes above 20 ns, which correspond to spin transport lengths of approximately 70 μm. The role of the relevant spin relaxation mechanisms is discussed in details.

Chapter 6 addresses the spin manipulation during transport using external magnetic fields. The dephasing spin dynamics along different in-plane directions is analyzed. A spin transport anisotropy is demonstrated, which can be well understood in terms of the dependence of the spin-orbit coupling on the carrier momentum direction, as expected from the D'yakonov-Perel' dephasing process.

In *Chapter 7*, we summarize the main achievements of this work and comment on future perspectives.

Chapter 2

Surface acoustic wave on GaAs (110) surfaces

This chapter reviews the properties of Surface Acoustic Waves (SAWs) on GaAs (110) structures. We start by introducing the basic concepts of elasticity theory and their application to determine the acoustic properties of (Al,Ga)As multilayers. We will be particularly interested in the modulation properties induced by SAWs propagating along the [001] and $[1\bar{1}0]$ directions of the GaAs (110) surface, which were the directions employed for the spin transport studies. We will show that, as a consequence of the crystal symmetry, there are different propagating surface modes along these two directions, with distinct strain and piezoelectric properties. We will describe the strain fields associated with the two modes and comment on their effect on the band structure of the material. In the final section, emphasis is given to the mechanism for carrier capture and transport induced by the SAW piezoelectric potential. The effects of the acoustic fields on the electron spin dynamics are discussed in chapter 3.

2.1 Surface acoustic wave dynamics

In this section, we give a general introduction to the mathematical description of elastic wave dynamics in solids. We will present the mathematical formalism and notation used in elasticity theory to describe SAW propagation and its effects on the physical properties of the hosting material.

2.1.1 Mathematical description

From elasticity theory, the three bulk elastic eigenmodes propagating with a given wave vector $\mathbf{k}_{bulk}$ in a homogeneous solid result from the solution of the elastic wave equation for the acoustic displacement field $\mathbf{u}$, which can be stated as [115]:

$$\frac{\partial \mathrm{T}_{ij}}{\partial x_j} = \varrho \frac{\partial^2 u_i}{\partial t^2}. \tag{2.1}$$

Here, $\mathbf{T}$ is the stress tensor, ϱ the density of the medium, $x_j = x, y, z$, and u_i the particle displacement field component along the ith direction $(i, j = x, y, z)$.

If the solid is perfectly elastic and non-piezoelectric, the stress T and the strain S are related by Hooke's law:

$$\mathrm{T}_{ij} = c_{ijkl}\mathrm{S}_{kl}, \tag{2.2}$$

where c_{ijkl} are the elastic stiffness constants of the material. The strain tensor component S_{kl} is defined as:

$$\mathrm{S}_{kl} = \frac{1}{2}\left(\frac{\partial u_k}{\partial x_l} + \frac{\partial u_l}{\partial x_k}\right), \tag{2.3}$$

where u_k is the particle displacement in the kth direction.

In a piezoelectric solid, an electric field accompanies the elastic wave. Equation (2.1) has to be solved then by taking into account the piezoelectric equations of state, which can be written in the form [115]:

$$\begin{aligned} \mathrm{T}_{ij} &= c_{ijkl}\mathrm{S}_{kl} - e_{ijm}\mathrm{E}_m \\ \mathrm{D}_n &= e_{nkl}\mathrm{S}_{kl} + \varepsilon_{nm}\mathrm{E}_m. \end{aligned} \tag{2.4}$$

Here, $\mathrm{E}_m = -\vec{\nabla}\phi$ and D_n (with $m, n = x, y, z$) are the electric and electric displacement fields components, respectively, while ϕ denotes the wave piezoelectric potential. The relevant material parameters in equations (2.4) include, besides the elastic stiffness components c_{ijkl}, the piezoelectric e_{ijm} and the static dielectric ε_{nm} tensor components.

Surface acoustic waves are low-frequency acoustic phonons localized close to the surface. In an homogeneous medium, the SAW modes have a linear energy *versus* wave vector ($\mathbf{k}_{\mathrm{SAW}}$) dispersion. The solutions of equations (2.4) providing SAW eigenmodes are the ones obtained by imposing the conditions that the free surface is indeed free, i.e., zero stress components T_{iz} ($i = x, y, z$), as well as continuity of the normal component of the dielectric field D_z across the surface [80]. In case of layered structures, the procedure is extended by imposing these conditions at the interfaces between the constituent layers. The continuity of the stress and electrical displacement at the interface at $z = z_{\mathrm{int}}$ between two adjacent layers grown along the z-direction can be expressed as:

$$\begin{aligned} \mathrm{T}_{iz}(z_{\mathrm{int}}^{+}) &= \mathrm{T}_{iz}(z_{\mathrm{int}}^{-}), \\ D_z(z_{\mathrm{int}}^{+}) &= D_z(z_{\mathrm{int}}^{-}), \end{aligned} \tag{2.5}$$

where $i = x, y, z$ and ($^{+}$) indicates that the corresponding quantity is evaluated at the layer located at $z > z_{\mathrm{int}}$ and ($^{-}$) at $z < z_{\mathrm{int}}$, respectively. On the surface, the condition if fulfilled by imposing $\mathrm{T}_{iz}(z_{\mathrm{surf}}^{-}) = 0$.

Besides the boundary conditions imposed by equations (2.5), SAW modes have also to be localized near the surface. It is thus also required that the amplitude of the SAW decays to zero as $|z| \to \infty$.

2.1.2 Abbreviated notation

In acoustics, abbreviated subscripts for tensor components involved in equation (2.4) are normally introduced in order to simplify the notation. In the case of equation (2.3), the invariance of the strain under rotation of the system imposes that $\mathrm{S}_{kl} = \mathrm{S}_{lk}$. As a result, the strain tensor can be represented by a six-element column matrix rather than a nine-element square matrix. The abbreviated notation (also called engineering notation) is then defined according to Ref. [8] as:

$$\mathrm{S} = \left(\mathrm{S}_{xx},\ \mathrm{S}_{yy},\ \mathrm{S}_{zz},\ 2\mathrm{S}_{yz},\ 2\mathrm{S}_{xz},\ 2\mathrm{S}_{xy}\right)^{T}, \tag{2.6}$$

where the components S_{kl} are defined by equation (2.3).

The number of independent components of the tensors defined by equation (2.4) depends on the symmetry of the solid. In a similar way as the 3×3 strain tensor S can be represented as a 1×6 vector, the independent components of the stiffness and piezoelectric tensors can also be reduced. For the rank four stiffness tensor, the number of independent components c_{ijkl} is limited by symmetry and by thermodynamic considerations. Due to the symmetry requirement for the strain tensor, the pairs (i, j) and (k, l) of indices of the stiffness tensor can only assume six independent values. In common acoustics notation, these values are numbered from 1 to 6 according to:

$$\begin{gathered}(xx) \rightarrow 1, \quad (yy) \rightarrow 2, \quad (zz) \rightarrow 3 \\ (yz) = (zy) \rightarrow 4, \quad (zx) = (xz) \rightarrow 5, \quad (xy) = (yx) \rightarrow 6.\end{gathered}$$

c_{ijkl} can then be described by a 36 elements 6×6 tensor written in the form $c_{\alpha\beta}$.

Using thermodynamic considerations it can be further shown that $c_{ijkl} = c_{klij}$, thus reducing the number of independent components to 21. The crystal symmetry further limits the number of independent components of the stiffness tensor for each type of material [115]. Here, we are particularly interested in cubic $\mathrm{Al}_x\mathrm{Ga}_{1-x}\mathrm{As}$ layers with different composition values x. For these materials, as well as for other crystals of cubic symmetry, there are only three independent components for the stiffness tensor, which are conventionally called c_{11}, c_{12}, and c_{44}. The stiffness tensor is written in the form [115]:

$$[c_{\alpha\beta}](\mathrm{GaAs}) = \begin{bmatrix} c_{11} & c_{12} & c_{12} & 0 & 0 & 0 \\ c_{12} & c_{11} & c_{12} & 0 & 0 & 0 \\ c_{12} & c_{12} & c_{11} & 0 & 0 & 0 \\ 0 & 0 & 0 & c_{44} & 0 & 0 \\ 0 & 0 & 0 & 0 & c_{44} & 0 \\ 0 & 0 & 0 & 0 & 0 & c_{44} \end{bmatrix} \tag{2.7}$$

Throughout the numerical calculations to be described in the next section, we assume the following values for the elastic constants for GaAs (provided by ref. [8]): $c_{11} = 11.83 \times 10^{10}$, $c_{12} = 5.32 \times 10^{10}$, and $c_{44} = 5.93 \times 10^{10}$ N/m^2. The corresponding constants for AlAs (from ref. [6]) are given by 12.02×10^{10}, 5.7×10^{10}, and 5.89×10^{10} N/m^2, respectively. The density of GaAs and AlAs are $\varrho = 5316.5$ kg/m^3 [58] and $\varrho = 3760$ kg/m^3 [6], respectively. Note that the elastic constants for these two materials have very similar values. It is, therefore, reasonable to obtain the stiffness components for $Al_xGa_{1-x}As$ alloys by interpolating between the values for GaAs and AlAs.

The piezoelectric fields associated with the SAW on GaAs are normally very weak. In order to obtain higher piezoelectric fields for the transport experiments in QWs, we have deposited on top of one of our $Al_xGa_{1-x}As$ surfaces a 500-nm-thick piezoelectric ZnO layer. For the hexagonal symmetry of ZnO there are five independent elastic components: c_{11}, c_{12}, c_{13}, c_{33}, and c_{44}. The stiffness tensor has the following form [115]:

$$[c_{\alpha\beta}](\text{ZnO}) = \begin{bmatrix} c_{11} & c_{12} & c_{13} & 0 & 0 & 0 \\ c_{12} & c_{11} & c_{13} & 0 & 0 & 0 \\ c_{13} & c_{13} & c_{33} & 0 & 0 & 0 \\ 0 & 0 & 0 & c_{44} & 0 & 0 \\ 0 & 0 & 0 & 0 & c_{44} & 0 \\ 0 & 0 & 0 & 0 & 0 & \frac{c_{11}-c_{12}}{2} \end{bmatrix} \tag{2.8}$$

We adopt throughout the calculations the values of $c_{11} = 20.9 \times 10^{10}$, $c_{12} = 12.03 \times 10^{10}$, $c_{13} = 10.46 \times 10^{10}$, $c_{33} = 21.06 \times 10^{10}$, and $c_{44} = 4.23 \times 10^{10}$ N/m^2, respectively. The density of ZnO is $\varrho = 5660$ kg/m^3 [115].

The number of independent components of the rank-three piezoelectric tensor e_{ijm} is also reduced by the symmetry of the strain tensor from 27 (for an arbitrary tensor of rank three) to 18. Indeed, the last two indices j and m form a pair which can only take six distinct values represented by α. According to the abbreviated convention e_{ijm} can then be written as:

$$e_{i\alpha} = e_{ijm} \quad i = 1, 2, 3 \quad \alpha = (j, m) = 1, 2, ...6$$

The remaining number of independent components is again determined by the symmetry of the crystal unit cell. The cubic symmetry of GaAs and AlAs entails that the piezoelectric tensor for both materials has only one nonzero component e_{14}. The piezoelectric tensor has the form:

$$[e_{i\alpha}](\text{GaAs}) = \begin{bmatrix} 0 & 0 & 0 & e_{14} & 0 & 0 \\ 0 & 0 & 0 & 0 & e_{14} & 0 \\ 0 & 0 & 0 & 0 & 0 & e_{14} \end{bmatrix} \tag{2.9}$$

The values of e_{14} used in our calculations are 0.16 C/m^2 for GaAs and 0.12 C/m^2 for the AlAs. [115]

ZnO has three nonzero piezoelectric constants, namely e_{15}, e_{31}, and e_{33}, which characterize the tensor:

$$[e_{i\alpha}](\mathrm{ZnO}) = \begin{bmatrix} 0 & 0 & 0 & 0 & e_{15} & 0 \\ 0 & 0 & 0 & e_{15} & 0 & 0 \\ e_{31} & e_{31} & e_{33} & 0 & 0 & 0 \end{bmatrix} \tag{2.10}$$

The values of e_{15}, e_{31}, and e_{33} used in the numerical analysis are 0.573, 0.48, and 1.321, respectively. [115]

The static dielectric tensors for GaAs and AlAs have a single non-zero component ε_{11}, forming a diagonal matrix. The values used in the calculations are $\varepsilon_{11} = 9.73 \times 10^{-11}$ F/m for GaAs and $\varepsilon_{11} = 8.29 \times 10^{-11}$ F/m for AlAs [6]. ZnO has two non-zero dielectric tensor components, $\varepsilon_{11} = \varepsilon_{22} = 7.38 \times 10^{-11}$ F/m and $\varepsilon_{33} = 7.83 \times 10^{-11}$ F/m. [115]

2.2 SAW propagation on (110) GaAs surfaces

In this section, we determine and discuss the properties of SAW modes propagating along the [001] and [1$\bar{1}$0] directions on the (110) GaAs surface. We start by introducing the numerical procedure to determine the acoustic modes, which is based on the elasticity theory principles discussed in the last section. We then show that, due to the tetragonal symmetry of the hosting matrix, distinct acoustic modes propagate along the two main surface directions of the (110) zinc blende surface. The modes possess strain and piezoelectric fields with different distribution profiles, leading to distinct effects on the material properties, like the band gap modulation along the two propagation directions.

2.2.1 Numerical calculation of the SAW eigenmodes

For a given acoustic wave vector $\mathbf{k}_{\mathrm{SAW}}$ ($\mathrm{k}_{\mathrm{SAW}} = 2\pi/\lambda_{\mathrm{SAW}}$, with λ_{SAW} being the acoustic wavelength) there are, in general, three independent elastic modes characterized by an angular frequency $\omega_i = \mathbf{v}_i \cdot \mathbf{k}_{\mathrm{SAW}}$, where $i = 1, 2, 3$ is the mode index. The phase velocity $\mathbf{v}_i$ is specified by the ratio $\mathbf{v}_i = \sqrt{c_i/\varrho}$. The effective elastic constant c_i is a linear combination of the elastic and piezoelectric constants of the material. The phase velocity $\mathbf{v}_i$ and the displacement field for the SAW modes are obtained by solving equations (2.4) and by applying the boundary conditions [equation (2.5)] for the structure of interest. This procedure is described in detail in Ref. [130], and has been applied in Ref. [126] to obtain analytical expressions for the eigenmodes of a SAW propagating along the [011] surface direction on a (100) GaAs/$\mathrm{Al}_x\mathrm{Ga}_{1-x}\mathrm{As}$ structure containing a two dimensional electron gas (2DEG).

Throughout this work, we will calculate the acoustic properties for the specific case of a (110) GaAs/AlGaAs layer structure with an embedded QW, based on numerical solutions of equations (2.1), (2.4), and (2.5). The numerical procedure (instead of the analytical method of Ref. [126]) is required due to the complexity of the multilayer structure employed in the experiments. The calculations follow the procedures described in Refs. [6, 136]. According to this procedure, one first determines for each layer the solutions of equation (2.1) for a given angular frequency ω_{SAW} and wave vector $\mathbf{k} = (k_x, k_y, k_z)^T$. Note that the in-plane component of the wave vector $\mathbf{k}_{\mathrm{SAW}} = (k_x, k_y)^T$ is conserved throughout the layer structure. The solution within each layer can be stated as an eigenvalue problem, where the z-component of the wave vector k_z is associated with the eigenvalues and the corresponding eigenvectors are written as a four-dimensional vector $\overrightarrow{v} = (u_x, u_y, u_z, \phi^{SAW})^T$. In a second step, the coefficients of the eigenvectors $\overrightarrow{v}$ in neighboring layers are related to each other by imposing the appropriate boundary conditions for the stress and displacement fields at the interfaces between adjacent layers [equation (2.5)]. By iterating across the layer structure, the eigenvector coefficients of the layers can be related to those in the substrate. In the final step, one seeks for angular frequencies ω_{SAW} yielding surface modes, i.e., solutions which simultaneously decay in the substrate and satisfy the acoustic and electric boundary conditions at the surface. This is usually done by numerically searching for solutions within the frequency range expected for the surface modes.

For the calculation of the acoustic modes, it is convenient to use a reference frame with axes oriented along the main axes of the surface. In the case of the (110) zinc blende surface, we will use the frame defined by $\hat{x} = [001]$, $\hat{y} = [1\bar{1}0]$, and $\hat{z} = [110]$, as shown in Fig. 2.1(a). The latter can be obtained by rotating the conventional reference frame, i.e., the one with axes defined by $\hat{x'} = [100]$, $\hat{y'} = [010]$, and $\hat{z'} = [001]$ [shown in Fig. 2.1(b)], by using the appropriate Euler angles (φ, θ, ψ). These angles describe clockwise sequential rotations of the main frame around the crystal directions defined by the $\hat{z}'$, $\hat{y}'$ and again $\hat{z}'$ axes, respectively. The first rotation is performed by an angle $\varphi \in [0, 2\pi]$ around the $\hat{z}'$ axis. The reference frame obtained after the first rotation is then rotated around $\hat{y}' \parallel [010]$ by an angle $\theta \in [0, \pi]$. The third clockwise rotation by $\psi \in [0, 2\pi]$ is performed around the direction defined by $\hat{z}' \parallel [001]$ after the previous two rotations[1]. In the rotated frame of Fig. 2.1(a), the z-axis is parallel to the growth direction, i.e., the [110] direction. The in-plane directions ($\hat{x}$ and $\hat{y}$) can be chosen to match the propagation direction of interest for the acoustic waves. Such a rotated frame is obtained from the one in Fig. 2.1(b) by using the angles $\varphi = \pi$, $\theta = \pi/2$, and $\psi = \pi/4$.

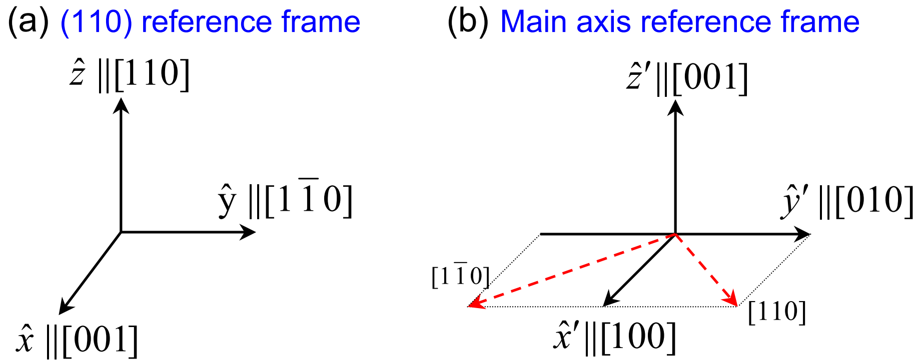

Figure 2.1: (a) Rotated reference frame oriented along the main axes of the (110) zinc blende surface. (b) Conventional reference system for GaAs/AlGaAs cubic crystal structures.

It is important to remark that equations (2.1) and (2.4) are general, i.e., they apply independently on the choice of the coordinate system. The tensors describing the material parameters, however, depend on the chosen set of axes. Therefore, when the reference frame rotation is performed, the stiffness, piezoelectric, and dielectric tensors have to be transformed to the new reference frame. The new components can be written in the abbreviated notation in terms of the tensor components of equations (2.7) through (2.10), following the procedure described in Refs. [23, 24].

The sample structure used in the calculations, containing an 18 nm-thick GaAs QW with $Al_{0.3}Ga_{0.7}As$ barriers, is presented in Table 2.1. This struc-

---

[1] Note, however, that different authors may use different sets of angles to describe the rotations, or different notations for the same angles. Therefore, a reference frame rotation employing Euler angles should always be preceded by their definition.

ture is slightly simplified in comparison to the real multilayer structure of sample A used in the experiments[2], which will be described in Chapter 4. A set of $\mathrm{Al}_x\mathrm{Ga}_{1-x}\mathrm{As}$ alloy layers in the real structure of the sample, composed of a short-period GaAs/AlAs superlattice with 20 repetition periods, was replaced in the calculation by an homogeneous 112 nm-thick $\mathrm{Al}_{0.15}\mathrm{Ga}_{0.85}\mathrm{As}$ layer with the same average composition x, as shown in Table 2.1. This simplification is not expected to affect the results obtained from the calculations, since the composition of the layers is very similar and no changes in the acoustic properties of the (110) GaAs/$\mathrm{Al}_x\mathrm{Ga}_{1-x}\mathrm{As}$ structure are expected. We also included in Table 2.1 a 500 nm-thick piezoelectric ZnO film, which was deposited on the surface of sample A after the epitaxial growth. The calculations were carried out for a SAW with wavelength $\lambda_{\mathrm{SAW}} = 5.6\ \mu$m and an acoustic linear power density $P_l = 200$ W/m. The latter is a typical value for the acoustic power employed in the experiments to be discussed later. P_l is defined as the total acoustic power flow per unit length across the SAW beam.

Material	**Thickness (nm)**
ZnO	500
GaAs	10
$\mathrm{Al}_{0.1}\mathrm{Ga}_{0.9}\mathrm{As}$	370
$\mathrm{Al}_{0.3}\mathrm{Ga}_{0.7}\mathrm{As}$	10
GaAs	**18 (QW)**
$\mathrm{Al}_{0.3}\mathrm{Ga}_{0.7}\mathrm{As}$	30
$\mathrm{Al}_{0.15}\mathrm{Ga}_{0.85}\mathrm{As}$	112
GaAs	310

Table 2.1: (110)-oriented multilayer structure used in the calculation of the SAW propagation modes containing a 18 nm wide GaAs QW with $\mathrm{Al}_{0.3}\mathrm{Ga}_{0.7}\mathrm{As}$ barriers. The ZnO film was deposited on the III-V surface after MBE growth.

In the sample reference frame shown in Fig. 2.1(a), the SAW propagating along the $\hat{x} \parallel [001]$ direction is described by a wavevector $\mathbf{k}_{\mathrm{SAW}} = (k_x, 0)^T$ while the SAW along the $\hat{y} \parallel [1\bar{1}0]$ has $\mathbf{k}_{\mathrm{SAW}} = (0, k_y)^T$. Figure 2.2 shows the dispersion for these two SAW modes calculated for the multilayer structure

---

[2] Another sample (B) with a similar structure was also studied. However, since most of the experimental results presented in this work concern to sample A, and no new physical aspect is gained by rigorously considering the structure of sample B, we decided to concentrate the calculations on the structure described in Table 2.1.

presented in Table 2.1. The dispersion curves are approximately linear with a slightly higher propagation velocity for a SAW propagating along $\hat{y}$ than along $\hat{x}$. For the SAW wavelength $\lambda_{\mathrm{SAW}} = 5.6\ \mu$m, the calculated acoustic propagation velocities along $\hat{x}$ and $\hat{y}$ are $v_x = 2905.7$ m/s and $v_y = 3301$ m/s, respectively.

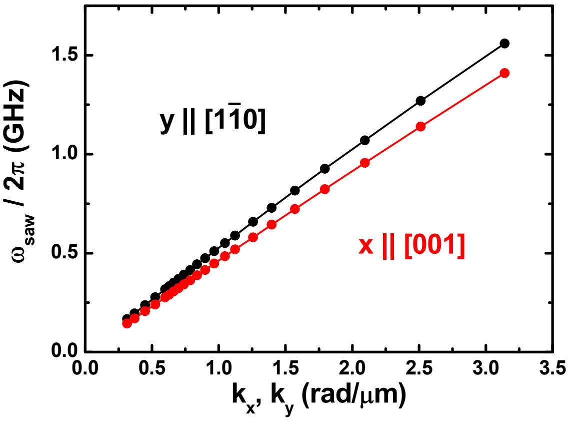

Figure 2.2: Linear dispersion calculated for the surface acoustic modes along the $\hat{x} \parallel [001]$ and $\hat{y} \parallel [1\bar{1}0]$ directions of the (110) QW structure described in Table 2.1

2.2.2 Propagation along the [001] direction

The SAW mode propagating along the [001] direction of a GaAs (110) surface is a Rayleigh mode [23]. Rayleigh SAWs consist of a superposition of a longitudinal acoustic (LA) mode with a transverse acoustic ($\mathrm{TA_z}$) one polarized perpendicular to the surface, leading to a displacement field $\mathbf{u}$ with components $\mathbf{u}_R = (u_x, 0, u_z)^T$, as illustrated in Fig. 2.3(a). In general, the amplitudes of the two displacement components u_x and u_z decrease with depth at different rates. The spatial distribution of the vertical component u_z calculated for a SAW propagating along the [001] direction of the structure in Table 2.1 is displayed in Fig. 2.3(b). For this wave, $u_z \gg u_x$. As shown in the figure, the amplitude of the vertical displacement reaches about 1 nm at the surface and decays away from it, with a decay length of approximately $\lambda_{\mathrm{SAW}}/2$.

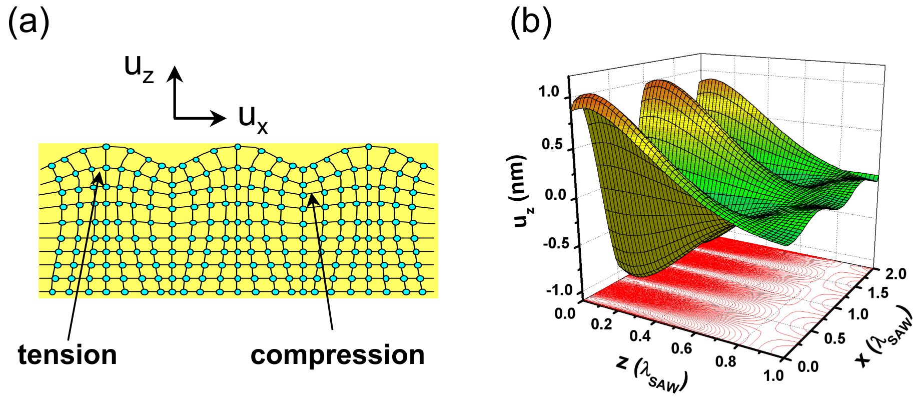

Figure 2.3: (a) Characteristic particle displacements fields u_x and u_z of a Rayleigh SAW. (b) Profiles for the vertical displacement u_z along the z direction for the Rayleigh wave propagating along the [001] direction of the (110) oriented multilayer structure depicted in Table 2.1. The calculation was performed for $\lambda_{\mathrm{SAW}} = 5.6\ \mu$m and $P_l = 200$ W/m.

2.2.3 Propagation along the $[1\bar{1}0]$ direction

The SAW mode which propagates along the $[1\bar{1}0]$ direction of the (110) surface is a Bleustein-Gulyaev wave, which consists essentially of a horizontally polarized shear wave having no displacement component perpendicular to the surface [21, 23, 65]. The displacement pattern for this mode is illustrated in Fig. 2.4(a). In the sample reference system, this wave is described by a displacement vector given by $\mathbf{u}_{BG} = (u_x, 0, 0)^T$. The component u_x oscillates along the propagation direction $\hat{y}$ and decays away from the surface with a longer decay length than the one for the Rayleigh wave component u_z propagating along the [001] direction. As shown in the profile in Fig. 2.4(b), the magnitude of the transverse displacement u_x can reach about 1 nm at the surface and is thus comparable to the surface vertical displacement u_z of the Rayleigh SAW in Fig. 2.3(b). The decay length of u_x, however, approaches $2\lambda_{\mathrm{SAW}}$.

2.3 Band structure modulation by SAWs

2.3.1 Strain field

The periodic particle displacement induced by a mechanical wave also gives rise to a modulation of the propagating strain field, as defined by equa-

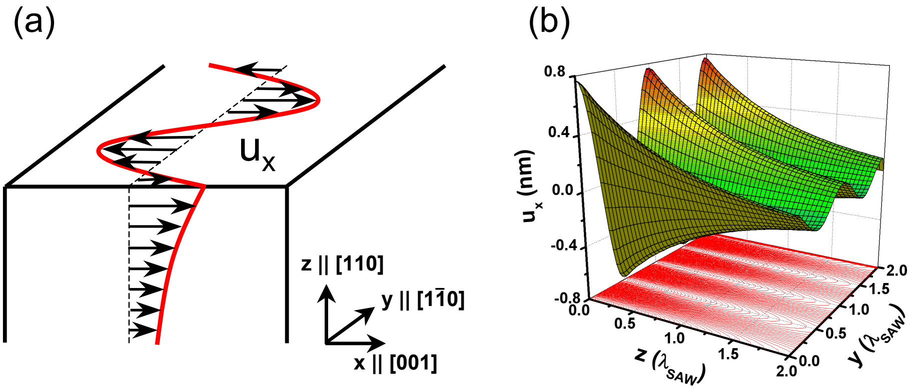

Figure 2.4: (a) Particle displacement field u_x for a Bleustein-Gulyaev SAW propagating along the $[1\bar{1}0]$ direction of the (110) GaAs surface. (b) Calculated depth dependence of u_x with $P_l = 200$ W/m for the multilayer structure presented in Table 2.1.

tion (2.3). This is illustrated in Fig. 2.3(a), which shows the lattice vertical displacement modulation by the Rayleigh wave. The spatial modulation of the strain leads to a periodic modulation of the band structure of the underlying material [42, 120]. The deformation potential modulation of the band gap E_g is caused by local variations of volume and symmetry of the crystal lattice induced by the strain field. In general, E_g reduces in the regions where the crystal is under tension and increases where the crystal is compressed, thus creating a periodic band gap modulation along the propagation direction of the SAW.

The (110) surface has two SAW modes with different symmetries propagating along the [001] and $[1\bar{1}0]$ in-plane directions. It is, therefore, expected that the propagating strain fields [given by equation (2.6)] will have different effects on the band gap of the underlying material. The strain field for the Rayleigh wave propagating along the $\hat{x} \parallel [001]$ direction, with the two component displacement vector $\mathbf{u}_R = (u_x, 0, u_z)^T$, has three non-zero components. Using the abbreviated notation, the strain field S_R can be written as:

$$\mathrm{S}_R = (S_{xx},\ 0,\ S_{zz},\ 0,\ 2S_{xz},\ 0)^T\,, \tag{2.11}$$

where the zero components appear because $u_y = \partial u_x/\partial y = \partial u_z/\partial y = 0$.

In contrast, the displacement field $\mathbf{u}_{BG} = (u_x, 0, 0)^T$ for the Bleustein-Gulyaev wave propagating along the $\hat{y} \parallel [1\bar{1}0]$ direction has only one non-vanishing component. In the sample reference frame, the strain field S_{BG} for this wave has only two non-zero components given by:

$$\mathrm{S}_{BG} = (0,\ 0,\ 0,\ 2S_{xz},\ 0,\ 2S_{xy})^T \,. \tag{2.12}$$

The band-edge states of the conduction (CB) and valence (VB) bands have different symmetries and, accordingly, respond in different ways to the acoustic field. The CB states are s-like and primarily sensitive to the volume changes introduced by the hydrostatic strain component $S_0 = S_{xx}+S_{yy}+S_{zz}$. The shift in the CB energy is given by $\Delta E_{\mathrm{CB}} = a_{\mathrm{CB}} S_0$, where a_{CB} is the hydrostatic CB deformation potential. The VB states are also modified by S_0. In general, however, the energy shifts of the VB are much smaller than the ones for the CB for most semiconductors due to the smaller values for the hydrostatic deformation potential of this band. The VB states are also sensitive to uniaxial strain components, which change the energy and mix heavy-hole (*hh*) and light-hole (*lh*) levels. In the case of the strain modulation induced by a Rayleigh SAW, the energy shift due to strain can be written as [42]:

$$\Delta E_g = (a_{\mathrm{CB}} + a_{\mathrm{VB}})\, S_0 \pm b_{\mathrm{VB}} \left(\mathrm{S}_{zz} - \frac{\mathrm{S}_{xx}}{2} \right), \tag{2.13}$$

where the deformation potential of the conduction band a_{CB} is typically about ten times larger than a_{VB}, the hydrostatic deformation potential of the valence band [149]. The signs + and - apply for *hh* and *lh* states, respectively. The VB uniaxial deformation potential b_{VB} accounts for the mixing between the *hh* and *lh* states. For QWs, the second term of equation (2.13) becomes relevant only at very high acoustic powers, when the strain-induced shifts become comparable to the splitting between the *hh* and *lh* levels associated with the confinement.

Since the CB modulation is mainly affected by S_0, the band gap modulation should be small for the Bleustein-Gulyaev waves where S_0 vanishes [compare equations (2.11) and (2.12)]. In this case, the band modulation becomes dominated by shear strain components, which do not affect the CB. The calculation of the band gap modulation in our multilayer structure will be presented in the next subsection, where we discuss the transport mechanisms and the effects of the SAW piezoelectric field.

2.3.2 Piezoelectric field

The moving piezoelectric field which follows the strain plays a key role in the carrier capture and transport processes. In this subsection, we will discuss the distribution of piezoelectric fields in our sample and show how these fields can be enhanced by coating the sample with a piezoelectric ZnO layer.

Like the strain field, the SAW piezoelectric potential ϕ^{saw} is modulated along the SAW propagation direction. This field induces a type-II potential modulation of the band edges, which spatially separates optically generated electrons (e) and holes (h) and traps them in the maxima and minima of ϕ^{saw}, respectively. Figure 2.5 illustrates the type-II modulation created by the piezoelectric field after the optical excitation of electrons and holes with energy $\hbar\omega$. The spatial separation reduces the overlap between the electron and hole wavefunctions, thus increasing the carrier lifetimes. Long lifetimes allow for long acoustic transport distances.

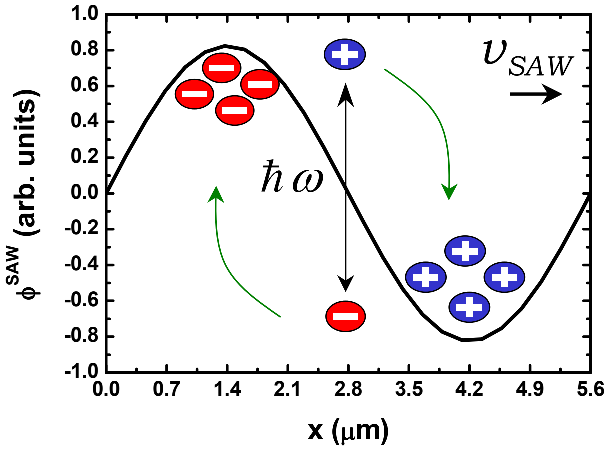

Figure 2.5: Carrier transport mechanism: the SAW piezoelectric field induces a moving type-II potential modulation, spatially separating the optically generated carriers (electrons are denoted by '-' and holes by '+'). $\hbar\omega$ corresponds to the photon energy used to excite the electron to the CB.

The transport efficiency can be discussed by analyzing the amplitude of ϕ^{saw} in the QW, which determines the carrier confinement into the SAW potential during transport. Figure 2.6(a) shows the depth dependence of ϕ^{saw} for the Rayleigh SAW propagating along [001], as well as for the Bleustein-Gulyaev wave propagating along the $[1\bar{1}0]$ direction. The profiles were calculated for the multilayer structure presented in Table 2.1 excluding the ZnO top layer. The QW positioned at a depth of z = 399 nm is indicated. For a Rayleigh wave with $P_l = 200$ W/m, the amplitude of ϕ^{saw} reaches 8 mV at this position. The amplitude of ϕ^{saw} for the Bleustein-Gulyaev SAW along the $\hat{y} \parallel [1\bar{1}0]$ direction is, in contrast, negligible. Figure 2.6(b) shows the effect introduced by the 500 nm-thick ZnO layer on the depth dependence of ϕ^{saw} for the two acoustic modes. Comparing the potential amplitude of the Rayleigh wave with the one presented in Fig. 2.6(a), we see that the introduction of the piezoelectric layer on top of the GaAs surface increases considerably the amplitude of the SAW potential in the QW, now situated at z = 899 nm. ϕ^{saw} reaches 400 mV in the QW under the piezoelectric layer, corresponding to an enhancement of approximately 50 times. In other words, since the SAW wavelength is previously determined, more intense piezoelectric fields associated with ϕ^{saw} are obtained under the ZnO. The potential amplitude for the Bleustein-Gulyaev is also increased, achieving approximately 80 mV in the QW. As we will show in chapter 6, the higher amplitudes for the piezoelectric field under the ZnO for the two acoustic modes leads to a higher transport efficiency along the [001] direction.

From these results, we also expect that optically generated carriers will live longer in the presence of the ZnO film due to a more effective separation of electrons and holes by the SAW piezoelectric field. Spin flip mechanisms induced by *e*-*h* interaction are also expected to be suppressed more efficiently. In chapter 5, we present the experimental results obtained in a second sample (B), which was not coated with ZnO. This sample was employed to compare and analyze the effects of the piezoelectric layer on the transport properties.

Besides a longitudinal component, which drags the carriers, the SAW also induces a transverse piezoelectric field component E_z. Strong vertical fields lead to a reduction of the band gap (and, consequently, to a red-shift of the photoluminescence (PL) emission lines) due to the Quantum-Confined Stark Effect induced by the bending of the energy bands along z [15]. Moreover, a z-oriented electric field breaks the inversion symmetry of the QW along the growth direction. As will be discussed in chapter 3 and chapter 5, symmetry breaking induces a contribution, due to spin-orbit interaction, to the effective internal magnetic field felt by moving electrons in the 2D structure. This internal magnetic field affects the spin relaxation rates. Figure 2.7 compares the profiles of E_z for the SAW modes propagating along the [001] and $[1\bar{1}0]$ directions, in the presence and absence of the ZnO layer. The vertical component of the piezoelectric field increases by a factor of approximately 20 in comparison to the bar AlGaAs surface (opened dots) for transport along the [001] direction when the ZnO is present (filled dots). Comparing the amplitudes of the two modes under the ZnO, the calculation shows that for a power density $P_l = 200$ W/m the amplitude of E_z induced by the piezoelectric layer reaches 5 kV/cm for the Rayleigh wave propagating along the [001] direction and 1 kV/cm for the Bleustein-Gulyaev wave along $[1\bar{1}0]$.

We now analyze the effects introduced by the ZnO film on the band gap modulation, as well as on the carrier distribution along this modulation. The

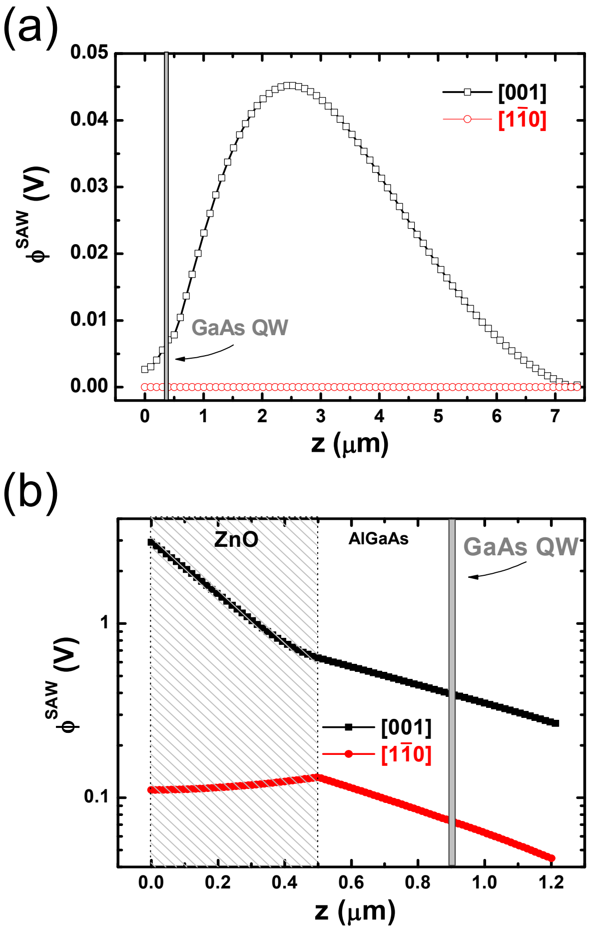

Figure 2.6: Calculated depth profiles for the piezoelectric potential amplitude ϕ^{saw} for the acoustic modes propagating along the [001] and $[1\bar{1}0]$ directions for the multilayer structure presented in Table 2.1 (a) without ZnO and (b) with the 500 nm thick ZnO film on top.

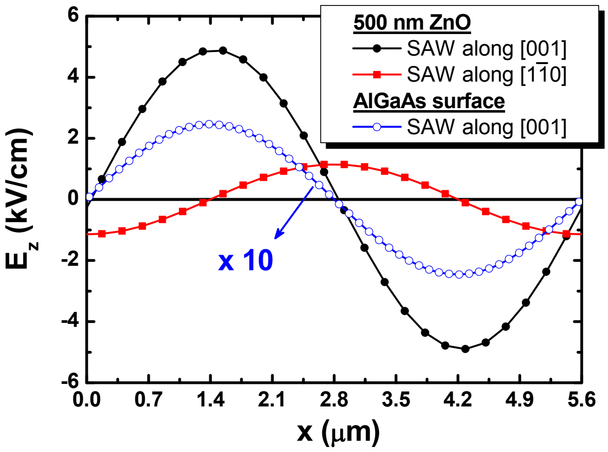

Figure 2.7: Calculations for the out-plane component E_z in one SAW cycle for propagation along the [001] (filled dots) and [1$\bar{1}$0] (squares) directions for the structure presented in Table 2.1. The same calculations performed without ZnO are presented by opened circles, where the modulation amplitude of E_z is multiplied by a factor of 10 (opened dots) for better visualization.

piezoelectric potential profiles ϕ^{saw} over one SAW cycle are displayed on the left vertical axis of both graphs in Fig. 2.8. The corresponding profiles for the band gap modulation ΔE_g due to the strain field are displayed on the right vertical axes. ΔE_g, the variation of the band gap energy, achieves its maximum (minimum) value ΔE_g^{max} (ΔE_g^{min}) in the vicinity of regions under compression (tension). The amplitudes of ϕ^{saw} and ΔE_g were calculated at the center of the QW for the Rayleigh wave along the [001] direction. This corresponds to a depth of z = 399 nm for the multilayer structure without ZnO [Fig. 2.8(a)] and of z = 899 nm in the ZnO coated structure [Fig. 2.8(b)]. The horizontal acoustic wavelength scale is defined by taking as reference the zero of the SAW phase ($\varphi_{\mathrm{SAW}} = \mathrm{k}_{\mathrm{SAW}} x - \omega_{\mathrm{SAW}} t$) at the position where ϕ^{saw}= 0 and $\partial\phi^{saw}/\partial x > 0$ for both structures.

In Fig. 2.8(a), the electrons are trapped and transported close to the positions of minimum electronic energy ($-e\phi^{saw}$) at x = $\lambda_{\mathrm{SAW}}/4 = 1.4$ μm and the holes at $3\lambda_{\mathrm{SAW}}/4 = 4.2$ μm. In this situation, ϕ^{saw} is approximately 90° dephased with respect to the band gap modulation ΔE_g. The electrons and holes are, therefore, transported in positions where the band gap modulation is close to its undisturbed value. Due to the small amplitude of ϕ^{saw} in the absence of the ZnO layer, the carriers are likely to populate a wide range of SAW phases, corresponding to a considerable energy range along the band gap modulation cycle.

The relative phase between ϕ^{saw} and ΔE_g changes when a ZnO layer is introduced on top of the structure, as shown in Fig. 2.8(b). In this case, the electrons are trapped close to the minima and the holes close to the position where the bandgap is almost undisturbed. The difference in the relative phases between band gap modulation and piezoelectric field, which depends on the presence of the ZnO, leads to a different carrier distribution along the SAW phase and, therefore, to distinct photoluminescence (PL) characteristics. In chapter 5 we will present PL spectra for different SAW power amplitudes and analyze them in terms of the field distributions depicted in

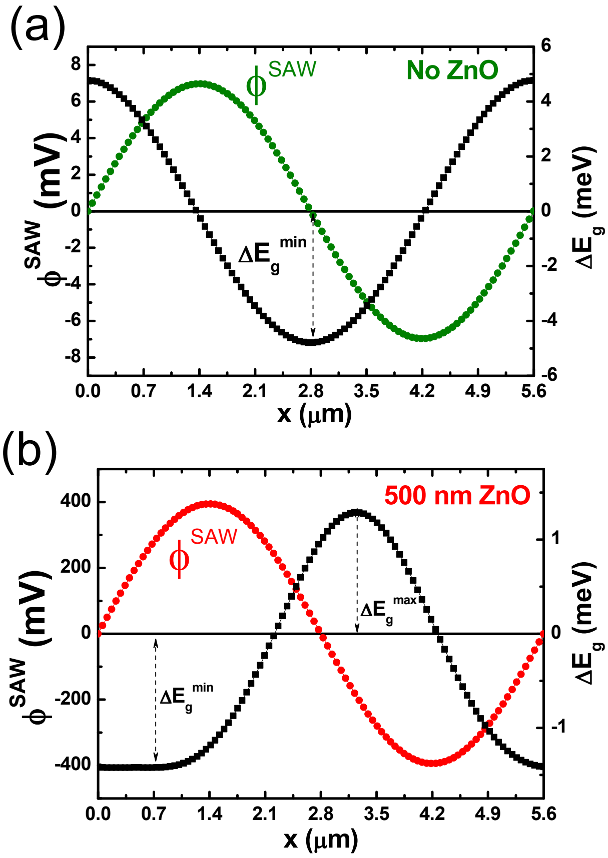

Figure 2.8: Calculated piezoelectric potential amplitude and bandgap modulation (a) in the absence and (b) presence of a 500 nm-thick ZnO layer. The relative phase between ϕ^{saw} and ΔE_g determines the occupation of carriers along one cycle of the Rayleigh SAW propagating along the [001] direction. For the calculations, $P_l = 200$ W/m.

Fig. 2.8. Note also that in the presence of the ZnO, the mixing between *hh* and *lh* states becomes considerable for $P_l = 200$ W/m. The latter leads to the flattening of the minimum energy value of the band gap modulation ΔE_g in Fig. 2.8(b) due to the interaction between the *hh* and *lh* states.

Chapter 3

Spin relaxation in (110) GaAs quantum wells

3.1 Introduction

When a non-equilibrium population of spins is excited in a physical system, the processes driving the system back to equilibrium, the so-called spin relaxation processes, are governed by the nature and strength of the interaction between the spins and the medium. In a semiconductor, the relaxation of the electron spins excited in the conduction band normally takes place through their interaction with the microscopic potential of the underlying crystal matrix, the so-called spin-orbit (SO) interaction. Electron spin interaction with other particles of the system, such as holes, phonons, impurities, or nuclear spins also lead to spin relaxation.

In this chapter, we discuss the most relevant spin relaxation mechanisms acting on a non-equilibrium population of spin-polarized electrons in a zinc-blende two-dimensional (2D) electron gas oriented along the [110] direction. We start with a general introduction to the physical origin of the SO-coupling in section 3.2. We show that, besides causing dephasing, the SO-interaction also enables the excitation of a non-zero spin polarization in the conduction band of the semiconductor by angular momentum transfer from absorbed light. The selection rules for optical transitions are valid for the excitation as well as for the recombination of spin-polarized carriers and form the basis for the so-called *optical orientation* method.

In section 3.3, the spin relaxation in symmetric (110) GaAs quantum wells (QW) is reviewed. The role played by the bulk inversion asymmetry of the III-V crystal matrix and by the exchange interaction between electrons and holes on the spin relaxation process is discussed on the basis of the D'yakonov-Perel' and the Bir-Aronov-Pikus relaxation mechanisms, respectively. Spin dephasing under external magnetic fields, discussed in section 3.4, is demonstrated to be dominated by the D'yakonov-Perel' mechanism. Attention is devoted to the dependence of the dephasing dynamics on the SO-coupling strength along different directions in the QW plane.

Besides the intrinsic spin relaxation mechanisms, we consider in section 3.5 the effects introduced by a propagating SAW on the electron spin dynamics. The propagating strain and piezoelectric fields modulate dynamically the crystal properties and are shown to add a structural inversion asymmetric contribution to the spin relaxation.

Section 3.6 summarizes the spin relaxation process discussed in this chapter and reviews the most important literature reports about spin relaxation in (110) III-V QWs.

3.2 Spin-orbit interaction

In a semiconductor, the energy dispersions $\mathrm{E}_+(\mathbf{k})$ and $\mathrm{E}_-(\mathbf{k})$ for the spin up and down states, respectively, for electrons and holes result from a combined effect of the space and time inversion symmetries of the single-particle Hamiltonian. Both symmetry operations change the wave vector $\mathbf{k}$ into $-\mathbf{k}$. Space inversion symmetry imposes that $\mathrm{E}_+(\mathbf{k}) = \mathrm{E}_+(-\mathbf{k})$. Time inversion, known as Kramer's degeneracy, also flips the spin and imposes $\mathrm{E}_+(\mathbf{k}) = \mathrm{E}_-(-\mathbf{k})$. In systems where both symmetries coexist the single-particle energies are twofold degenerate, i.e., $\mathrm{E}_+(\mathbf{k}) = \mathrm{E}_-(\mathbf{k})$.

The SO-coupling results from the interaction of moving spins with the microscopic crystal fields inside the material. It can be derived from a relativistic transformation of the crystal electric fields to the rest frame of a moving electron. In this situation, symmetry breaking is a central issue on the interaction of spins with the environment. The SO-coupling Hamiltonian, which will be defined in the next section, is invariant under time reversal [90]. Nevertheless, when the crystal potential through which the carriers move is inversion-asymmetric, the spin degeneracy is removed even in the absence of an external magnetic field. We then obtain two non-degenerate branches for the energy dispersion for carriers with momentum $\mathbf{k} \neq 0$, i.e., $E_+(\mathbf{k})$ and $E_-(\mathbf{k})$ for spins up and down, respectively. This $\mathbf{k}$-dependent energy splitting $[\Delta E_{SO}(\mathbf{k}) = E_+(\mathbf{k}) - E_-(\mathbf{k})]$ can be described as an internal magnetic field $\mathbf{B}_{\mathrm{SO}}(\mathbf{k})$, which couples to the particle spin. $\mathbf{B}_{\mathrm{SO}}(\mathbf{k})$ makes the spin degree of freedom respond to its orbital environment and, in general, leads to the relaxation of a non-equilibrium spin population.

3.2.1 Spin-splitting in quasi-2D zinc-blende semiconductors

In zinc-blende semiconductors, the SO-coupling energy splitting of the spin up and down states occurs due to the intrinsic space inversion asymmetry related to the bulk constituents of the material[1]. The splitting occurs for states in the conduction (CB) as well as valence (VB) bands [144]. Figure 3.1 illustrates schematically the non-degenerate conduction and valence bands in a 2D electron gas in the presence of the SO-coupling (the so-called split-off band is not shown). At the Γ-point ($\mathbf{k} = 0$), the heavy (*hh*) and light (*lh*) holes valence bands, whose energies coincide at the zero quasi momentum in bulk, are split due to the confinement. The energy spin splitting ΔE_{SO} of the CB characterizes the internal magnetic field $\mathrm{B}_{\mathrm{SO}} = \Delta E_{SO}/2g_e\mu_B$. As a consequence of the energy splitting, energy relaxation of non-equilibrium spin populations will be accompanied by the relaxation of the average spin of the ensemble. The splitting of the CB in Fig. 3.1 is intentionally exaggerated, since we are particularly interested in the electron spin dynamics. In general, however, the splitting is larger for the VB. The larger splittings, together with the mixing of the *hh*-*lh* states for $\mathbf{k} \neq 0$, entails very fast relaxation of the hole spins [99].

In the presence of SO-interaction, an electron with momentum $\mathbf{k}$ in the CB has its energy dispersion described by an Hamiltonian of the form [99]:

$$H = \frac{\hbar^2}{2m_0}\mathbf{k}^2 + H_{SO}(\mathbf{k}), \tag{3.1}$$

where m_0 is the electron effective mass. For GaAs, $m_0 = 0.067\ m$, where m is the free electron mass (cf. Appendix A).

The second term in equation (3.1), the SO-coupling Hamiltonian, describes the energy spin-splitting of the CB. Its general expression includes all

---

[1] Other sources of asymmetry will be discussed in the next subsection.

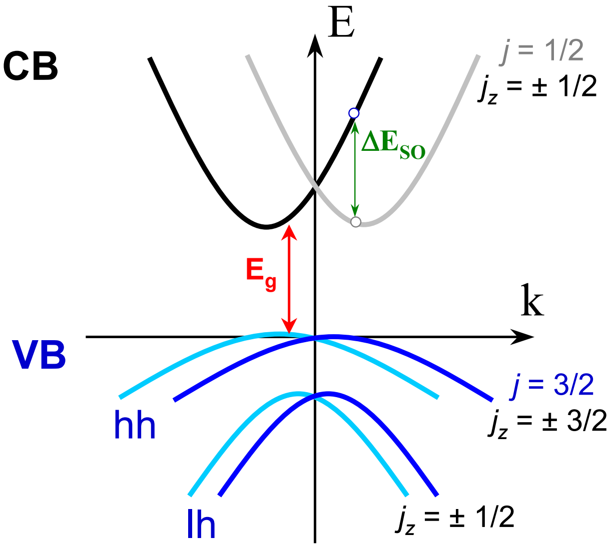

Figure 3.1: Energy splitting of the conduction (CB) and the valence (VB) bands of a quasi-2D semiconductor system when the SO-interaction is present. ΔE_{SO} is the energy splitting of the CB, which gives rise to a carrier momentum-dependent internal magnetic field $\mathbf{B}_{\mathrm{SO}}(\mathbf{k})$.

contributions to the SO spin-splitting, i.e., those arising from intrinsic crystal asymmetries as well as the ones induced by external fields, imperfections, or deformations. Consequently, $H_{SO}(\mathbf{k})$ dependents on the dimensionality of the system. Before analyzing each of the relevant contributions to our system, we make some remarks on the general form of H_{SO}. For the CB electrons, H_{SO} can always be written in the form [48]:

$$H_{\mathrm{SO}}(\mathbf{k}) = \hbar\ \Omega_{\mathrm{SO}}(\mathbf{k}) \cdot \frac{\sigma}{2}. \tag{3.2}$$

The Pauli matrices are σ_i, with $i = x, y, z$ [99]. A similar expression holds for the VB.

A comparison with the well-known Hamiltonian for the Zeeman splitting shows that $\Omega_{\mathrm{SO}}(\mathbf{k})$ can be interpreted as an effective magnetic field, in analogy to the magnetic field in the Zeeman effect, which is defined as:

$$\mathbf{B}_{\mathrm{SO}}(\mathbf{k}) = \frac{\hbar}{g_e \mu_B} \Omega_{\mathrm{SO}}(\mathbf{k}). \tag{3.3}$$

In this way, $\Omega_{\mathrm{SO}}(\mathbf{k})$ becomes the Larmor spin precession frequency associated with the internal magnetic field $\mathbf{B}_{\mathrm{SO}}(\mathbf{k})$. g_e denotes the electron g-factor and

μ_B the Bohr magneton.

3.2.2 Sources of inversion asymmetry

Three main types of asymmetry contribute to spin relaxation (determining then the $\mathbf{k}$ dependence of H_{SO}), namely the bulk inversion asymmetry, the structural inversion asymmetry and the native interface inversion asymmetry. [11, 151]

Bulk Inversion Asymmetry (BIA) is the intrinsic inversion asymmetry related to the crystal structure of the bulk material, which imposes that $\mathrm{E}_+(\mathbf{k}) \neq \mathrm{E}_+(-\mathbf{k})$. The most prominent examples of materials without inversion symmetry come from groups III-V (such as GaAs) and II-VI (like ZnSe) semiconductors, where the inversion symmetry is broken by the presence of two distinct atoms in the unit cell of the Bravais lattice. Electrons "feel", therefore, different effective magnetic fields along different crystalline directions in bulk as well as in nanostructured materials, like quantum wells.

Structural Inversion Asymmetry (SIA) refers to the asymmetry introduced by arrangements of semiconducting materials or external fields. Applying an uniform electric field even to centrosymmetric crystals immediately breaks the inversion symmetry of the potential felt by the electrons. Fluctuations in the doping density and asymmetric confinement potentials in heterojunctions also lead to SIA.

Native Inversion Asymmetry (NIA), sometimes also called *Interface Inversion Asymmetry*, refers to asymmetries induced by interfaces, like interfaces between materials with no common atoms or those whose crystal structure have BIA. Interfaces are normally asymmetric, but a compensation between upper and lower interfaces of a QW can be achieved by choosing the atomic termination plane of the upper interface, making the structure "more" symmetric. III-V QWs grown along (110) have planes of mixed anions and cations, thus vanishing the NIA contribution for this system [66]. Inhomogeneities due to interface imperfections can, however, raise contributions of NIA type to spin relaxation.

Except in the case of NIA, where a theoretical description normally depends on detailed microscopic parameters, it is possible to associate different spin relaxation mechanisms to the relevant inversion asymmetries of the system. These mechanisms, in general, have a well-defined dependence on carrier momentum $\mathbf{k}$. As we will show below, BIA yields an intrinsic contribution to spin dephasing (under external magnetic fields) in our system, while SIA can be induced by the SAW propagating fields. Due to the different efficiencies of these two effects on spin relaxation, we are able to distinguish the contributions from these asymmetries in a symmetric (110) GaAs QW. We leave for sections, 3.3, 3.4, and 3.5, the detailed discussion on this subject.

3.2.3 Selection rules and optical orientation

The generation of a non-equilibrium spin polarization can be performed by *optical orientation*, where the angular momentum of a circularly polarized light beam is transferred to the electronic system. The electron orbital momenta are directly oriented by light and, through SO-interaction, the electron spins become polarized [99]. Conversely, the polarization of the luminescence emitted by electron-hole recombination depends on the spin state of the carriers. By measuring the circular polarization of the photoluminescence (PL), it is possible to study the spin dynamics of a non-equilibrium carrier population and obtain information about the average spin orientation, the recombination time, or the spin lifetime of the carriers.

In direct band gap semiconductors, like GaAs, the selection rules for optical transitions from the uppermost valence band to the lowest conduction band can be understood in terms of the simple picture that the lowest conduction band states are *s*-like with total angular momentum $\mathrm{j} = \mathrm{l} + \mathrm{s} = 1/2$ (where l is the orbital angular momentum and s the spin), whereas the uppermost valence band hole states are *p*-like with spin $\mathrm{j} = 3/2$. Taking z as the quantization axis, the *hh* states are characterized by the z angular momentum component $\mathrm{j}_z = \pm 3/2$ while the *lh* states by $\mathrm{j}_z = \pm 1/2$. The absorption and emission of circularly polarized light require a change $\Delta \mathrm{s}_z = 1$ for transitions between the valence and conduction bands. If the incident light is left circularly polarized (σ^-), we then get the selection rules scheme depicted in Fig. 3.2. According to this scheme, the relative probability of generating an electron with spin $\mathrm{s}_z = 1/2$ in the CB ($\mathrm{l} = 0$ for the lowest CB) for a transition from the *hh* states (red arrows) is three times larger ($\mathsf{T} = 3$) than the one of generating a spin $\mathrm{s}_z = \text{-}1/2$ particle from the *lh* states ($\mathsf{T} = 1$). In this way, an excess of spin polarized carriers is excited in the conduction band. If the carrier recombination time (τ_r) is smaller than the spin relaxation time (τ_z), the emitted luminescence will be partially polarized. For normal light excitation and detection, the degree of polarization of the PL reflects the projection of the total spin vector along the z-direction. It is given by:

$$\rho_z = \frac{I_L - I_R}{I_L + I_R}, \tag{3.4}$$

where I_R and I_L are the intensities of the emitted right and left circularly polarized PL.

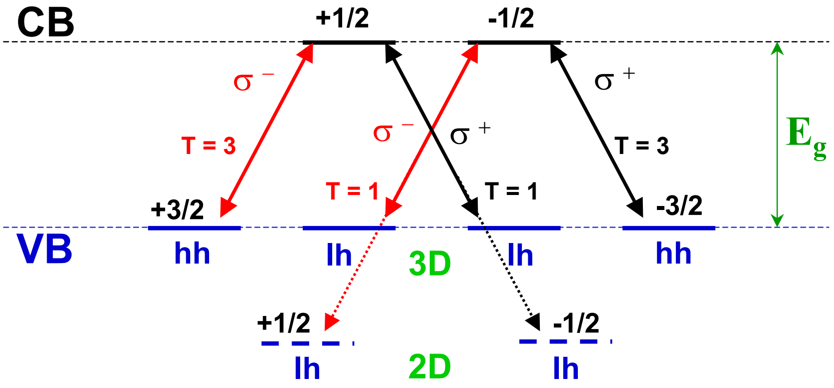

Figure 3.2: Optical selection rules at the Γ-point for 3D and 2D semiconductor systems. Due to the SO coupling, incident left circularly polarized light σ^- excites electrons with spin 1/2 with 3 times higher probability than -1/2 into the CB. The same rules hold for the recombination of the excited carriers to the ground state.

In bulk semiconductors, the degenerate *hh* and *lh* states at the Γ-point contribute with electron spin polarization of opposite signs, so that the maximum achievable degree of polarization is 0.5, or 50%. As shown in Fig. 3.2, the recombination probabilities for the luminescence (black arrows) are the same as the ones for excitation. In this way, for an excited spin polarization of 50%, we expect to obtain ρ_z =25% at the recombination[2]. This result, always valid for normal incidence, can be expressed as $\rho_z = -\rho_e/2$, where ρ_e is the electron spin polarization in the CB [49]. The minus sign means that the angular momenta of the emitted photons are directed opposite to the average electron spin. In a real situation, however, achievement of such initial high degree of spin polarization is limited by the coupling between *hh* and *lh* bands away from the Γ-point as well as by the Coulomb interaction between electrons and holes. Therefore, the measured degree of spin polarization is, in general, smaller than the expected one [108].

---

[2] It is assumed that the hole spins relax much faster then the electron ones [99].

In quasi-2D systems, the degeneracy of the *hh* and *lh* states is lifted (as indicated by the dashed energy level lines in Fig. 3.2), thus making it possible to achieve 100% of electron spin polarization by resonant excitation of the *e-hh* transition energy. Further increase of the excitation energy will lead to a contribution of opposite spin due to transitions excited from the *lh* bands and from the split-off band. [49]

3.2.4 Spin relaxation and dephasing

The *optical orientation* method allows to study the spin dynamics in semiconductors under a large variety of physical conditions, like external electric or magnetic fields, temperature, strain, etc. The spin dynamics of a spin 1/2 system is often characterized by the decay of the longitudinal and transverse spin polarization, which in literature are known as the times T_1 and T_2, respectively. In this notation, introduced in the field of nuclear magnetic resonance (NMR) [128], the longitudinal and transverse directions are defined with respect to an applied external magnetic field which causes the Zeeman splitting along the field direction. T_1, the longitudinal spin relaxation time, is the time the spin system takes to come back to equilibrium. The relaxation normally involves a change in the relative occupation of the states of the two-level system and requires energy transfer to or from the system, usually via the interaction with phonons. T_2, the transverse relaxation time, relates to the coherence (phase) relationship between the two states and, in general, does not require energy transfer. Normally, in the absence of magnetic fields or in isotropic systems, $T_1 = T_2$ [151]. For an ensemble of spins, one defines another time scale $T_2^* \leq T_2$. The latter takes into account that some spins may rotate faster than others due to spatially inhomogeneous magnetic fields for g-factors, leading to an inhomogeneous spin dephasing of the ensemble [11].

An universal definition for the quantities T_1 and T_2, appropriate for a wide diversity of physical systems and phenomena, is still source of debates [77, 151]. Throughout this work, for convenience, we will adopt the notation τ_z for the relaxation time of optically-oriented spins under normal incidence, and τ_s for the average decoherence time of the spin ensemble (which is equivalent to T_2^*), when external magnetic fields induce spin precession.

Strictly speaking, the longitudinal spin relaxation time T_1 can not be associated with changes in the state occupation, since in most cases the wavefunction of an electron under the SO-interaction cannot be factorized into the product of a purely spin component and a purely momentum component. The presence of H_{SO} Hamiltonian couples electron states of opposite spins which have the same wavevector $\mathbf{k}$ (since H_{SO} has the same period of the lattice) but different energies. Therefore, in combination with momentum scattering, the spin up and down states can couple and lead to spin relaxation. This scattering-driven decoherence is often referred to as the Elliot-Yafet (EY) mechanism [53]. Spin-flip due to momentum scattering is typically caused by impurities (at low temperatures) or phonons (at higher temperatures). Because the magnitude of the SO-interaction is, in general, much smaller than the energy separation between bands, the interband coupling can be disregarded in many cases [151].

3.3 Spin relaxation mechanisms in (110) GaAs QWs

In this section, we discuss the most relevant spin relaxation mechanisms in symmetric and undoped GaAs QWs oriented along the [110] direction. We start in subsection 3.3.1 with the description of the spin relaxation associated with the BIA, known as the D'yakonov-Perel' (DP) mechanism [48]. In III-V semiconductors, the DP mechanism is, in general, the most effective spin relaxation process. By exploring the crystal symmetry of the 2D electron gas, we show that it is possible to suppress the BIA contribution from the SO-coupling for spins oriented along the z-direction in (110) III-V QWs.

Besides the spin relaxation mechanism related to the inversion asymmetry, we consider in subsection 3.3.2 the Bir-Aronov-Pikus (BAP) mechanism [20], which accounts for spin relaxation due to the exchange interaction between electrons and holes and is, in general, very effective for photoexcited spins at low temperatures.

Other intrinsic spin relaxation mechanisms, namely the already mentioned EY mechanism or spin relaxation via hyperfine interaction, will not be discussed due to the lack of experimental evidence for their occurrence in our investigations, as well as in other similar studies. This topic will be discussed in section 3.6, where we review some of the most important studies on spin relaxation in (110) III-V QWs.

3.3.1 D'yakonov-Perel' mechanism

As we already mentioned, the D'yakonov-Perel' spin relaxation mechanism in III-V semiconductors arises from the lack of inversion symmetry of the host material. [46, 48] In contrast to the Elliot-Yafet mechanism, which describes spin relaxation due to spin-dependent scattering processes, the DP mechanism relates to spin dephasing due to random spin precession in-between scattering events. During the intervals between collisions, each electron spin precesses around the direction defined by $\mathbf{B}_{\text{int}}(\mathbf{k})$, which characterizes the internal magnetic field due to the BIA contribution to the SO-coupling. The random walk of individual spins within a spin polarized ensemble results in random changes of direction and magnitude of the momentum $\mathbf{k}$. The changes in momentum during collisions lead, in most cases, to rotation of the precession axis due to changes of the internal field $\mathbf{B}_{\text{int}}(\mathbf{k})$. This process randomizes the precession angles of individual spins in an ensemble and, consequently, entails a fast relaxation of the average spin vector. The fast spin relaxation caused by momentum fluctuations makes DP one most effective spin relaxation mechanism in systems missing bulk inversion symmetry.

In some cases, the DP dephasing can be considerably reduced by exploiting motional narrowing effects resulting from rapid momentum scattering: collisions which change the momentum of an electron faster than the precession period around the internal field retard spin relaxation. If the time between collisions is much smaller than the precession period, then the electron spin will not be able to follow the frequent rotations of the precession axis and relaxation will be suppressed. Under these conditions, the spin precession angle between scattering events $\varphi = \Omega_{\mathbf{int}}(\mathbf{k})\tau_p \ll 1$. Here, τ_p is the momentum relaxation time of the electron and $\Omega_{\mathbf{int}}(\mathbf{k})$ is the Larmor precession frequency associated with $\mathbf{B}_{\text{int}}(\mathbf{k})$. The average value $\overline{\varphi^2}$ during a time interval $t \gg \tau_p$ can be written in the form $\overline{\varphi^2} = (\Omega_{\mathbf{int}}\tau_p)^2 t/\tau_p$, where t/τ_p is the number of flips of the precession axis during time t. Defining the spin relaxation time τ_z as the time required to get $\overline{\varphi^2} \approx 1$, we obtain [49]:

$$\frac{1}{\tau_z} \approx \overline{\Omega^2_{\mathbf{int}}}\,\tau_p. \tag{3.5}$$

Here $\overline{\Omega^2_{\mathbf{int}}}$ denotes the value of $\Omega^2_{\mathbf{int}}$ averaged over the values of $\mathbf{k}$. Although equation (3.5) does not take into account details about the momentum scattering dynamics, it yields, in general, a good estimate for the spin relaxation time in the limit of high collision rates. Different approaches have been successfully used to suppress spin relaxation in GaAs structures by increasing the momentum scattering rates. Examples are the introduction of dopants [87, 118] and the confinement of spins either within mobile quantum dots [29, 132, 150] or in narrow 2D channels [74, 89, 97].

A second approach to reduce spin relaxation due to the DP mechanism explores the confinement effects in 2D systems and the symmetry of the hosting crystal matrix. To understand this approach, we firstly have to analyze the dependence of the CB spin splitting on carrier momentum. The term which describes the lack of inversion symmetry contribution to the SO-coupling Hamiltonian H_{SO} [equation (3.2)] is known as the Dresselhaus term [46]. In bulk III-V semiconductors, the Dresselhaus Hamiltonian in the vicinity of the Γ-point can be written as:

$$H_{SO}(\mathbf{k}) = \frac{\gamma}{2} \sum_i \sigma_i k'_i (k'^2_{i+1} - k'^2_{i+2}), \tag{3.6}$$

with k'_i being the wave-vector components along the principal crystal axes defined in Fig. 2.1(b). γ is the spin-splitting constant of the material. We follow here the convention introduced by Eppenga [54] and Cardona [27], which define the energy splitting due to the SO-interaction in bulk III-V semiconductors in the form $\Delta E_{SO} = \gamma k'^3$. Values for γ ranging from 16 to 28 eV$\mathring{A}^3$ for GaAs have been reported in the literature [33, 36, 46, 98, 112, 132].

Equation (3.6) shows that the internal magnetic field associated with the energy spin-splitting of the CB depends on the cube of the electron momentum $\mathbf{k}'$. This cubic dependence on carrier momentum makes DP relaxation very effective for electrons with high energies due to high temperatures or induced by optical excitation above the bottom of the conduction band.

In quasi 2D systems, the magnitude of the internal magnetic field is, in general, enhanced in comparison to the 3D case. The k'_z component of the electron momentum perpendicular to the 2D plane becomes larger because of the confinement. By averaging the SO-splitting along the growth direction $\hat{z}'$ in a QW with thickness d, one obtains a spin-splitting of the lowest 2D energy band which is proportional to $k'^2_z k'_\parallel$, where $k'_z = (\pi/d)$ and $k'^2_\parallel = k'^2_x + k'^2_y$ [48]. Note that the symmetry of the wave function along the confinement direction z' imposes zero average values for the odd terms in k'_z.

In this context, (110) oriented QWs were proposed as potential candidates for the achievement of long spin lifetimes [47, 54]. Transforming equation (3.6) to the (110)-oriented reference frame [cf. Fig. 2.1(a)], we obtain the Larmor frequency associated with the Dresselhaus Hamiltonian for the (110) system [cf. equation 3.2]:

$$\Omega_{\mathbf{int}}(\mathbf{k}) = \frac{\gamma}{2\hbar}\begin{pmatrix} 4k_x k_y k_z \\ -k_y^2 k_z - 2k_x^2 k_z + k_z^3 \\ -k_y k_z^2 - 2k_x^2 k_y + k_y^3 \end{pmatrix} \tag{3.7}$$

For the (110) 2D system, we have $\langle k_z \rangle = \langle k_z^3 \rangle = 0$ along the confinement direction. Neglecting higher order terms in $k_{||}$, we obtain following expression for the Larmor precession frequency:

$$\Omega_{\mathbf{int}}(\mathbf{k}) = -\frac{\gamma}{2\hbar}\begin{pmatrix} 0 \\ 0 \\ k_y \langle k_z^2 \rangle \end{pmatrix} \tag{3.8}$$

The internal magnetic field describing the BIA contribution to the SO-coupling can then be written as [36]:

$$\mathbf{B}_{\text{int}}(\mathbf{k}) = -\frac{\gamma}{2 g_e \mu_B} k_y \left[\frac{\pi}{d_{\text{eff}}}\right]^2 \hat{z}, \tag{3.9}$$

where we use $\langle k_z^2 \rangle = [\pi/d_{\text{eff}}]^2$, d_{eff} is the effective QW thickness, which includes the nominal QW thickness d plus the wave function penetration into the QW barriers.

The vector field pattern describing the distribution of $\mathbf{B}_{\text{int}}(\mathbf{k})$ along the (110) QW plane is illustrated in Fig. 3.3. Unlike QWs grown along [001] or [111] directions, where the internal magnetic field lies in the QW plane [54, 151], equation (3.9) shows that $\mathbf{B}_{\text{int}}$ is always parallel to the growth direction $\hat{z}$ in (110) QWs. Electron spins generated by circularly polarized light at normal incidence are also oriented along $\hat{z}$. The internal magnetic field, therefore, does not induce precession for these spins and, consequently, does not contribute to spin relaxation. Moreover, $\mathbf{B}_{\text{int}}$ depends only on the in-plane momentum component $k_y \mid\mid \hat{y}$ of $\mathbf{k}_{||}$, as illustrated in Fig. 3.3. Electron motion along $\hat{x}$ does not affect the internal field felt by the electrons.

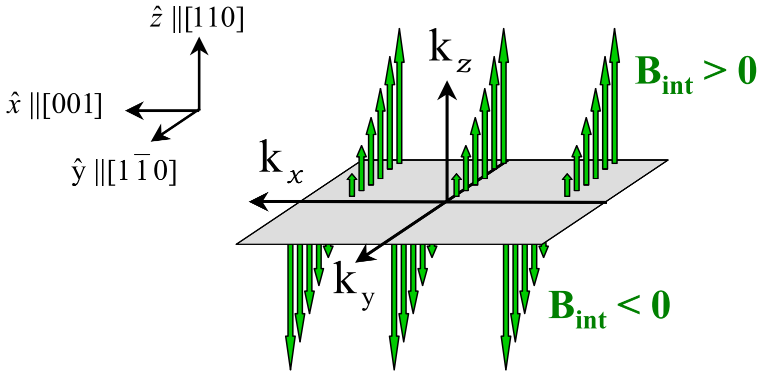

Figure 3.3: Internal magnetic field configuration in (110) QWs. $\mathbf{B}_{\mathrm{int}}$ points always along the growth direction, preserving the $\hat{z}$-component of the electron spin and avoiding fast spin relaxation.

In agreement with the expectations, much longer spin lifetimes for $\hat{z}$-oriented spins have been reported for (110) GaAs QWs [1, 36, 45, 82, 105] and (110) InAs/GaSb superlattices [66] as compared to their (001) counterparts. Nevertheless, equation (3.9) suggests that fluctuations in k_y lead to spin dephasing when in-plane spin components appear due to precession induced by external fields. Fluctuations of $\mathbf{B}_{\mathrm{int}}$ due to the linear dependence on k_y have been demonstrated to induce transversal relaxation rates one order of magnitude higher than the longitudinal ones [36, 45]. The spin dephasing dynamics under external magnetic fields and its dependence on carrier momentum direction in the QW plane will be discussed in detail in section 3.4.

3.3.2 Bir-Aronov-Pikus mechanism

Optical excitation in semiconductors inherently involves the creation of a non-equilibrium population of carriers in the valence and in the conduction band. Hence, besides spin relaxation mechanisms related to the SO-coupling, spin-flip due to the exchange interaction between electrons and holes has to be taken into account for the spin relaxation process.

There are two regimes in which the electron and hole spins can interact and lead to spin relaxation. The first one, proposed by Bir, Aronov and Pikus (BAP) [20], relates to spin-flips caused by scattering of free electrons in a sea of spin-polarized holes via the exchange interaction. This mechanism can dominate the spin relaxation process in highly p-doped materials [57]. The second regime addresses exciton spin relaxation, where the excitonic nature of the wave function plays a fundamental role in the spin scattering process. Exciton spin relaxation also belongs to the motional narrowing class and can be described by an effective internal magnetic field acting on excitons with $\mathbf{K} \neq 0$, where $\mathbf{K}$ is the exciton center-of-mass momentum [95].

A clear distinction between these two processes (BAP or exciton spin relaxation) is, in general, not straightforward and many authors do not rigorously separate both situations. In some cases, however, it is possible to determine whether electrons and holes have similar spin relaxation times, thus indicating that they are scattered simultaneously and that the excitonic spin relaxation predominates. In intrinsic GaAs QWs, excitonic spin relaxation normally dominates at low temperatures, where the electron-hole (*e*-*h*) correlation is stronger [95]. As the temperature rises, the relaxation turns to be dominated by the free-carrier spin scattering, and, in general, the electron spin lifetime becomes considerably longer than the hole one due to the stronger SO-coupling for holes and the mixing of the valence band states [39, 96].

Obviously, spin relaxation due to *e*-*h* interaction can coexist with other relaxation mechanisms. In general, the contribution arising from different mechanisms can be separated by their unique dependence on temperature and/or carrier density. For (110) GaAs QWs, where the DP mechanism is absent for z-oriented spins, it has been demonstrated that the spin relaxation at low temperatures is basically due to the excitonic interaction. Ohno and co-workers [105] showed that the spin relaxation below T = 20 K is determined by exciton spin relaxation. For higher temperatures the spin lifetimes are enhanced due to exciton dissociation.

As already discussed in the previous chapter, the mobile piezoelectric field of a SAW spatially separates electrons and holes during acoustic transport. The transport is then performed with uncorrelated electrons and holes, which is expected to suppress the BAP relaxation process [129].

3.4 Spin dephasing under external magnetic fields

Equation (3.9) shows that z-oriented spins in (110) GaAs QWs are not sensitive to the D'yakonov-Perel' relaxation mechanism. Therefore, an optically excited electron in the CB with spin polarized along the z-direction and an in-plane momentum $\mathbf{k}_{\|} \neq 0$ experiences an internal magnetic field which maintains the initial spin orientation. Under these conditions, spin relaxation is expected to be dominated by other relaxation mechanisms. The decay of the degree of spin polarization can be, in general, well described by an exponential decay of the form:

$$\rho_z(t) = \rho_0 e^{-\gamma_z t}. \tag{3.10}$$

Here, ρ_0 is the degree of spin polarization of the ensemble at $t = 0$ and $\gamma_z = \tau_z^{-1}$ the spin relaxation rate, which is determined by the strength of the involved relaxation mechanisms.

When an external magnetic field rotates the average spin vector away from the z-direction, however, the DP mechanism has to be once more considered in the (110) system. This situation is analogous to spin relaxation in (001) QWs, where the DP field is not collinear with the spin orientation direction and random fluctuations of the SO-field caused by momentum scattering lead to fast loss of the spin memory [49].

3.4.1 Spin dephasing during transport along the [001] direction

In the (110) reference frame, a Rayleigh SAW propagating along the $\hat{x} \parallel [001]$ direction imparts an average carrier momentum $\langle \mathbf{k}_{\|} \rangle = (\langle k_x \rangle, 0)$. For simplicity, we will denote it by $\langle k_x \rangle$. The carrier momentum parallel to the wave fronts ($\hat{y}$ direction), in contrast, averages to zero. This last assertion implies that the average internal magnetic field due to DP relaxation felt by the spin ensemble also vanishes, i.e., $\langle \mathbf{B}_{\text{int}} \rangle = 0$. In this situation, when an in-plane external magnetic field $\mathbf{B}_{\text{ext}}$ is present, the spin precession dynamics can be treated as a two-dimensional problem. For simplicity, we set $\mathbf{B}_{\text{ext}}$ along $\hat{y} \parallel [1\bar{1}0]$ as in the experimental configuration, so that the spin dynamics can be described by a pair of components $\mathrm{s}_x(\Omega_{\text{ext}}, t)$ and $\mathrm{s}_z(\Omega_{\text{ext}}, t)$ in the x-z plane, with spin relaxation rates γ_x and γ_z, respectively.

In optical pumping experiments, the spin lifetime $\tau_{\text{s}} = \gamma_{\text{s}}^{-1}$ is determined by the contributions from carrier recombination and spin relaxation, according to:

$$\gamma_{\text{s}} = \gamma_{\text{r}} + \gamma_{x,z} \tag{3.11}$$

where $\gamma_\mathrm{r} = \tau_\mathrm{r}^{-1}$ is the carrier recombination rate and τ_r the carrier lifetime. The spin dephasing rate associated with γ_x and γ_z is $\gamma_{x,z}$, which will be defined in the following.

Time evolution of the spin polarization

We follow the procedure described by Döhrmann *et al.* [45] to determine the time dependence of the spin polarization under a constant in-plane external magnetic field $\mathbf{B}_\mathrm{ext}$. The time evolution of the spin polarization components s_x and s_z is given by the solution of the following pair of equations:

$$\frac{\partial}{\partial t}\begin{pmatrix} \mathrm{s}_x \\ \mathrm{s}_z \end{pmatrix} = -\begin{pmatrix} \gamma_x & -\Omega_\mathrm{ext} \\ \Omega_\mathrm{ext} & \gamma_z \end{pmatrix}\begin{pmatrix} \mathrm{s}_x \\ \mathrm{s}_z \end{pmatrix} - \gamma_\mathrm{r}\begin{pmatrix} \mathrm{s}_x \\ \mathrm{s}_z \end{pmatrix} \tag{3.12}$$

The off-diagonal elements in the first term denote the spin precession around the applied magnetic field $\mathbf{B}_\mathrm{ext}$. The diagonal elements contain the in and out-of-plane relaxation rates. Finally, the second term takes into account the spin relaxation due to carrier recombination.

The solution of equation (3.12) for the z-component of the spin polarization is given by:

$$\mathrm{s}_z(\Omega_\mathrm{ext}, t) = \mathrm{s}_0 \frac{e^{-t/\tau_\mathrm{s}}}{\cos\varphi}\cos(\omega_a t - \varphi) \tag{3.13}$$

The total spin lifetime is:

$$\frac{1}{\tau_\mathrm{s}} = \frac{1}{\tau_\mathrm{r}} + \frac{1}{2}\left(\frac{1}{\tau_z} + \frac{1}{\tau_x}\right) \tag{3.14}$$

The phase angle φ and the effective Larmor frequency ω_a are defined according to:

$$\tan\varphi = \frac{\gamma_x - \gamma_z}{2\omega_a} \text{ and } \omega_a = \sqrt{\Omega_\mathrm{ext}^2 - \frac{(\gamma_x - \gamma_z)^2}{4}} \tag{3.15}$$

We expect from equation (3.13) an oscillatory behavior of the spin polarization $\mathrm{s}_z(\Omega_\mathrm{ext}, t)$ with time. The effective Larmor frequency ω_a (smaller than Ω_ext) depends on the difference between out-of-plane (γ_z) and in-plane (γ_x) spin relaxation rates.

The time and magnetic field dependence of the degree of spin polarization $\rho_z(\Omega_\mathrm{ext}, t)$ is the same one of equation (3.13) which describes the spin polarization. However, according to equation (3.4), $\rho_z(\Omega_\mathrm{ext}, t)$ does not depend on γ_r, so that the effective spin lifetime τ_eff in this case is given by:

$$\frac{1}{\tau_\mathrm{eff}} = \frac{1}{2}\left(\frac{1}{\tau_z} + \frac{1}{\tau_x}\right) \tag{3.16}$$

According to equation (3.9), the spin relaxation rates associated with the BIA for z-oriented spins in a (110) QW are expected to vanish (i.e., $\tau_z \approx \infty$). In contrast, the in-plane spin lifetimes are expected to be much shorter. Using the expression for τ_x from Ref. [151] and the relation $\gamma = \alpha\hbar^3/\sqrt{2m_0^3 E_g}$ (α is a dimensionless parameter specifying the strength of the SO-interaction of the material), we write:

$$\tau_x \approx \left[\frac{4\hbar^4}{m_0 \pi^4 \gamma^2 k_B}\right] \frac{d_\mathrm{eff}^4}{\tau_p \mathrm{T}}. \tag{3.17}$$

Here, k_B is the Boltzmann constant, τ_p the momentum relaxation time, T the temperature, and d_eff the effective QW thickness. In high-quality (110) QWs, the carrier lifetimes during diffusion have been shown to exceed several nanoseconds [45]. During acoustic transport, these lifetimes are expected to be even longer. Therefore, according to equation (3.17), the exponential decay term e^{-t/τ_s} in equation (3.13) describing the damping of the spin precession around the external magnetic field is expected to be mainly determined by τ_x.

Hanle effect

Equation (3.13) describes the time evolution of the spin polarization s_z under an external magnetic field and needs, therefore, a time-resolved experimental analysis for its verification. Information about the spin dynamics can also be obtained from time integrated luminescence measurements as a function of an external magnetic field. Here, we explore the Hanle effect [99], which describes the decay of the spin polarization of a spin ensemble induced by the application of a transverse magnetic field.

Under usual optical pumping conditions, the carrier decay rate for thermalized electrons is given by $W(t) = \tau_\mathrm{r}^{-1}\exp(-t/\tau_\mathrm{r})$. The average spin polarization is then obtained by performing the integration [99]:

$$\bar{\mathrm{s}}_z(\Omega_\mathrm{ext}) = \bar{\mathrm{s}}_0 \int dt W(t) \mathrm{s}_z(\Omega_\mathrm{ext}, t). \tag{3.18}$$

Using equation (3.13) and performing the integration in equation (3.18), we obtain:

$$\bar{\mathrm{s}}_z(\Omega_{\mathrm{ext}}) = \bar{\mathrm{s}}_0 \frac{\gamma_{\mathrm{r}}\ (\gamma_{\mathrm{r}} + \gamma_x)}{(\gamma_{\mathrm{r}} + \gamma_x)(\gamma_{\mathrm{r}} + \gamma_z) + \Omega_{\mathrm{ext}}^2}, \tag{3.19}$$

where $\bar{\mathrm{s}}_0$ is the average spin polarization at $B_{\mathrm{ext}} = 0$. The time average value for the degree of spin polarization $\bar{\rho}_z(\Omega_{\mathrm{ext}})$ is then expected to have the same dependence on the external magnetic field.

Equation (3.19) differs from the standard Hanle effect expression derived in Ref. [99] due to the anisotropic spin relaxation in (110) QWs. The spin polarization dynamics, described by equation (3.13), depends on the out (τ_z) and in-plane (τ_x) spin relaxation times, which are different. Equations (3.13) and (3.19) are, however, expected to provide the same description of the spin relaxation dynamics. As will be demonstrated in Chapter 6, this expectation is experimentally fulfilled with very similar in and out of plane spin relaxation rates obtained from time-resolved and CW optical pumping experiments.

3.4.2 Spin dephasing during transport along the $[1\bar{1}0]$ direction

In the case of the Bleustein-Gulyaev wave propagating along $[1\bar{1}0]$, the non-zero average carrier momentum impinged by the SAW is $\langle k_y \rangle$. Equation (3.9) implies that the internal magnetic field interacting with the electron spins will have a non-zero average value $\langle \mathbf{B}_{\mathrm{int}} \rangle$ for transport along this direction. When an in-plane external magnetic field is applied, the average spin vector of the ensemble will precess around a resultant magnetic field given by $\mathbf{B}_{\mathrm{R}} = \mathbf{B}_{\mathrm{ext}} + \langle \mathbf{B}_{\mathrm{int}} \rangle$. Since $\langle \mathbf{B}_{\mathrm{int}} \rangle$ points along $\hat{z}$, the spin dynamics is then described by a three-dimensional problem, with spin polarization components s_x, s_y, and s_z evolving in time according to:

$$\frac{\partial}{\partial t} \begin{pmatrix} \mathrm{s}_x \\ \mathrm{s}_y \\ \mathrm{s}_z \end{pmatrix} = - \begin{pmatrix} \gamma_x & \Omega_z & -\Omega_y \\ -\Omega_z & \gamma_y & \Omega_x \\ \Omega_y & -\Omega_x & \gamma_z \end{pmatrix} \begin{pmatrix} \mathrm{s}_x \\ \mathrm{s}_y \\ \mathrm{s}_z \end{pmatrix} - \gamma_{\mathrm{r}} \begin{pmatrix} \mathrm{s}_x \\ \mathrm{s}_y \\ \mathrm{s}_z \end{pmatrix}. \tag{3.20}$$

Here $\Omega_{\mathrm{R}} = (\Omega_x, \Omega_y, \Omega_z)$ is the Larmor precession frequency of the average spin vector around the resultant magnetic field $\mathbf{B}_{\mathrm{R}}$. Equation (3.20) can be solved numerically. We have used this procedure to fit the experimental data to be presented in chapter 6. The initial condition to find the solution for the degree of spin polarization is $\rho(t=0) = (0, 0, \rho_0)$. Since $\mathbf{B}_{\text{ext}} \parallel [1\bar{1}0]$, the resultant Larmor frequency is $\Omega_{\text{R}} = (0, \Omega_{\text{ext}}, \langle\Omega_{\text{int}}\rangle)$. We also assume $\gamma_x = \gamma_y$.

Note that the solution of equation (3.20) is analog to the one of equation (3.12) for spin transport along the [001] direction, except for the fact that the average spin polarization precesses around the resultant magnetic field $\mathbf{B}_{\text{R}}$, which has an out-of-plane component. In this way, the longitudinal component of the spin polarization (i.e., the one parallel to the axis defined by $\mathbf{B}_{\text{R}}$) thermalizes with a time τ_l, which is expected to be close to τ_z. The time evolution of the z-component of the longitudinal degree of spin polarization ρ_z^ℓ can be written in the form:

$$\rho_z^\ell(\Omega_{\text{ext}}, t) = \rho_0 \cos(\theta) e^{-t/\tau_l} = \rho_0 \left(\frac{\langle B_{\text{int}}\rangle}{\sqrt{\langle B_{\text{int}}\rangle^2 + B_{\text{ext}}^2}} \right) e^{-t/\tau_l}, \qquad (3.21)$$

where θ defines the angle between the z-axis and the direction of the resultant magnetic field $\mathbf{B}_{\text{R}}$, as illustrated in Fig. 3.4.

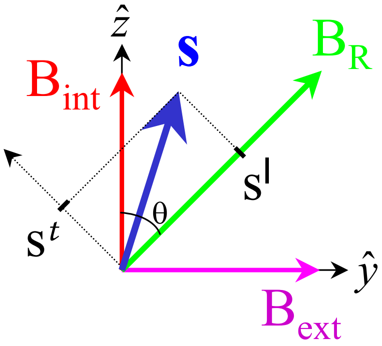

Figure 3.4: Vector scheme illustrating the longitudinal (s^ℓ) and the transverse (s^t) spin polarization components (with respect to $\mathbf{B}_{\text{R}}$) for spin transport along the $[1\bar{1}0]$ direction.

The transverse component of the spin polarization (perpendicular to the direction of $\mathbf{B}_{\text{R}}$) will be sensitive to fluctuations in $\mathbf{B}_{\text{R}}$ caused by momentum scattering. Therefore, it is expected to last for a time comparable to τ_{s} [equation (3.14)] and have a time dependence described by a damped spin precession around $\mathbf{B}_{\text{R}}$ equivalent to equation (3.13).

3.5 SAW induced spin relaxation

We have considered in section 3.3 the DP and the BAP relaxation mechanisms. At low temperatures, these processes become the most effective ones for symmetric, unstrained, and undoped (110) 2D GaAs systems. In particular, equation (3.9) tells us that the DP process is suppressed for z-oriented spins in (110) QWs so that the BAP mechanism remains the only relevant intrinsic spin relaxation process for optically generated carriers.

In this section, we discuss spin relaxation processes induced by the fields carried by a SAW propagating on the 2D structure. As we discussed in section 2.3, the SAW possesses a strain and a piezoelectric field. The carriers are captured by the piezoelectric field and transported in a well-defined position within the SAW cycle. Therefore, the moving carriers are, in general, subjected to non-zero strain and electric fields during transport. These fields lead to additional contributions to the spin splitting of the conduction band.

3.5.1 Bychkov-Rashba mechanism

The SIA contribution to the SO-Hamiltonian in equation (3.2) is normally denoted as the Bychkov-Rashba term [25, 26, 110]. This contribution appears in QWs with an asymmetric confinement potential. The asymmetry may be intrinsic or induced by the application of external fields. For a 2D system, the Bychkov-Rashba term is given by [144]:

$$H_{\mathrm{br}}(\mathbf{k}) = r\ \sigma \cdot \mathbf{k} \times \mathbf{E}. \tag{3.22}$$

Here, r is a material specific parameter and $\mathbf{E}$ the electric field characterizing the asymmetric confinement potential. Note that, in a 2D system, only an electric field component along the confinement direction leads to a Bychkov-Rashba contribution. In this way, the effective magnetic field (B_{br}) associated with this contribution always lies in the QW plane and is perpendicular to the carrier momentum. Figure 3.5 illustrates this situation for the effective magnetic field felt by a spin up electron propagating in the QW plane. B_{br} can be used for spin manipulation. Spin control using external electric fields perpendicular to the QW growth direction was the main motivation for the proposal of the spin transistor by Datta and Das in the early 90's [40].

Strictly speaking, (110) QWs grown with nominally symmetric barriers, as in our case, should not exhibit spin relaxation due to the Bychkov-Rashba effect. However, even in nominally symmetric structures a small contribution from Rashba coupling to spin relaxation may appear due to small differences between the interfaces on both sides of the quantum well [22, 41, 140]. Fluctuations of the doping density, for the case of doped materials, have also been shown to add a SIA splitting [122].

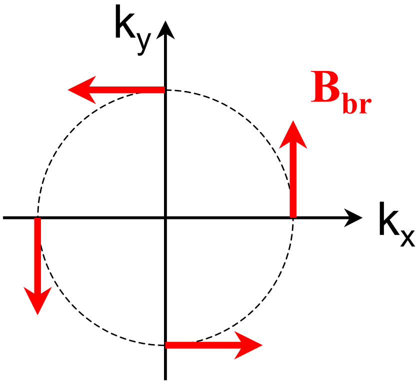

Figure 3.5: Effective magnetic field in the QW plane introduced by the SIA contribution to the SO-coupling. The internal Bychkov-Rashba field $\mathbf{B}_{\mathrm{br}}$ lies in the QW plane and points always perpendicularly to the carrier momentum direction.

As pointed out in subsection 2.3.2, the SAW carries a moving piezoelectric field with a z-component E_z of a few kV/cm which can also induce a small contribution of the SIA type. The spin-splitting due to an electric field E_z applied along the z-direction obtained from equation (3.22) is given by [144]:

$$\hbar\Omega_{\mathrm{br}} = r\mathrm{E}_z\ k_{\|}, \tag{3.23}$$

where Ω_{br} is the Larmor precession frequency associated with B_{br}, $r = 5.2\ e\mathring{A}^2$ for GaAs (cf. Appendix A), and $k_{\|}$ is the in-plane electron momentum.

In the (110) reference frame, the Rayleigh SAW propagating along the $\hat{x} \parallel [001]$ direction imparts an average momentum $\langle k_x \rangle = m_0 v_x/\hbar$ to the electrons, where v_x is the SAW propagation velocity. The Bychkov-Rashba precession frequency can, therefore, be written in the form:

$$\Omega^{\mathrm{R}}_{\mathrm{br}}(\mathbf{k}) = -\frac{r\ \mathrm{E}_z}{\hbar}\begin{pmatrix} 0 \\ \langle k_x \rangle \\ 0 \end{pmatrix}. \tag{3.24}$$

During their transport along $\hat{x}$, the electrons then experience an effective average SIA-field pointing along the $\hat{y}$ direction.

For a SAW propagating along the $\hat{y} \parallel [1\bar{1}0]$ direction with average momentum $\langle k_y \rangle = m_0 v_y/\hbar$, the field is directed along $\hat{x}$, and the precession frequency is given by:

$$\Omega^{\mathrm{BG}}_{\mathrm{br}}(\mathbf{k}) = \frac{r\ \mathrm{E}_z}{\hbar}\begin{pmatrix} \langle k_y \rangle \\ 0 \\ 0 \end{pmatrix}. \tag{3.25}$$

As discussed in chapter 2, the propagation velocity of the acoustic modes along [001] and $[1\bar{1}0]$ is similar. Therefore, differences between the average Bychkov-Rashba fields acting on the propagating along the two directions spins are basically determined by the amplitude of E_z.

3.5.2 The influence of strain on spin relaxation

Deformations of the lattice change the band structure of a semiconductor and can influence its electrical and optical properties [32, 99]. The strain also induces a SIA contribution to the SO-coupling. The corresponding strain-induced spin-splitting has been used to induce coherent spin precession in semiconductors [84]. In the same manner as static deformations, the propagating SAW strain field induces a conduction band spin-splitting which affects the spin dynamics.

As for an electric field, the deformation of crystals with zinc-blende structure may induce a SIA contribution to the spin splitting which is linear in momentum **k** and proportional to the strain amplitude S [99, 109]. Two terms describe the conduction band Hamiltonian of such a strained crystal [51]:

$$
\begin{aligned}
H_{strain} &= \frac{\hbar}{2}\left[\sigma \cdot \Omega_{\mathrm{s}}^{'}(\mathbf{k}') + \sigma \cdot \Omega_{\mathrm{s}}^{'*}(\mathbf{k}')\right], \qquad (3.26)\\
\text{where} \quad \hbar\Omega_{\mathrm{s},x'}^{'} &= C_3\left(\mathrm{S}_{x'y'}k_y' - \mathrm{S}_{x'z'}k_z'\right),\\
\text{and} \quad \hbar\Omega_{\mathrm{s},x'}^{'*} &= C_3^{*}k_x'\left(\mathrm{S}_{y'y'} - \mathrm{S}_{z'z'}\right).
\end{aligned}
$$

The x', y', and z' axes in equation (3.26) denote the main axis of the system, shown in Fig. 2.1(b). The strain components S_{ij} are defined by equation (2.3). The y' and z' components of the strain-induced precession frequencies are obtained by cyclic permutation of the spatial indices in $\Omega_{\mathrm{s},x'}$ and $\Omega^{*}_{\mathrm{s},x'}$. For GaAs, the constant C_3 has been determined both experimental and theoretically [17, 27, 51, 99, 125]. The experimentally obtained values range from 0.8 eV$\mathring{A}$ [125] to 8.1 eV$\mathring{A}$ [17]. As we discuss in chapter 5, the comparison between the experimentally determined and the expected spin relaxation rates associated with the the strain field in our system suggest a very low value for C_3. Therefore, in our calculations we adopt the positive value for $C_3 = 0.8$ eV$\mathring{A}$ from Ref. [125] (cf. Appendix A), obtained for spin-strain coupling coefficient for GaAs epilayers. C_3^{*} appears due to interaction with remote bands and should be negligible as compared to C_3 [51, 99]. Therefore, in the following we will set $\Omega^{*}_{\mathrm{s},i} = 0$.

To obtain the corresponding precession frequencies due to the strain field of a SAW propagating on the (110) surface, it is convenient to rotate the reference frame following the procedure described in subsection 2.2.1. $\Omega_{\mathrm{s}}(\mathbf{k})$ will then depend on the strain components written on equations (2.11) and (2.12) for the SAW propagating along the [001] and [1$\bar{1}$0] directions, respectively. For the Rayleigh wave propagating along the $\hat{x} \parallel [001]$ direction the only strain component relevant for the spin-splitting is the shear component S_{xz}, which removes the mirror symmetry of the plane perpendicular to the growth direction $\hat{z}$. After the reference frame rotation, we obtain the precession frequency associated with the strain for the Rayleigh wave. It has a single non-zero component $\Omega^{\mathrm{R}}_{\mathrm{s},y}$ along $\hat{y}$, given by:

$$\Omega^{\mathrm{R}}_{\mathrm{s}}(\mathbf{k}) = -\frac{C_3}{\hbar}\begin{pmatrix} 0 \\ \mathrm{S}_{xz}\langle k_x\rangle \\ 0 \end{pmatrix} \qquad (3.27)$$

Analogously, the shear strain component S_{yz} of the Bleustein-Gulyaev wave propagating along the $\hat{y} \parallel [1\bar{1}0]$ direction leads to an electron precession frequency $\Omega_{\mathrm{s}}^{\mathrm{BG}}(\mathbf{k})$ given by:

$$\Omega_{\mathrm{s}}^{\mathrm{BG}}(\mathbf{k}) = -\frac{C_3}{\hbar}\begin{pmatrix} \mathrm{S}_{yz}\langle k_y\rangle \\ 0 \\ 0 \end{pmatrix} \tag{3.28}$$

Equations (3.27) and (3.28) indicate that, as in the case of the Bychkov-Rashba contribution induced by the piezoelectric field, the effective magnetic field due to the strain lies in the QW plane and is always directed perpendicularly to the SAW propagation direction.

3.6 Discussion

In this brief section, we make an overview of spin relaxation studies in (110) QWs and their relation with what has been discussed in this chapter.

As discussed in section 3.4, the dynamics of optically-oriented electron spins is described by the spin relaxation time τ_z. When external fields are applied to induce spin precession, the spin lifetime τ_{s} [given by equation (3.14)] determines the time scale for spin decoherence. These two times arise from the simultaneous action of different dephasing mechanisms on the spin vector of the ensemble. In general, each mechanism has a particular dependence on parameters like temperature or external fields and the relevant ones can be identified by analyzing the dependence of the spin lifetimes on such parameters.

In the absence of external magnetic fields, the suppression of the DP relaxation mechanism for spins along the z-direction due to the special symmetry of (110) III-V QWs is expected to lead to long spin lifetimes. Spin lifetimes in (110) oriented superlattices have been shown to have a spin relaxation rates one order of magnitude slower than their (001) counterparts [66]. The absence of the DP mechanism has been attributed as the main reason for the long spin relaxation times ranging from approximately 1 to 10 ns obtained in (110) GaAs [1, 45, 82, 105], InAs [68], and InGaAs [101] QWs.

The magnitude of the spin lifetimes for the (110) systems depends, therefore, on the ability to control other relevant spin relaxation processes. Temperature is probably the most important parameter in order to identify these mechanisms. The interaction between the electron and hole spins (the BAP mechanism) was demonstrated to be effective at low temperatures (below 100 K) [45, 105]. Different approaches have been used to control this interaction. The BAP mechanism has been reduced by *n*-doping, with longer spin lifetimes been verified in comparison to undoped (110) QWs. The longer lifetimes were attributed to a screening of the *e*-*h* interaction due to the excess electrons [1, 101]. Another approach relies on the reduction of the *e*-*h* interaction due to type-II confinement of carriers in InAs QWs with AlSb barriers [68]. In acoustic transport, the efficiency of the BAP mechanism is expected to be diminished by the type-II spatial separation of electrons and holes induced by the moving SAW piezoelectric potential [129].

For temperatures above 100 K, where the *e*-*h* interaction is weaker, the spin lifetimes in (110) QWs have been shown to be mainly limited by asymmetries between the two QW interfaces, which lead to built-in SIA fields [68, 82, 92]. The SIA contribution has also been shown to reduce the spin lifetimes in strained (110) QWs [121]. In section 3.5, we have shown that during acoustic transport SIA can also be induced by the SAW fields. This contribution to spin relaxation can be written as in-plane effective magnetic fields perpendicular to the carrier propagation direction. Figure 3.6(a) resumes schematically the effective fields acting on a spin polarized carrier packet propagating along the $\hat{x} \parallel [001]$ direction. According to equations (3.24) and (3.27), the SAW effective magnetic fields $\mathbf{B}^{\mathrm{R}}_{\mathrm{br}}$ and $\mathbf{B}^{\mathrm{R}}_{\mathrm{s}}$ due to the piezoelectric and strain fields, respectively, have the same orientation along the y axis. For propagation along the $[1\bar{1}0]$ direction, the acoustic fields associated with the Bleustein-Gulyaev wave, $\mathbf{B}^{\mathrm{BG}}_{\mathrm{br}}$ and $\mathbf{B}^{\mathrm{BG}}_{\mathrm{s}}$, have opposite

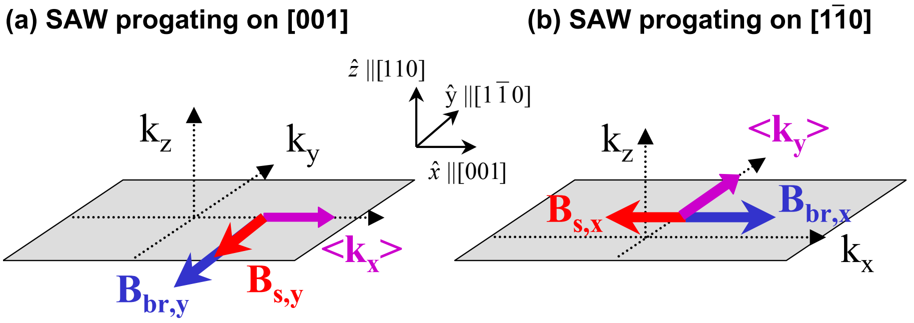
(a) SAW progating on [001]

(b) SAW progating on $[1\bar{1}0]$

Figure 3.6: Effective magnetic field induced by the SAW fields during acoustic transport in (110) QWs along the (a) [001] and (b) $[1\bar{1}0]$ directions.

orientation according to equations (3.25) and (3.28). This is illustrated in Fig. 3.6(b).

For wider QWs ($d > 20$ nm), where occupation of higher subbands at elevated temperatures can be considerable, a new spin relaxation mechanism has been proposed. Using first order perturbation theory the authors in Ref. [45] demonstrate that there is a non-zero probability of spin-flip when an electron in the conduction band is thermally excited from the first to the second subband, leading to the so-called intersubband spin relaxation (ISR). The spin relaxation time for the ISR process is proportional to the momentum scattering time, thus decreasing with temperature. The theory was successfully applied to explain the decrease of the spin relaxation times observed from 120 to 300 K in a apparently SIA free (110) system. In the high temperature regime, ISR could be relevant for the spin relaxation in the 18 nm-thick (110) QWs employed in our experiments. However, as we will verify in chapter 5, acoustic spin transport above 80 K could not be accomplished due to the low transport efficiency. We, therefore, have no evidences of the influence of the ISR relaxation mechanism in our experiments.

The discussion in the previous paragraphs justifies why the Elliott-Yafet relaxation mechanism [53, 135] has not been considered as one of the main sources of spin relaxation in our system. Pure (110) GaAs QWs, i.e. with very low concentration of impurities and defects, were shown to have no significant contribution to the relaxation of optically excited spins due to this mechanism [45, 82, 105]. Reports based on temperature-dependent measurements of the spin relaxation times in intrinsic (110) QWs have shown that BAP and built-in SIA contributions are the main relaxation processes up to 100 K. As we will show in chapter 5, our measurements also reveal no significant contribution from the EY mechanism to the spin relaxation dynamics.

Another spin relaxation process, which we did not take into account here is the spin relaxation via the hyperfine interaction [50, 99, 106]. This process requires that the nuclei have a non-zero average spin polarization in order to interact with the electron spins. Under external magnetic fields, dynamic nuclear polarization can be enhanced by the interaction with light [117]. However, for normal light incidence and weak in-plane external magnetic fields this mechanism leads, in general, to negligible contributions.

When in-plane external magnetic fields are applied, the spin relaxation efficiency in (110) QWs increases dramatically. Döhrmann *et al.* [45] demonstrated that the application of an in-plane external magnetic field leads to spin lifetimes τ_s much shorter than τ_z. Fluctuations of the internal BIA magnetic field due to in-plane momentum scattering [equation (3.9)] were shown to dephase the spin components very quickly. In this way, an anisotropy between out (τ_z) and in-plane (τ_x) spin relaxation times was demonstrated and attributed to the effects of the BIA relaxation, once suppressed in the zero-field situation. In fact, further studies of the anisotropic spin relaxation in (110) QWs demonstrated the ability to tune the relaxation anisotropy. Taking the dependence of τ_x on the momentum scattering time, confinement energy, and temperature expected from equation (3.17), a variety of τ_z/τ_x ratios have been reported [101, 121].

In addition to the suppression of the BAP relaxation, another advantage of employing SAWs to transport spins comes from the ability to impinge a well-defined average momentum to the carrier ensemble. In contrast to all the previous experiments, where the average carrier momentum vanishes, different in-plane propagation directions can be chosen for acoustic transport in order to explore the SO-coupling dependence on carrier momentum direction. The carrier momentum dependence of the internal magnetic field in equation (3.9) leads, consequently, to different spin dynamics along different in-plane propagation directions. This topic will be addressed in chapter 6, where we demonstrate that in (110) QWs the spin dephasing dynamics depends on the transport direction and can be understood in terms of the **k**-dependence of the D'yakonov-Perel' mechanism.

Chapter 4

Experimental details

In this chapter, we provide details about sample growth and processing, as well as about the spectroscopic techniques to probe carrier and spin transport using SAWs. We start with the growth of (110) GaAs structures using molecular beam epitaxy (MBE). We then describe the (Al,Ga)As layer structures used for acoustic transport. The processing steps after the MBE growth are also described. They include the deposition by sputtering of a piezoelectric ZnO layer (in one of the samples) followed by the photolithographic fabrication of metallic interdigital transducers (IDTs) for the generation of acoustic beams. In the last part of the chapter, we comment on the optical experiments, which have enabled us to study the time and spatial evolution of spin-polarized carriers during acoustic transport.

4.1 Sample preparation

All the steps of the sample preparation (MBE growth, ZnO sputtering, and IDT processing) were performed at the facilities of the Paul-Drude-Institute.

4.1.1 MBE growth of (110)-oriented structures

We start with a short review of MBE growth of (110)-oriented films on (110) substrates. The growth of such structures is a non-trivial procedure and has not received much attention as the one for (001) layers.

MBE is a thin film deposition technique carried out under ultrahigh vacuum (UHV) conditions, at a base pressure typically around 10^{-11} Torr. The constituents of the film are provided by separate evaporation of source materials from thermally heated crucibles. In case of III-V compounds, the molecular beams consist of atoms (group III elements) and molecules (dimers, tetramers, and group V element). Under standard conditions, the sticking coefficient of group III element is unity, whereas the sticking coefficient of group V element is always lower then unity. Before being incorporated, the group V element, which is provided in excess, undergoes a thermal cracking process at the surface of the heated surface. Since during the thin film formation the excess group V element evaporates, an almost perfect stoichiometric compound is formed.

As the molecular beams are controlled by individual shutters in front of the sources, this technique allows for the fabrication of layer systems tailored on a submonolayer scale. Usually, growth rates, surface, and film quality are precisely controlled during growth by *in situ* monitoring techniques. The most common one is the Reflection High-Energy Electron Diffraction (RHEED), which enables the analysis of the growing layers through the diffraction pattern of electrons diffracted at grazing incidence.

MBE growth studies of (110) GaAs layers date back to the 70's and were originally motivated by the manufacturing of GaAs devices on group-IV semiconductors [71]. The (110) non-polar plane of the zinc-blende structure had been proposed as one of the preferred orientations for the epitaxial growth of zinc-blende films on group IV substrates, because of the absence of interface charge imbalance for this plane [91]. This special interface property has motivated several studies of epitaxial growth of III-V materials on group IV (110) substrates, including GaAs on Ge [28], GaP on Si [146], and GaAs on Si [93]. The optical anisotropy of the (110) QWs [63] was another motivation for device applications, like optical modulators or vertical-cavity surface emitting lasers (VCSEL) [134].

The initial growth studies of GaAs and (Al,Ga)As on (110) GaAs substrates reported great difficulties in obtaining high-quality epilayers at growth temperatures above 620°C. Growth instabilities and morphological imperfections have been some of the reported problems. [13, 139] During the homoepitaxial MBE growth of GaAs (110) under these conditions, the surface appeared completely covered with facets, thus degrading the optical and electrical characteristics of the epilayers. Detailed investigations of facet formation and geometry was reported by Allen *et al.* [2, 3]. These authors showed that the facets are aligned along the [001] direction with sides composed of (010), (100), and (111) Ga back faces. In order to obtain smooth surfaces using MBE, they proposed the use of (110) substrates tilted by a relatively large angle (of approx. 6°) towards the $(11\bar{1})$Ga direction. Since As has a lower sticking coefficient than Ga, tilting the sample exposes the $(11\bar{1})$ Ga-rich planes, thus reducing the As desorption and forming stable surface basis for further incoming molecular beams of Ga and As [2, 3]. This procedure also improved the quality of heterostructures [133]. Migration-enhanced epitaxy (MEE) [94] leads to further structural improvements and to smoother surfaces and interfaces [75, 103]. Here, the Ga and As_4 fluxes are supplied discontinuously to the substrate by opening alternately the shutters in front of the evaporation sources.

Significant improvements on the structural quality of the (110) structures have been obtained by using lower growth temperatures and higher V-III flux ratios [55, 63, 138]. Finally, the morphology of the interfaces could be further improved by adding growth interruptions for surface annealing [148]. The combination of these techniques has lead to (110) QWs with high structural quality, which has been demonstrated to enhance the spin lifetimes in these systems [92].

4.1.2 (110) GaAs quantum wells for acoustic transport

Spin transport by surface acoustic waves requires a high degree of structural perfection, specially at the QW interfaces. Potential fluctuations at these interfaces hinders the transport of carriers by the moving piezoelectric field. Interface states can trap propagating carriers and induce recombination, thereby deteriorating the ambipolar transport efficiency [5]. Available interface states produced by thickness variations and/or defects can, in some cases, be reduced by employing doping [30]. This procedure, however, leads to degradation of the piezoelectric properties of the material. Furthermore, to transport carriers coherently (i.e., with the acoustic velocity v_{saw}), a minimum value of carrier mobility (μ_c) is required in order to satisfy the condition $v_{saw} = \mu_c F_{saw}$, where F_{saw} is the longitudinal component of the SAW piezoelectric field. As will be demonstrated in Chapter 5, low transport efficiency also limits the spin transport lengths. The mobility requirement can be compensated if the piezoelectric SAW field F_{saw} is increased. This can be achieved by depositing a piezoelectric layer of ZnO on top of the III-V structure, as will be discussed in subsection 4.1.3.

Material	**Thickness (nm)**
ZnO	500
GaAs	10
$Al_{0.1}Ga_{0.9}As$	370
$Al_{0.3}Ga_{0.7}As$	10
GaAs	**18 (QW)**
GaAs	0.2 (MEE)
$Al_{0.3}Ga_{0.7}As$	30
$GaAs/Al_{0.3}Ga_{0.7}As$	2.8/2.8 (20x)
GaAs	300
GaAs	10 (MEE)
GaAs (110) substrate	

Table 4.1: Layer structure of sample A consisting of a 18 nm-thick GaAs QW with $Al_{0.3}Ga_{0.7}As$ barriers.

In order to reach the electronic quality required for acoustic transport, an optimization of the MBE deposition conditions for $GaAs/Al_xGa_{1-x}As$ structures was carried out. The multilayer structure of sample A is shown in Table 4.1. After the conventional oxide desorption, the GaAs (110) surfaces were smoothed by the deposition of a 10 nm-thick GaAs layer grown in the MEE mode. The 18 nm-thick GaAs QW and the $Al_{0.3}Ga_{0.7}As$ barriers were deposited at $T_G = 490°C$ under a V-III beam equivalent pressure[1] ratio of 70 and a growth rate of approximately 220 nm/h. As shown in Table 4.1, a 20 period $GaAs/Al_{0.3}Ga_{0.7}As$ superlattice was introduced before the QW growth. This superlattice smoothes the growth front and considerably improves the structural quality of the material and of the QW interfaces. Furthermore, the increase in the number of interfaces with the addition of the superlattice efficiently blocks impurity riding from the substrate to the QW, thus increasing the purity of the 2D structure. At the end of every growth step, the process was interrupted for a 1 min annealing at 600°C to reduce the surface step density. As indicated in Table 4.1, the sample was produced performing two stages of MEE growth. The second one (0.2 nm), however, did not lead to substantial improvement of the optical properties [73]. Note that Table 4.1 includes the ZnO sputtered layer. Its deposition will be described in the next subsection.

The structural quality of the sample was evaluated by analyzing the full-

---

[1] Beam equivalent pressure (BEP) is the relative pressure between the V and III material beams.

width at half-maximum (FWHM) of the photoluminescence (PL) measured at low temperature (5 K). Rough interfaces broaden the PL line due to variations of the band gap energy over regions with inhomogeneous QW widths. Therefore, the narrower the FWHM of the PL, the higher the degree of homogeneity is expected for the QW interfaces. Figure 4.1 shows the PL spectrum recorded at T = 5 K for sample A, which has a PL FWHM of 0.8 meV. Although this value exceeds the one for (001) GaAs QWs with the same thickness by a factor of approximately 5 [72], the sample quality was found to be suitable for acoustic transport experiments. In general, FWHMs smaller than 1 meV are required for efficient acoustic transport.

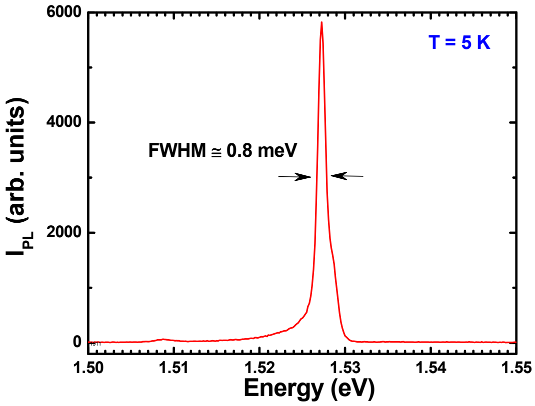

Figure 4.1: PL emission of the 18 nm-thick GaAs QW structure of Table 4.1. The small FWHM of 0.8 meV reflects the high degree of structural perfection.

We have also performed transport experiments on a second sample (sample B) containing a shallower (160 nm below the surface) 18 nm-thick QW, as shown in Table 4.2. Sample B did not receive a ZnO layer on top. This sample, however, was grown at an early stage of the growth optimization process and has a lower degree of structural perfection as compared to sample A. In fact, the PL emission for this sample was not homogeneous, changing slightly for different sample areas. The FWHM was approximately 2 meV. The transport measurements on this sample were important mainly to analyze the effects introduced by the piezoelectric film on carrier and spin transport properties of sample A. As we will show in chapter 5, the presence of the piezoelectric ZnO film significantly improves the carrier transport properties, increasing the spin transport length by a factor of approximately 5. Therefore, throughout this work most of the attention is devoted to sample

A.

Material	Thickness (nm)
GaAs	10
$Al_{0.3}Ga_{0.7}As$	150
GaAs	18
GaAs	0.2 (MEE)
$Al_{0.3}Ga_{0.7}As$	20
GaAs	10 (MEE)
GaAs	400
GaAs	100 (MEE)
GaAs (110) substrate	

Table 4.2: Layer structure of sample B consisting of a 18 nm-thick GaAs QW with $Al_{0.3}Ga_{0.7}As$ barriers.

4.1.3 ZnO sputtering

The initial acoustic transport experiments on (110) QWs have shown that the SAW-induced piezoelectric fields were not sufficiently strong to capture and coherently transport the carriers along the SAW propagation path [147]. Strong piezoelectric fields were obtained by coating the (Al,Ga)As structures with a piezoelectric ZnO film. Polycrystalline ZnO thin films deposited by sputtering are widely used in different applications like SAW transduction, optical waveguides [69], and acousto-optic devices [31, 52]. In order to be piezoelectric, the *c*-axis (the polar axis of the material) of the hexagonal (wurtzite) ZnO crystallites has to be preferentially oriented along the growth direction [62, 107]. The films have also to have a high electrical resistivity to avoid electrical losses during the SAW excitation using the IDTs.

We have coated sample A with a 500 nm-thick ZnO layer using a conventional rf-magnetron sputtering machine with a ZnO target. The ZnO deposition was carried out at 200°C in an Ar/O_2 atmosphere. The addition of O_2 is important to increase the electrical resistivity. Prior to ZnO deposition, the sample surface was cleaned by an ion-etching process. We found that the electronic properties of QWs placed at depths shallower than 150 nm below the surface were severely degraded during the ion-etching. For this reason, the 18 nm-thick QW of sample A was intensionally grown at a depth of 390 nm.

The high degree of *c*-orientation of the ZnO grains in the film is demonstrated by the X-ray $\omega - 2\theta$ diffraction curve of Fig. 4.2, which was obtained using the Cu Kα_1 wavelength of 0.154060 nm. The pronounced diffraction peak from the (0002) plane of ZnO at $\omega = 17.23°$ indicates the preferential orientation of the ZnO crystallites. The diffraction peak from (220) GaAs planes is situated at $\omega = 22.66°$. Diffraction peaks from the ZnO (0004) and GaAs (440) planes are also observed at $\omega = 36.31°$ and $50.42°$, respectively. The inset shows the rocking curve recorded around the (0002) ZnO plane. The FWHM $= 4.35°$ of the rocking curve reflects the angular distribution of the c-axis of the crystallites around the normal to the sample plane [62]. We did not perform a systematic study, but the weak X-ray peak situated at $\omega = 18.09°$ can be related to crystallites with slightly tilted c-axis. This would slightly reduce the piezoelectric field expected for such a structure.

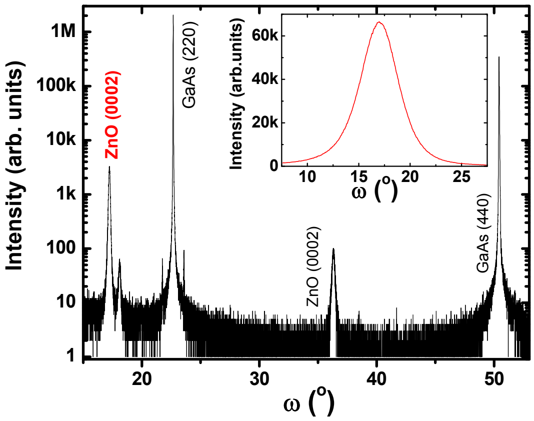

Figure 4.2: X-ray diffraction curve of sample A after the ZnO sputtering (cf. Table 4.1). The ZnO (0002) diffraction peak from the ZnO crystallites with c-axis orientation perpendicular to the film surface is detected at $\omega = 17.23°$. The inset shows a rocking curve taken around this peak.

4.2 SAW generation

The surface acoustic waves for acoustically induced transport are electrically generated via the inverse piezoelectric effect. This is carried out using metal interdigital transducers (IDTs) deposited on the sample surface, as illustrated in Fig. 4.3(a). An IDT consists of a metal-finger grating with a repetition period equal to the SAW wavelength (λ_{SAW}). The application of a radio-frequency (rf) voltage with frequency $f_{\mathrm{SAW}} = v_{\mathrm{SAW}}/\lambda_{\mathrm{SAW}}$ (where v_{SAW} is the SAW propagation velocity) to the grating excites a coherent acoustic vibration. The length of the metal fingers determines the width of the SAW beam.

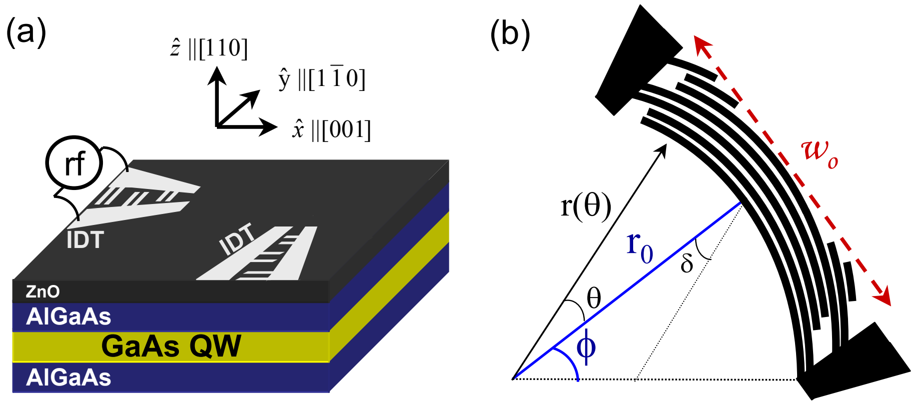

Figure 4.3: (a) Configuration of the IDTs on top of a (110) GaAs QW sample with (Al,Ga)As barriers. The sample is coated with a piezoelectric ZnO film. IDTs were designed to launch SAW beams along the [001] and [$1\bar{1}0$] surface directions. (b) Finger shape of a focusing IDT, defining the angular aperture ϕ and focusing distance r_0 of the acoustic beam.

The generation of high-power acoustic beams on GaAs requires, in general, IDTs with a large number of fingers, which have to be carefully designed to minimize losses. As the generated beam propagates through the long metal grating of the IDT, it can be reflected and scattered into bulk modes. In the simplest type of IDT, the so-called single-finger IDTs, each period consists of two fingers with width and separation equal to $\lambda_{\mathrm{SAW}}/4$. Acoustic reflections are large in this kind of structure since the grating periodicity fulfills the conditions for acoustic Bragg reflection of the excited SAW. These Bragg reflections turn single-finger IDTs into standing-wave acoustic cavities, leading to high acoustic amplitudes inside the transducers. The reflections can be minimized using a split-finger grating, where each single IDT finger is split into two. The period then consists of four fingers with width and separation corresponding to $\lambda_{\mathrm{SAW}}/8$. This configuration minimizes acoustic reflections by transforming the finger grating into a second-order one. This argument justifies the use of split-finger transducers in our experiments.

The acoustic power density can be further increased by employing acoustic beams with a narrow cross-section. Since the carriers are attracted towards regions of high acoustic power densities, these beams also act as narrow channels for acoustic transport. Narrow SAW beams can be produced by focusing IDTs with curve-shaped fingers [34]. In isotropic media, focusing is accomplished by shaping the IDT fingers in the form of an arc of circumference in order to produce a beam converging to the circumference center. In anisotropic materials (like GaAs), best focusing performances are obtained when the group velocity of the SAW beam generated at each section of the IDT is directed towards the focus point, i.e., when the IDT fingers follow lines of constant group velocity [141, 142].

We have used focusing IDTs designed by taking into account the crystalline anisotropy of GaAs (110) [43]. As illustrated in Fig. 4.3(b), the fingers in these IDTs have a parabolic shape calculated according to the expression:

$$r(\theta) = r_0 \left[1 + \frac{a}{1+2a}\theta^2 \right], \tag{4.1}$$

where r_0 is the IDT focusing length and θ is the angle defined in Fig. 4.3(b).

The anisotropic parameter a accounts for the dependence of the SAW group velocity on propagation direction caused by the crystal anisotropy. The latter is defined according to [43, 141]:

$$v_g(\delta) = v_0 \left[1 + \frac{1}{4a}\delta^2 \right]. \tag{4.2}$$

Here, v_g is the wave group velocity, v_0 is the propagation velocity of the wave along the IDT axis (i.e., for $\theta = 0$), and δ is a deviation angle with respect to the power flow direction specified by θ, as shown in Fig. 4.3(b). These quantities are related by $(1+2a)\delta = 2a\theta$. Equation (4.2) is valid for $\delta^2/4a \ll 1$.

The IDTs were deposited on samples A and B along the two in-plane directions of the (110) surface, the $\hat{x} \parallel [001]$ and the $\hat{y} \parallel [1\bar{1}0]$ direction according to the diagram in Fig. 4.3(a). They were fabricated using contact photolithography followed by a lift-off metallization process [143]. In the first step of this process, the sample is covered with a photoresist, which is brought into contact with a chromium mask fabricated by electron-beam lithography, which defines the IDT structure. The negative photoresist is exposed with UV light while the wafer is in contact position with the mask. On the sequence, a developer is used to remove the photoresist in the areas not exposed to the UV light. Because of the contact between the resist and mask, high resolution is possible in contact lithography, which in our case is 0.5 μm. The sample is then covered with a Ti/Al/Ti multilayer with layer thicknesses of 10 nm, 40 nm, and 10 nm, respectively. The lower Ti layer improves the adhesion of the metal film to the (Al,Ga)As surface, the upper one prevents the oxidation of the Al film. After metallization, lift-off of the metal is performed by etching of the photoresist, thus defining the IDT shape. The final result is viewed in the image shown in Fig. 4.4. The four focusing metal IDTs (indicated by Al) deposited on top of the ZnO film form a cross, which allows the generation of SAWs along the [001], $[00\bar{1}]$, $[1\bar{1}0]$, and $[\bar{1}10]$ directions. In the experiments which follow we used only the ones along the $\hat{x} \parallel [001]$ and the $\hat{y} \parallel [1\bar{1}0]$ directions.

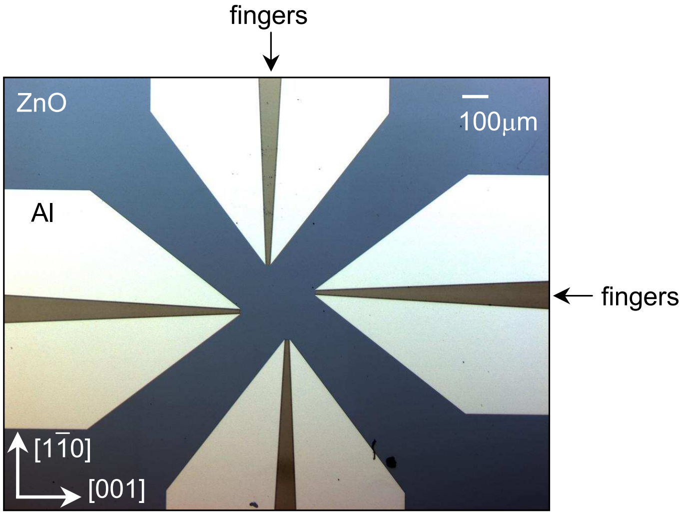

Figure 4.4: Sample surface image after the processing procedure. The dark area corresponds to the ZnO film, on top of which four metal IDTs (Al) are deposited. The focusing acoustic beams are generated by the IDTs fingers indicated by arrows.

For both [001] and $[1\bar{1}0]$ directions, the IDTs were 2 mm long, with input and output apertures of $\omega_i = 224$ μm and $\omega_o = 24$ μm, respectively. The focusing length is $r_0 = 120$ μm, corresponding to an angular aperture $\phi =$ 0.1 rad. [cf. Fig. 4.3(b)]. The value of the anisotropy parameter a depends on the propagation direction. While for the $[1\bar{1}0]$ direction $a =$ -0.0091, for the [001] $a =$ -0.154.

The same IDT design was used for samples A and B, i.e, with and without ZnO film, respectively. We will show during the discussion of the carrier and

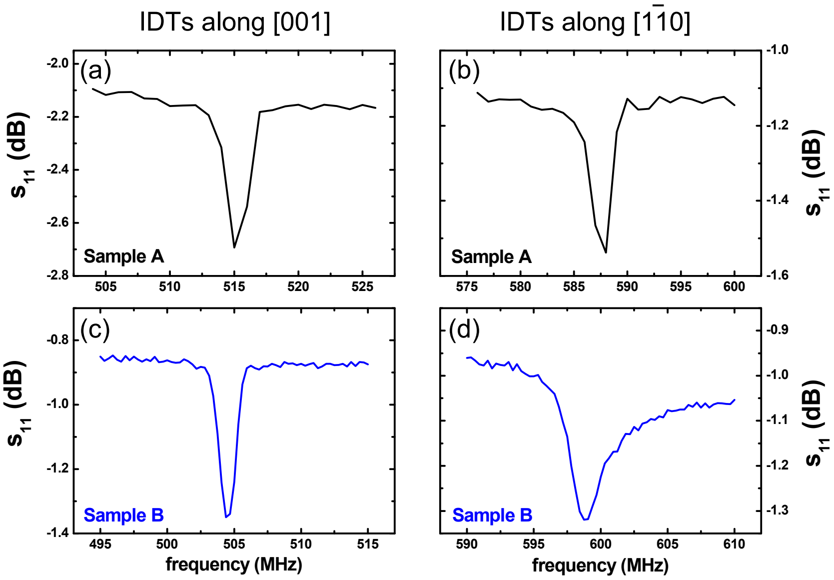

Figure 4.5: rf-reflection coefficient s_{11} measurements on IDTs along the [001] and [1$\bar{1}$0] for sample A, (a) and (b), respectively; the corresponding curves for sample B are shown in (c) and (d).

spin transport experiments in Chapter 5 that the acoustic beams were also narrow (i.e., about to 20 μm wide) for sample A, thus demonstrating that the ZnO film does not affect considerably the focusing properties.

The rf-reflection coefficient s_{11} of the double-finger IDTs deposited on sample A along the $\hat{x}$ and $\hat{y}$ directions are shown in Fig. 4.5(a) and (b), respectively. For sample B, they are shown in Fig. 4.5(c) and (d). These measurements were carried out using a network analyzer. The dips in the spectra correspond to the reduction in the reflected rf-power, which takes place when the incident electric power is converted into an acoustic mode. The SAW wavelength of the IDTs is $\lambda_{\mathrm{SAW}} = 5.6$ μm. Due to the acoustic anisotropy, the oscillation frequencies differ for the two crystalline directions. We have measured resonance frequencies of $f^{001}_{\mathrm{SAW}} = 515$ MHz and $f^{1\bar{1}0}_{\mathrm{SAW}} = 588$ MHz for the [001] and [1$\bar{1}$0] directions for sample A, respectively. The ZnO film changes slightly the resonance frequencies. For sample B, $f^{001}_{\mathrm{SAW}} = 504$ MHz and $f^{1\bar{1}0}_{\mathrm{SAW}} = 598$ MHz.

The difference $|\Delta s_{11}| = s_{11}^{(\mathrm{non-res})} - s_{11}^{(\mathrm{res})}$ between the rf-reflection coefficient at the resonance frequency ($s_{11}^{(\mathrm{res})}$) and away from it ($s_{11}^{(\mathrm{non-res})}$) is a measure of the electro-acoustic conversion efficiency of the IDTs. For sample A, the IDTs along the [001] direction $|\Delta s_{11}| = 0.54$ dB, while for the $[1\bar{1}0]$ $|\Delta s_{11}| = 0.38$ dB. Sample B, has IDTs with $|\Delta s_{11}| = 0.46$ dB and $|\Delta s_{11}| = 0.26$ dB for [001] and $[1\bar{1}0]$ directions, respectively.

The values for $|\Delta s_{11}|$ allow for the calculation of the effective acoustic power (P_{SAW}) resulting from the electro-acoustic conversion of a nominal rf-power P_{rf} applied to the IDT. Since the power conversion from dBm to mW is given by the relation P(dBm) = 10log[P(mW)], P_{SAW} is obtained from the expression:

$$P_{\mathrm{SAW}} = \frac{1}{2}\left[10^{\left(\frac{s_{11}^{\mathrm{non-res}}}{10}\right)} - 10^{\left(\frac{s_{11}^{\mathrm{res}}}{10}\right)}\right] \frac{10^{\left(\frac{P_{\mathrm{rf}}}{10}\right)}}{\omega_o} \tag{4.3}$$

The factor 1/2 takes into account the fact that the IDT launches two acoustic beams in opposite directions along the IDT axis when P_{rf} is applied. The division by the IDT output aperture ω_o allows for the comparison between the experimental and the calculated quantities [2].

Using the results presented in Fig. 4.5, we take the term in brackets in equation (4.3) to obtain the conversion efficiency for the four probed IDTs. They are 0.071, 0.064, 0.082, and 0.045 for the reflection curves in Figs. 4.5(a), (b), (c), and (d), respectively.

4.3 Optical experiments under surface acoustic wave

Figure 4.6 illustrates the experimental setup used to study spin dynamics during transport by SAWs. The SAWs are produced by exciting the IDTs with microwaves from a radio-frequency (rf) generator (Rohde&Schwarz SMT-06) tuned to the resonance frequency of the IDT. The frequency range of operation of the rf-generator goes from 5 kHz to 6 GHz, the nominal output powers up to 16 dBm. An rf-amplifier (Mini Circuits ZFL-2500 VH AS) was inserted at the generator output to increase the power applied to the IDT up to 20 dBm. The sample is mounted in a microscope cold finger cryostat (Cryovac-Konti Kryostat Mikroskop), not shown in Fig. 4.6, with rf-cables for excitation of the two IDTs. The experiments were always performed under good vacuum conditions, with pressures around 10^{-7} torr (at

---

[2] As pointed out in Chapter 2, the input power used in the numerical calculation procedure was P_l, the total acoustic power flow per unit length across the SAW beam

low temperatures). The measurement temperature could be varied from 4 to 300 K.

A commercial pulsed diode laser (PicoQuant LDH-P-780) emitting at 785 nm (approx. 50 meV above the *e-hh* transition of the QW) with pulse width of ≈ 100 ps and repetition rate of 40 MHz was used as the light source in most of the experiments to be presented in chapters 5 and 6. A Ti-Sapphire laser (at 780 nm) was used in experiments requiring a continuous wave (CW)

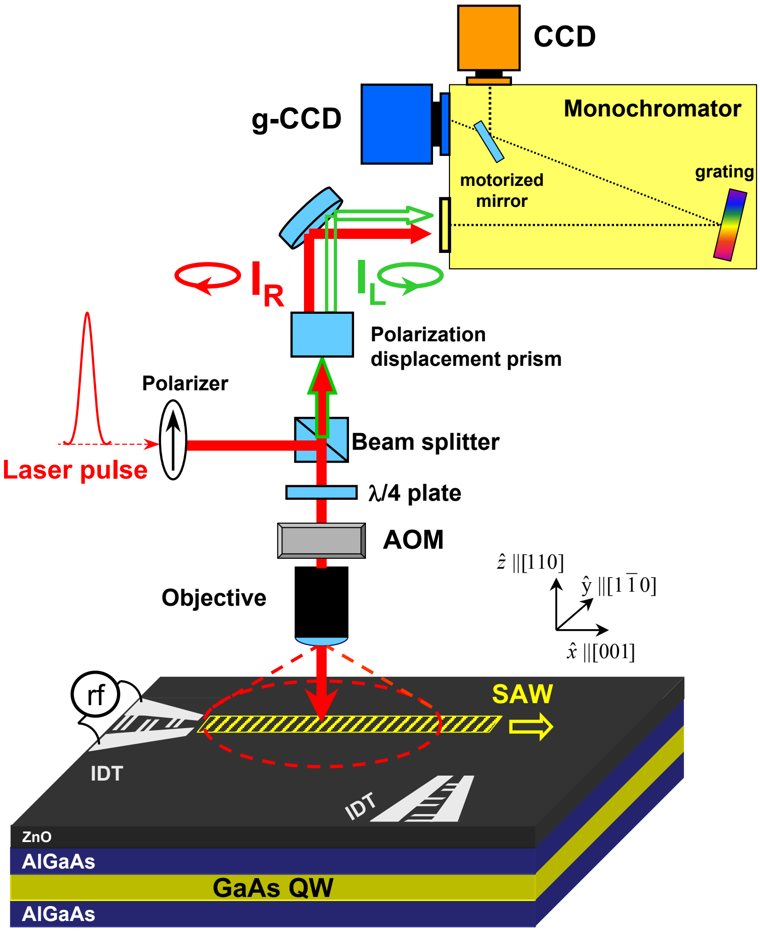

Figure 4.6: Experimental setup for the optical studies: a linearly polarized laser pulse becomes right circularly polarized after passing a $\lambda/4$ plate; an objective focuses the beam on the SAW path to generate spin polarized carriers; the emitter PL is collected by the same objective. Before entering the monochromator, the right (I_R) and left (I_L) circularly polarized PL components are separated by a polarization displacement prism and simultaneously detected in different areas of a CCD camera.

light source. In the experimental setup of Fig. 4.6, the linearly polarized laser beam is turned into a left circularly polarized one after passing a $\lambda/4$ plate. The laser beam is focused to a spot of diameter of ≈ 10 μm FWHM on the SAW path by a 20 × microscope objective (Mitutoyo G09003903A). In some of the experiments a 50 × magnification objective (Mitutoyo F59022901) was also employed. The laser spot generates carriers with spins preferentially polarized along the growth direction. The spin polarized carriers are captured by the SAW and transported along the SAW propagation direction. The PL emitted within the transport path is collected by the same objective. Its circular polarization is analyzed by the $\lambda/4$ plate and a polarization displacement prism. The latter displaces vertically the light components polarized along the x and y directions, which correspond to the PL emitted with right (I_R) and left (I_L) circular polarizations, respectively. These two beams are then detected simultaneously at different regions of a charge-coupled-device camera (CCD) coupled to a monochromator (JY T6400 with a grating with 1200 l/mm). Two types of CCD-detectors can be selected using a turning mirror. The first type is a standard charge-coupled-device camera (CCD) (JY Symphony), which detects the integrated photoluminescence with high sensitivity. The second type is a gated CCD LaVision Picostar HR12 (g-CCD in Fig. 4.6), for time-resolved experiments. This detector has an image intensifier, which can be synchronized with the laser pulses. In these experiments, the delay between the laser excitation pulse and the gated CCD is set by an electric delay line. Both spectral or spatial resolution of the PL signal were allowed by exchanging the 1200 grooves/mm diffraction grating by a mirror.

The polarization sensitivity of the optical system is calibrated using the acousto-optical-modulation (AOM) placed between $\lambda/4$-plate and the objective. When switched on, the AOM vibrates at 50 MHz and scrambles the average PL circular polarization, leading to the same time-averaged intensities for the right and left circular PL components directly after the $\lambda/4$-plate. These intensities were then used to correct for polarization distortions induced by the optical components between the $\lambda/4$-plate and the CCD detector.

The setup includes a coil outside the cryostat for the generation of magnetic fields in the plane of the sample. The coil has an iron core and produces fields with amplitudes inside the cryostat ranging from -50 to 50 mT. The axis of the coil, which defines the direction for applied field, was oriented along the $\hat{y} \parallel [1\bar{1}0]$ direction.

Chapter 5

Acoustically induced spin transport

In this chapter we present experimental results demonstrating acoustic carrier and spin transport in (110) GaAs QWs. We start with a characterization of the basic properties of acoustic carrier transport using photoluminescence (PL) experiments. We show how the SAW acoustic field quenches the PL at the carrier generation spot and subsequently transports the carriers along the propagation path. The effects of the ZnO layer on the transport efficiency are addressed. We show that the high piezoelectric field generated in the ZnO-coated sample increases the carrier capture and transport efficiencies, leading to spin transport distances approaching 70 μm. The long spin transport lengths are mainly attributed to the quenching of the D'yakonov-Perel' spin relaxation mechanism for spins oriented along the z-direction.

In order to identify the relevant spin relaxation processes, we have carried out measurements using different light excitation intensities, temperatures, and SAW powers. We demonstrate that the spin relaxation during acoustic transport does not depend on light excitation intensity and temperature (up to 80 K), thus excluding any contribution from the Bir-Aronov-Pikus relaxation mechanism. The acoustic power, however, changes the spin relaxation rates. We show that, in the low acoustic power regime, the lateral confinement imposed by the piezoelectric potential during transport further suppresses spin relaxation. Nevertheless, at high acoustic powers the in-plane average effective SIA magnetic fields induced by the SAW strain and piezoelectric fields are shown to induce spin precession.

It is important to remark that all the results for carrier as well as spin transport presented in this chapter were obtained from the analysis of transport experiments along the [001] direction of the (110) surface. The very low transport efficiency along the $[1\bar{1}0]$ direction did not allow the realization of systematic measurements along this direction.

5.1 Acoustic carrier transport

The processes of carrier generation, capture, and transport by the SAW are illustrated in Fig. 5.1. The lateral extension of the spatial modulation of the QW along $\hat{x}$ is determined by the SAW wavelength λ_{SAW}. In the figure, the amplitude of the modulation along the z direction is exaggerated for better visualization, since in reality it is much smaller than the QW thickness. The incident circularly polarized laser light hits the sample at a spot G, which is placed on the SAW path. At G, the photoexcited carriers (electrons and holes) are spatially separated by the SAW potential and dragged along the wave propagation direction. Some of the carriers recombine during transport: the right and left circularly polarized PL intensities are then measured (as explained in section 4.3) and used to determine the degree of spin polarization along the transport path.

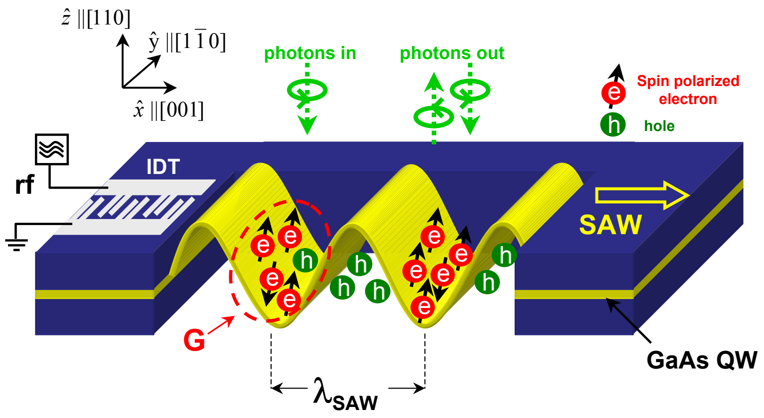

Figure 5.1: Illustration of the acoustic transport mechanism: carriers are optically generated at a spot G and transported by the SAW, which creates a lateral confinement potential with periodicity given by λ_{SAW}. The PL emitted along the path gives the degree of spin polarization of the electrons.

5.1.1 The role of the ZnO layer for carrier transport

Figure 5.2(a) shows a typical CCD image of the right circularly polarized PL emission from the transport channel obtained for sample B. The CW acquisition experiment was performed at T = 4 K using a nominal rf-power of $P_{\rm rf}$ = 19.5 dBm applied to the IDT. Band-pass filters were used in order to select the PL emission from the *e-hh* transitions of the 18 nm-thick QW. The carrier generation spot is indicated by G and the SAW propagation direction is shown by the arrow. The SAW launched by the focusing IDT defines a narrow (about 10 μm wide) transport channel. In the absence of an acoustic excitation, PL emission is only observed close to G. Under a SAW, in contrast, considerable recombination takes place along the SAW path. Although the nature of the radiative defects in this sample has not been studied in detail, we believe that they are due to lateral potential fluctuations induced by interface roughness and variations in the QW thickness. As discussed in subsection 4.1.2, these fluctuations can trap carriers and induce recombination, thus limiting the carrier transport to distances to approximately 20 μm, as observed in Fig. 5.2(a).

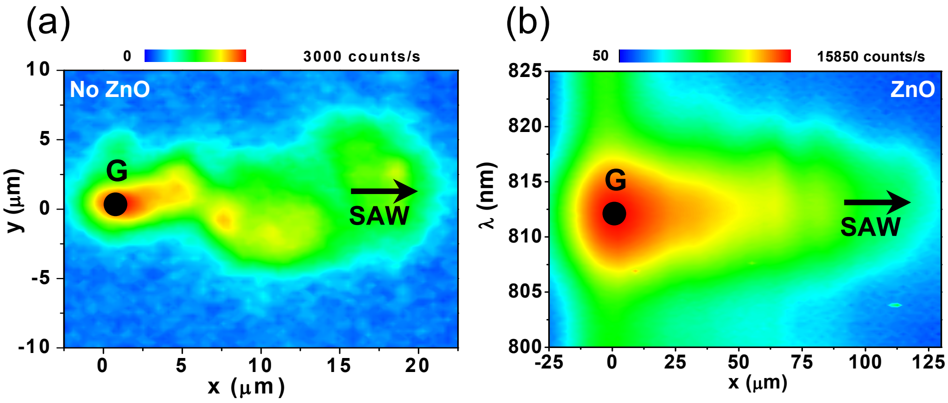

Figure 5.2: PL images of the acoustic transport in (a) Sample B, (b) Sample A, which was ZnO-coated. The transport takes place within the 18 nm-thick GaAs QWs in both structures [cf. Tables 4.1 and 4.2]. Note the difference in magnitude between the horizontal axes in both pictures.

A significant enhancement of the transport efficiency is achieved with the addition of a ZnO film. Figure 5.2(b) shows a PL image obtained for sample A under very similar conditions (T = 15 K and $P_{\rm rf}$ = 16 dBm) as in Fig. 5.2(a). The vertical axis is spectrally resolved. This measurement was performed by using the diffraction grating of the monochromator in order to select the emission energies around the *e-hh* transition around 812 nm [instead of band pass filters used to obtain the spatial image shown in Fig. 5.2(a)]. The acoustic channel in this case, is about 20 μm wide. We clearly observe a much more efficient carrier transport, which reaches distances exceeding 120 μm [note the different horizontal scales in Figs. 5.2(a) and (b)]. This considerable enhancement of the carrier transport distance is attributed to the piezoelectric ZnO layer deposited on top of the (Al,Ga)As structure containing the GaAs QW. The stronger potential produced by the piezoelectric layer, besides better screening of the *e-h* interaction, makes the transport less sensitive to potential fluctuations along the transport path. In contrast to Fig. 5.2(a), recombination along the carrier transport channel is much more homogeneous, demonstrating that the ZnO deposition is an important step to improve the transport efficiency.

5.1.2 Transport efficiency

Figure 5.3 presents the spatial dependence of the average PL intensity ($\mathrm{I_{PL}}$) integrated across the transport path of sample A for different rf-powers P_{rf} applied to the IDT. The squares display the PL profile in the absence of the SAW (right vertical axis). This profile is basically dominated by carrier diffusion and is, therefore, symmetric with respect to the generation spot. The PL intensity in the absence of a SAW [$\mathrm{I_{PL}}$(no SAW)] is approximately 5 times more intense than the profile measured at $P_{\mathrm{rf}} = 8$ dBm, which is shown together with the other P_{rf} values in the left vertical axis. For $P_{\mathrm{rf}} \geq 8$ dBm, $\mathrm{I_{PL}}$ at the generation spot decreases with the increase of the acoustic power. The PL profiles measured under acoustic power are asymmetric, with a much slower decay along the SAW propagation direction, thus demonstrating the carrier capture and subsequent transport along the acoustic channel. The increase of the SAW longitudinal piezoelectric field component (E_x) with the applied rf-power results in a stronger PL quenching at G (due to a more effective screening of the *e-h* interaction) and a more efficient carrier transport. In particular, the PL intensity at G for $P_{\mathrm{rf}} = 24$ dBm is about 90 times weaker as compared to the PL intensity in the absence of the SAW. A further increase in the acoustic power leads to a complete quenching of the recombination along the transport path. PL detection and, consequently, the analysis of the spin polarization ρ_z using the PL data becomes then very difficult under such conditions.

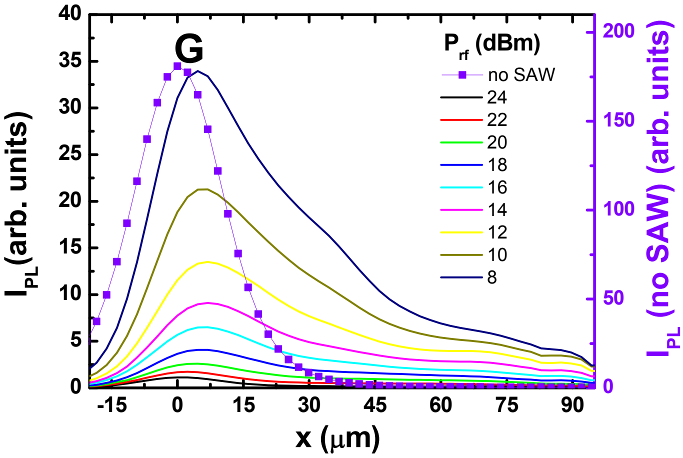

Figure 5.3: PL intensity (I_{PL}) integrated across the SAW beam recorded for sample A under different acoustic powers P_{rf}. I_{PL} reduces as the acoustic power increases, demonstrating the quenching of *e-hh* recombination at the generation spot G and the subsequent carrier transport. The squares (right vertical axis) present the PL intensity in the absence of the SAW [I_{PL}(no SAW)].

5.1.3 Band gap modulation

As pointed out in chapter 2, the SAW strain field induces a periodic modulation of the band gap of the semiconductor structure. The band gap modulation amplitude ΔE_g increases with the SAW amplitude and in weakly piezoelectric materials, like GaAs, is mainly attributed to the strain field. In this section, we analyze the band gap modulation of our multilayer structure and the effects introduced by the ZnO film on it by comparing the experimental results with the calculations described in chapter 2.

Figures 5.4 presents the PL spectra of the *e-hh* transition measured at T = 15 K for different values of P_{rf} in the ZnO-uncoated sample B. The PL intensity reduces with P_{rf}. The quenching is about a factor of 6 for a P_{rf} = 16 dBm as compared to the PL intensity in the absence of a SAW. In addition to the quenching, the shape of the PL lines changes as P_{rf} increases due to the band-gap modulation. A PL line splitting into two components is observed. The lower and higher energy components of the PL doublet correspond to the transition energies E_g^{min} and E_g^{max}, where the band gap energy E_g achieves its minimum and maximum values, respectively. As we have shown in subsection 2.3.2, in a (110) GaAs QW without a ZnO layer, due to the weak piezoelectric fields, the carriers are likely to populate a wide range of SAW phases, thus explaining the detection of the two energy components in the PL spectra.

The inset in Fig. 5.4 shows that the strain field also penetrates in the GaAs substrate, affecting the GaAs PL emission line. The splitting of the GaAs lines cannot be observed due to the wider FWHM of the substrate emission line and to the lower strain values at the substrate. A calculation reveals a difference of approximately 40% between the amplitude of the hydrostatic strain component S_0 in the QW and at the interface between the MBE layers and the substrate.

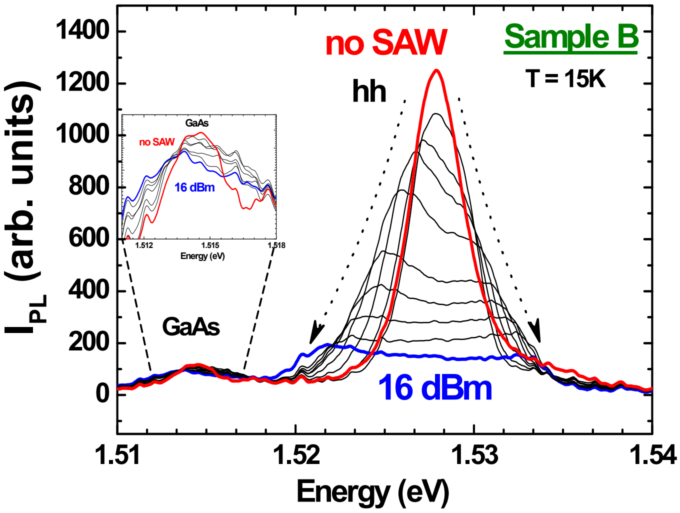

Figure 5.4: PL spectra as a function of SAW power for sample B. The inset corresponds to a zoom in the emission line of the GaAs substrate, showing the band splitting caused by the penetration of the SAW strain field.

Figure 5.5 displays the PL energy splitting ($\Delta E = E_g^{max} - E_g^{min}$) (filled squares) obtained from the data in Fig.5.4 as function of the effective acoustic power [cf. section 4.2]. The calculated values ($\Delta E = \Delta E_g^{max} + \Delta E_g^{min}$) [cf. subsection 2.3.2] which take into account the band gap modulation contribution induced by the SAW strain field are displayed by opened squares. The calculation was performed by taking into account the multilayer structure of sample B (Table 4.2). The calculated values agree very well with experimental ones, showing that in this case the main contribution to the band gap modulation of the structure arises from the SAW strain field.

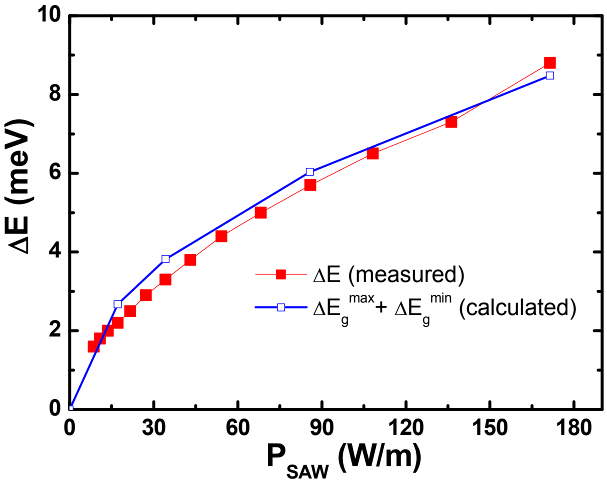

Figure 5.5: Experimental PL line splitting ΔE (filled squares) as a function of the effective acoustic power for sample B. The calculated values for ΔE_g taking into account the modulation due to the SAW strain field are shown by empty squares.

Figure. 5.6 displays similar measurements for sample A. In this case, the PL quenching is about 30 times for $P_{\mathrm{rf}} = 16$ dBm [note the logarithmic scale of the vertical axis of Fig. 5.6]. While $\mathrm{I_{PL}}$ reduces for $P_{\mathrm{rf}} > 6$ dBm, no line splitting is observed in this case. The SAW only red-shifts the *e-hh* PL emission line. According to Fig. 2.8(b), the electrons are transported close to the minimum band gap energy E_g^{min}, while the holes remain in positions where the band gap modulation almost vanishes. The detection of PL recombination at E_g^{min} suggests that the carrier recombination mechanism along the transport path in this (110) QW takes place when electrons transported by the SAW recombine with holes trapped in potential fluctuations [5].

The strain field also red-shifts the other emission lines observed in Fig. 5.6. In particular, the red-shift of the GaAs line is larger for sample A than for sample B due to the smaller separation between the QW and the substrate in the former.

The energy shift of the *e-hh* line with the acoustic power for sample A is larger than the one from the GaAs substrate. While the former one ranges about 4 meV, the latter is about 2.8 meV. This result can be understood by taking into account the stronger piezoelectric field due to the ZnO on the energy modulation of the *e-hh* transition for sample A. The filled squares in

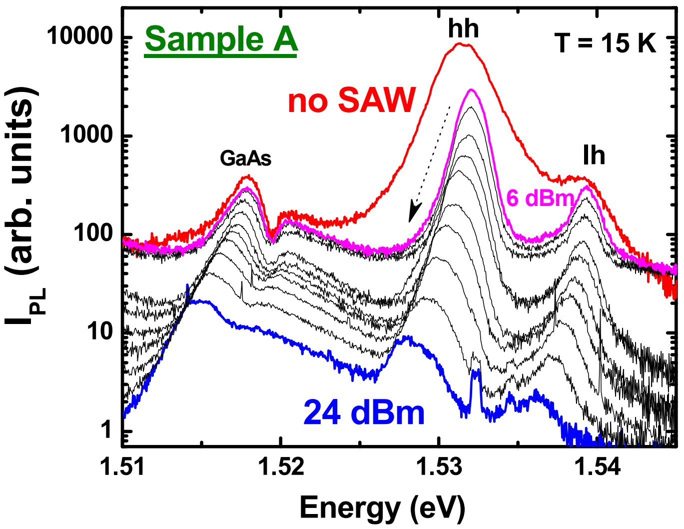

Figure 5.6: PL spectra as a function of SAW power sample A, which has a 500 nm-thick ZnO layer on top.

Fig. 5.7 show the energy shift ΔE_g^{min} as a function of the effective acoustic power P_{SAW}. The data points in this plot were obtained by fitting the spectra in Fig.5.6 with Gaussian curves in order to obtain the mean peak position for each P_{SAW}. ΔE_g^{min} was then calculated by subtracting from the mean energy position of the *e-hh* line for each rf-power the corresponding value in the absence of a SAW. In the presence of the ZnO, a small blue shift of the *e-hh* transition energy has always been observed in the very low power regime. For $P_{\mathrm{rf}} > 6$ dBm, a narrowing of the *e-hh* emission linewidth was also detected. These two effects may be related to each other, but we did not investigate their origin in detail.

The empty squares curve in Fig. 5.7 display values of ΔE_g^{min}, calculated taking into account only the band gap modulation introduced by the strain field. A qualitative agreement is found for low acoustic powers, although the calculations cannot account for the observed blue shift. However, as P_{SAW} increases, the measured energy shift becomes considerably larger than the expected contribution from the band gap modulation due to the strain.

Let us now analyze the effects of the piezoelectric field on the band gap modulation. As pointed out in subsection 2.3.2, an electric field parallel to the growth direction of a 2D system induces the spatial separation of electrons and holes via the Quantum-Confined Stark Effect (QCSE).

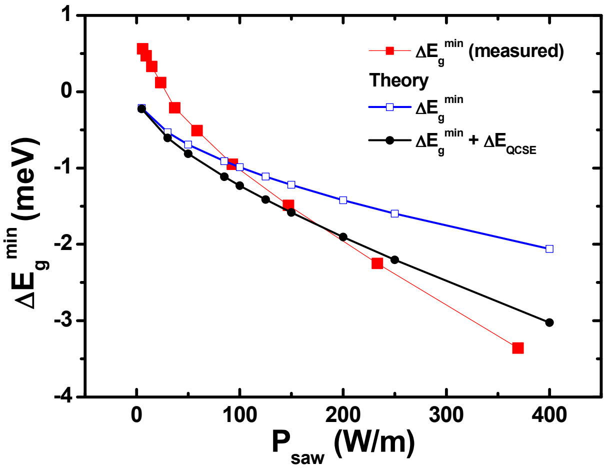

Figure 5.7: Experimental ΔE_g^{min} (filled squares) as a function of the effective acoustic power for sample A. The calculated values of ΔE_g^{min} taking into account only the modulation due to the strain field (empty squares) and strain plus the piezoelectric-field-induced QCSE (circles) are also shown.

[15, 81, 114, 119, 120] This field shifts the wave functions of electrons and holes towards opposite QW interfaces, suppressing carrier recombination and leading to a red-shift of the PL emission line. The energy shift due to the QCSE induced by an electric field E_z for a particle with effective mass m^*, in a QW of effective thickness d_{eff} is given by [15]:

$$\Delta E_{QCSE} = -\frac{1}{8}\left[\frac{1}{3}-\frac{2}{\pi^2}\right]^2 \frac{m^* e^2 d_{\text{eff}}^4}{\hbar^2}\mathrm{E}_z^2. \tag{5.1}$$

Since the effective mass of the holes m_0^h is much larger than the electron effective mass m_0, the major contribution to the QCSE energy shift is determined by the contribution from the valence band. We use $m^* \approx m_0^h$ $= 0.45\ m$ [15] and a 1 nm wave function penetration in each of the QW barriers, so that $d_{\text{eff}} = 20$ nm.

The dotted curve shown in Fig. 5.7 was calculated by including the energy shift ΔE_{QCSE} given by equation (5.1) to the energy shift calculated from the strain contribution. The agreement is significantly improved, specially for higher acoustic powers, demonstrating that the SAW-induced energy shift on the *e-hh* emission results from a combined contribution of both strain and piezoelectric fields. The absolute values calculated for ΔE_{QCSE} depend on the piezoelectric properties of the ZnO layer as well as on the wave function penetration into the QW barriers. In the former case, as we pointed out in chapter 2, the calculations assume a complete orientation of the ZnO crystallites along the c-axis. However, a distribution of orientations around the c-axis as well as the presence of crystallites with opposite polarization may decrease the piezoelectricity in comparison to a fully c-axis oriented film [62]. On the other hand, the dependence of ΔE_{QCSE} on d_{eff}^4 makes it very sensitive to this parameter. The value assumed here for the penetration into the barriers is 1 nm. The real value can, however, be higher and may account for the lower calculated values for ΔE_g^{min} for high P_{SAW} as compared to the measured ones.

5.2 Acoustic spin transport

This section is devoted to the investigation of spin transport in (110) GaAs QWs using polarization-resolved PL measurements. We first demonstrate the acoustically induced spin transport, based on the analysis of the PL polarization collected along the SAW path in the [001] direction. In the following, we discuss the spin relaxation properties in the absence of external magnetic fields. We try to identify the relevant spin relaxation mechanisms acting on the spin ensembles by looking on the results obtained under different light intensity, sample temperature, and acoustic power.

5.2.1 The role of the ZnO layer for spin transport

Figure 5.8(a) presents profiles of the right (I_R) (squares) and left (I_L) (dots) circularly polarized PL, recorded at T = 4 K along the transport path on sample B (i.e., without the ZnO coating). The carriers were generated by a left circularly polarized laser beam focused at x = 0 (spot G). The solid line shows, for comparison, I_R in the absence of a SAW. The PL intensity at the generation spot is approximately 20 times weaker when a SAW power P_{rf} = 19.5 dBm is applied. As already observed in Fig. 5.2(a), the acoustic carrier transport in sample B is strongly affected by potential fluctuations along the transport path. The wavy PL profiles displayed in Fig. 5.8(a) also show a spatial modulation with a period comparable to the SAW wavelength λ_{SAW}. The latter is attributed to acoustic interference[1]. This interference

---

[1] The mask used to design the IDTs on sample B included two faced IDTs. Therefore, the SAW launched by one of the IDTs along the [001] direction can be reflected by the

also avoids a smooth decay of the PL emission along x. Note that the intensity I_R is higher than I_L along the whole channel, showing that a non-zero electron spin polarization is being transported (we assume that the hole spins relax much faster the electron ones [129]).

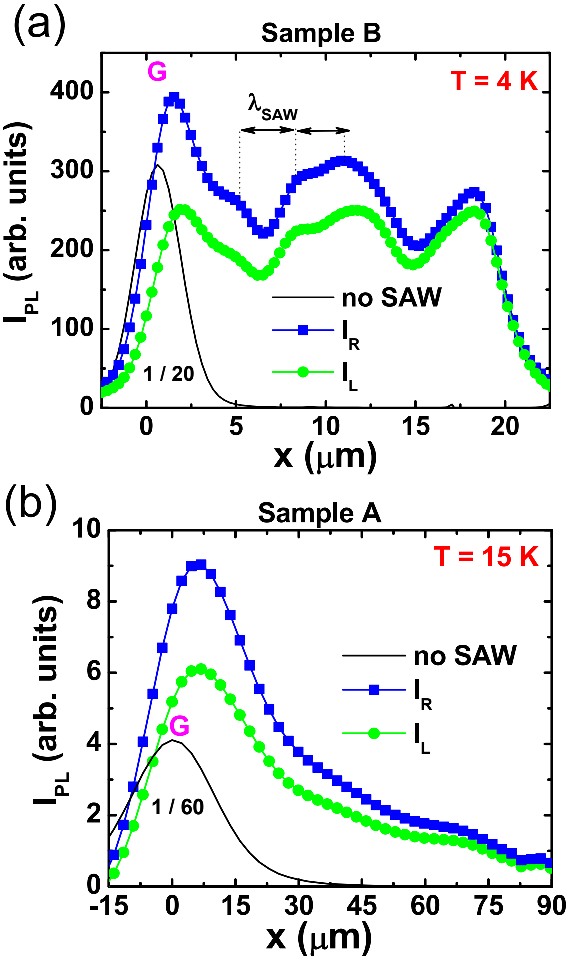

Figure 5.8: PL profiles of the right I_R and left I_L circularly polarized light demonstrating a net spin transport along the SAW channel in (a) sample B (without ZnO) and (b) sample A (ZnO-coated). The solid lines show the PL profiles in the absence of a SAW.

Figure 5.8(b) displays the spatial dependence of I_R (squares) and I_L (dots) recorded at 15 K for the ZnO-coated sample A. The solid line shows again I_R in the absence of a SAW, where the PL profile is determined by

---

second one and interfere with the incoming wave front along the transport path.

carrier diffusion[2] and practically vanishes for $|x| \geq 20$ μm. When a SAW is generated by applying a $P_{\text{rf}} = 16$ dBm to the IDT, a strong reduction of I_R and I_L (by a factor of approx. 30) takes place at x = 0 as the photogenerated carriers are transported away from G. In addition, I_R also remains above I_L along the whole measured spatial range.

Figure 5.9 shows the spatial dependencies of the spin polarization ρ_z extracted from Figs. 5.8(a) and (b). The spin polarization decay is faster for sample B (squares). An exponential fit to the data (solid black line) yields a spin transport length (spin decay length) of $l_s = 15$ μm. The spin depolarization is considerably slower for the sample A (circles). An exponential fit (red solid line) yields, in this case, a spin transport length of $L_s = 64$ μm. As we will show in the discussion of time-resolved experiments in chapter 6, the strong carrier confinement induced by the piezoelectric field in the ZnO coated sample ensures that the transport length and the spin lifetime (τ_z) are related to each other by $L_s = v_{\text{SAW}}\tau_z$, where v_{SAW} is the SAW propagation velocity. This expression yields a spin lifetime $\tau_z = 22$ ns for the case of a SAW propagating along the x $\|$ [001] direction, with $v_x = 2930$ m/s (the propagation velocity of the spins for sample A will be determined in chapter 6). These are the longest spin lifetime and transport length reported for spin transport in (110) GaAs quantum wells [35].

At this point, we conclude that the enhancement of the piezoelectric field induced by the ZnO layer is crucial for the improvement of the carrier as well as of the spin transport efficiencies. Therefore, from now on, expect when stated, our focus will be to the analysis of the spin relaxation dynamics in the ZnO-coated sample A.

5.3 Spin relaxation during acoustic transport

The orientation of the SO-field in a symmetric (110) GaAs QW [equation (3.9)] predicts vanishing relaxation via the DP mechanism for z-oriented spins. However, Fig 5.9 demonstrates that, even under the strong confinement induced by the SAW piezoelectric potential, the spins live slightly longer than 20 ns. In the following subsections, we address the mechanisms limiting the spin lifetime in our system.

---

[2] The larger diameter of the laser spot in Fig. 5.8(b) in comparison to (a) is due to the 20× magnification objective used in the former. The experiments on sample B shown in Fig. 5.8(a) were performed with a 50× objective, what creates a 2.5 smaller laser spot.

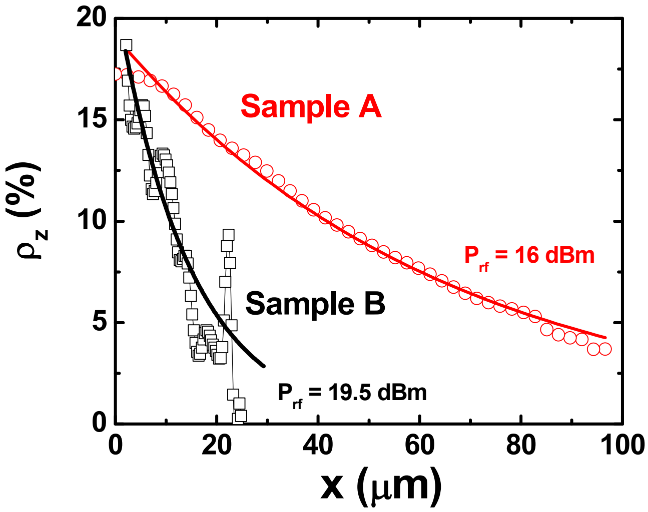

Figure 5.9: Spin polarization decay obtained from the PL profiles displayed in Fig. 5.8(a) and (b) for sample B (squares) and sample A (circles), respectively. The solid lines correspond to exponential fits.

5.3.1 Light intensity

The role of the Bir-Aronov-Pikus spin relaxation mechanism, associated with the electron-hole interaction, can be checked by changing the light excitation power (P_{ex}) and consequently changing the carrier density generated by the laser beam [1, 105]. Figure 5.10 displays on a logarithmic scale the decay of the spin polarization for different values of P_{ex}. For x $>$ 15 μm (and for the whole spatial range for the low light excitation intensities), the spin relaxation rates are essentially independent on P_{ex}, thus indicating that the long-range acoustic transport is not limited by the *e*-*h* exchange interaction. For high illumination intensity ($P_{\mathrm{ex}} = 10$ μW curve), ρ_z decays faster close to the generation spot (x $<$ 15 μm). The latter is attributed to the BAP mechanism induced by the large concentration of carriers injected at G. As the carriers are taken away from the generation spot, BAP relaxation is virtually eliminated.

Exponential fits of the long decay regime for the three pumping powers in Fig. 5.10 provide spin transport distances of approximately 45 μm. This value is smaller than the one of 64 μm obtained from the fit in Fig. 5.9 due the lower acoustic power ($P_{\mathrm{rf}} = 10$ dBm) used in the present measurements. At low light intensity, as well as high temperatures (T), the PL emitted along the transport path decreases considerably. Therefore, in order to have a reasonable luminescence intensity along the channel, it was necessary to reduce the acoustic power. The dependence of the spin transport length on the applied acoustic power will be discussed in detail in subsection 5.3.3.

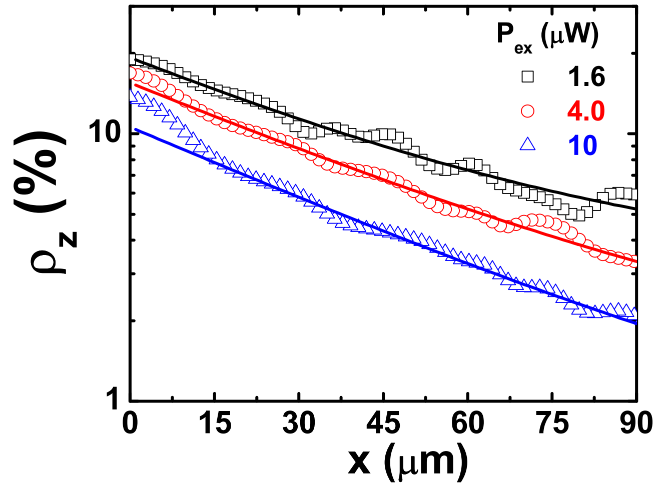

Figure 5.10: Dependence of spin polarization during transport on light excitation power P_{ex} for sample A, recorded at T = 15 K and using P_{rf} = 10 dBm. The solid lines are exponential decay fits to the data.

5.3.2 Temperature

To confirm the suppression of the BAP relaxation during acoustic transport, we have also performed experiments under different temperatures. The efficiency of the BAP spin relaxation mechanism should reduce if the temperature is high enough to prevent exciton formation. Figure 5.11 displays spin polarization profiles recorded at different temperatures, under a fixed acoustic power $P_{\text{rf}} = 9$ dBm. The profiles are essentially temperature independent up to 75 K. Reliable spin transport measurements could not be carried out above 80 K due to the reduced transport efficiency. Previous works on (110) GaAs QWs have reported an enhancement of the relaxation time of optically injected spins with temperature in the range from 10 to 120 K [45, 105]. This behavior has been attributed to the reduction of the electron-hole correlation with temperature, which weakens the BAP mechanism. The invariance of the spin transport length with temperature further confirms the suppression of the BAP mechanism by the spatial separation of electrons and holes in the type-II potential confinement associated with the acoustic wave [37].

Note that the invariance of the spin relaxation rates with temperature during acoustic transport also indicates no significant contribution from the Elliott-Yafet mechanism. According to Zutic' [151], the EY mechanism leads a temperature dependence of the spin relaxation given by $\tau_z \sim \tau_p/T^2$ in non-degenerate semiconductors. The absence of EY in our experiments agrees with previous temperature dependent spin relaxation measurements in (110) QWs [1, 45, 105].

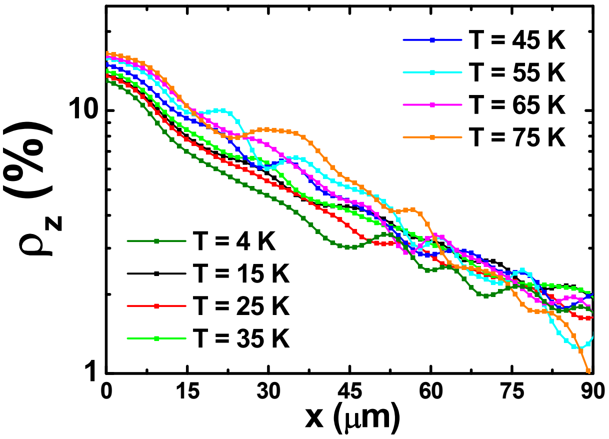

Figure 5.11: Spin depolarization along the transport channel recorded at different temperatures using $P_{\rm rf} = 9$ dBm and $P_{\rm ex} = 4$ μW.

5.3.3 Acoustic power

The spin lifetimes for z-oriented spins were shown to be independent of temperature and carrier density, demonstrating that not only the DP, but also the BAP relaxation mechanism is suppressed during acoustic transport. In this subsection, we address the role of the SAW fields on the spin relaxation process. We show that the acoustic power does affect the spin relaxation rates, allowing us to get important insight into the most relevant relaxation mechanisms during acoustic transport in our (110) QWs.

Before addressing the dependence of the spin transport length on acoustic power it is important to make some remarks about the carrier transport efficiency. Figure 5.12 displays on a logarithmic scale PL profiles (which have been normalized with respect to the intensity at the generation spot G) recorded along the transport path for different values of $P_{\rm SAW}$. These PL profiles are the same ones presented in Fig. 5.3. The solid lines show the

PL profiles characterizing the carrier recombination along the transport path in the low acoustic power regime. For $P_{\text{SAW}} \leq 6$ W/m, the luminescence profile resembles the one in the absence of a SAW, except for showing a slower decay towards the SAW propagation direction. The transport threshold is achieved for $P_{\text{SAW}} = 9$ W/m, where carrier transport over longer distances is observed. The carrier transport length and the PL intensity along the path increase slightly for P_{SAW} between 9 and 23 W/m and saturate for $23 < P_{\text{SAW}} < 146$ W/m (filled square curves). The carrier transport length, therefore, does not depend on the effective acoustic power over approximately one order of magnitude in acoustic power. An exponential fit to the PL decay (not shown) yields a carrier transport length $L \approx 47$ μm. A calculation of the amplitude of the longitudinal piezoelectric field responsible for the spatial separation and transport of electrons and holes, yields $\mathrm{F}_x \approx 1.6$ kV/cm for $P_{\text{SAW}} = 25$ W/m. This value agrees with the one expected for exciton dissociation in GaAs QWs [100, 113], once more confirming the complete suppression of electron-hole interaction in this transport regime. In the limit of high powers, i.e. $P_{\text{SAW}} > 150$ W/m (opened square curves), the very high acoustic fields considerably quench the carrier recombination along the path. The carrier transport lengths in this regime probably exceed 47 μm. A precise determination of the carrier and spin transport length under these conditions, however, becomes difficult and much less precise due to the very low intensities of I_R and I_L.

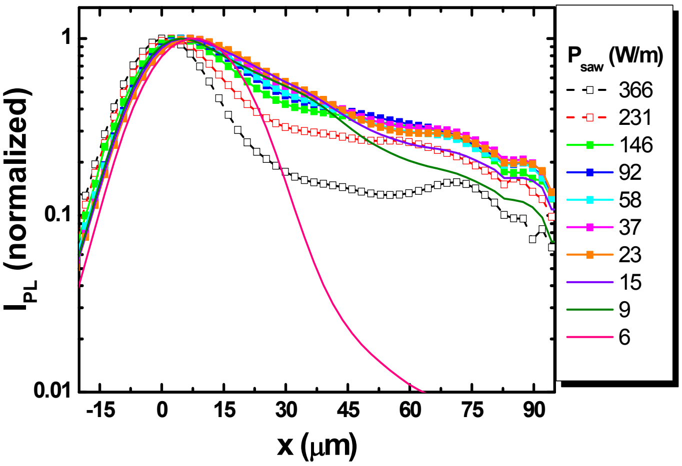

Figure 5.12: Normalized PL intensity emitted along the transport channel for different effective acoustic powers P_{SAW}, recorded at 15 K.

The dependence of the spin lifetime τ_z on the effective acoustic power P_{SAW}, obtained from the PL profiles shown in Fig. 5.12, is displayed in Fig. 5.13(a) (left axis). The corresponding values for the spin transport length L_s, which are displayed on the right axis, increase from 35 μm up to approximately 70 μm with the increase of the acoustic power. Since the carrier transport length is independent on P_{SAW} in this power range, the enhancement of the spin transport length cannot be attributed to an increased carrier transport efficiency. This result shows, therefore, that the acoustic power can be used to tune the spin relaxation rate in sample A.

The spin lifetimes increase up to effective acoustic powers around 90 W/m

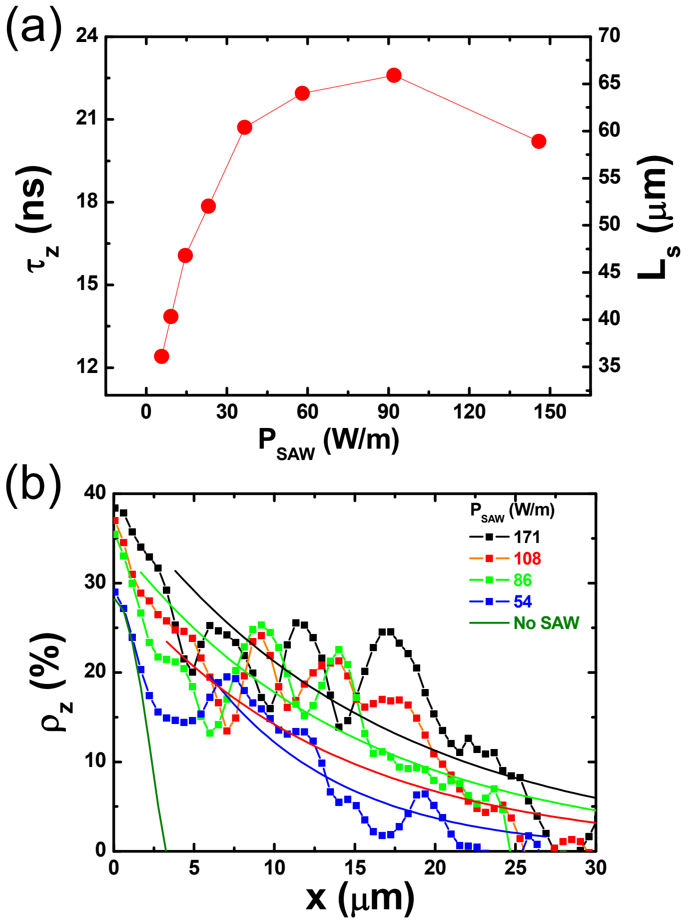

Figure 5.13: (a) Dependence of the spin relaxation time (left) and spin transport length (right) on the effective acoustic power for sample A. The lifetimes were obtained from the relation $\tau_z = L_s/v_x$, with $v_x = 2930$ m/s. (b) Spin polarization profiles for different acoustic power obtained for sample B.

and seem to reduce for higher acoustic powers. This observation suggests that SAW-related spin relaxation mechanisms become relevant at high power levels. As we will show in the following, this happens mainly due to the enhanced strain and piezoelectric fields induced by the ZnO film.

We did not observe such a pronounced effect of the acoustic power on the spin decay rates for sample B. This is shown in Fig. 5.13(b), which displays the spin polarization profiles as a function of P_{SAW} obtained under similar experimental conditions as for sample A. An accurate determination of the decay lengths in this case is hindered because of the presence of acoustic interferences and inhomogeneities in the PL emission along the transport path. However, no significant change in the relaxation rates as compared to sample A is detected. The exponential fits (solid lines) in Fig. 5.13(b) yield a variation in l_s between 11 and 15 μm for P_{SAW} between 54 and 171 W/m.

We attribute the discrepancy between the spin lifetime dependence on the SAW power for the two samples to the effects introduced by the stronger piezoelectric fields experienced by the carriers in sample A due to the deposition of the ZnO film. The suppression of spin relaxation with increasing acoustic power (for $P_{\mathrm{SAW}} < 90$ W/m) observed in Fig. 5.13(a) is attributed a progressive confinement of the spins within narrow channels with widths much smaller than λ_{SAW} aligned along the SAW wavefronts (cf. Fig. 5.1). The effects of mesoscopic confinement on the spin lifetimes have been demonstrated in dynamic quantum dots [29, 132] and in quasi-1D structures [74, 89, 97]. Intuitively, the enhancement of the spin lifetimes arises from the motional narrowing associated with electron scattering at the potential boundaries of the narrow channels.

In principle, motional narrowing induced by doping [1, 105] or by lateral confinement [89] is not expected to suppress the relaxation of z-oriented spins in (110) GaAs QWs. Spin relaxation suppression due to scattering relies on the existence of **k**-dependent internal magnetic fields, in general not aligned with the electron spin, which quickly randomize the average spin of an ensemble. In the case of nominally symmetric (110) QWs, however, the internal magnetic field due to the SO-coupling is always parallel to the growth direction and does not contribute to the relaxation of z-oriented spins. Therefore, higher momentum scattering rates are only effective if in-plane effective fields are present [cf. equation 3.17]. Such fields can be induced by asymmetric confinement potentials due to differences between the two QW interfaces, which may appear even in high-quality (110) QWs [68, 82, 92]. These asymmetries lead to built-in SIA effective magnetic fields $\mathbf{B}_{\mathrm{SO}}(\mathbf{k})$ with an in-plane component. As we will demonstrate in chapter 6, the D'yakonov-Perel' relaxation associated with this component leads to quick randomization of the average ensemble spin via carrier momentum fluctuations, leading to spin relaxation.

The effectiveness of mesoscopic confinement for spin relaxation suppression depends on the ratio between the confinement dimensions and the spin-orbit length (λ_{SO}) of the electron spins. λ_{SO} is defined as the ballistic transport distance required for a precession angle of 1 rad around the internal magnetic field $\mathbf{B}_{\mathrm{SO}}(\mathbf{k})$ arising from the SO-interaction. λ_{SO} must be larger than the confinement dimension (x_c) in order to allow for the suppression of the spin relaxation via motional narrowing induced by momentum scattering on the potential boundaries [131]. The lateral carrier confinement during acoustic transport is limited by the SAW wavelength (λ_{SAW}), as illustrated in Fig. 5.14(a). When $\lambda_{SO} >> x_c$, the precession angle ($\Omega_{\mathrm{SO}}\tau_p$) of the spin vector around the SO-field between two boundary scattering events is very small. In this case, scattering conserves the spin component along the z-direction. On the other hand, when $\lambda_{SO} < x_c$ [Fig. 5.14(b)] the spin precession angles and, consequently, the spin relaxation rates are larger.

In order to determine the ratio between the SO-length and the carrier

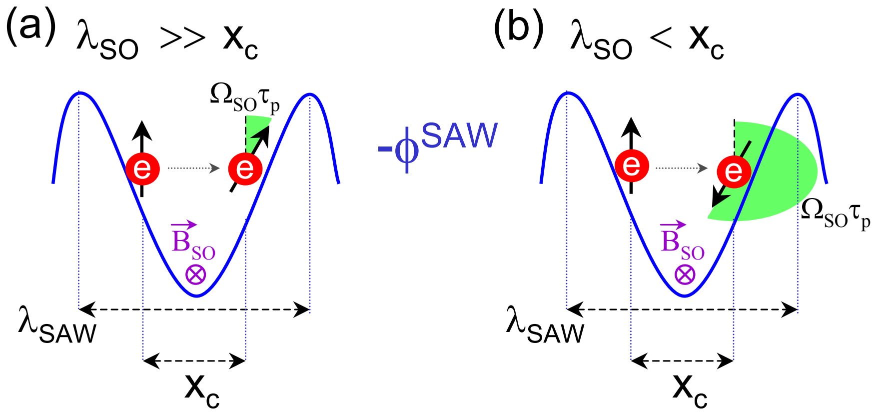

Figure 5.14: Illustration of the spin scattering in the SAW potential (ϕ^{saw}): (a) An electron crosses the confinement direction and scatters at the potential boundary. If $\lambda_{SO} >> x_c$, the precession around $\mathbf{B}_{\mathrm{SO}}$ is small and the spin orientation is expected to be preserved. (b) When $\lambda_{SO} < x_c$, spin memory is lost after scattering.

lateral confinement distance, we derive in the following an expression for the SO-length associated with the in-plane spin component. As we will show, the expression for λ_{SO} does not depend on carrier momentum, being, therefore, general. For an electron moving with velocity v, the SO-length is given by:

$$\lambda_{SO} = \frac{v}{\Omega_{\mathrm{SO}}}, \tag{5.2}$$

where Ω_{SO} is the precession frequency around the effective field to which the spin component is sensitive.

When a spin vector initially oriented along z is rotated by an in-plane magnetic field, the in-plane spin component becomes sensitive to the DP internal magnetic field [equation (3.9)], which induces precession with frequency $\Omega_{\mathrm{SO}} = \Omega_{\mathbf{int}}$. Therefore, using $v = \hbar k_y/m_0$ and the expression for $\Omega_{\mathbf{int}}$, we obtain:

$$\lambda_{SO} = \frac{2\hbar^2}{\gamma m_0}\left[\frac{d_{\mathrm{eff}}}{\pi}\right]^2. \tag{5.3}$$

Using $\gamma = 18$ eV$\mathring{A}^3$ (this value will be experimentally determined in Chapter 6), and assuming[3] $d_{\mathrm{eff}} = 20$ nm, equation (5.3) yields $\lambda_{SO} = 5.2$ μm.

For acoustic transport, the average lateral carrier confinement length (x_c) depends on λ_{SAW} and on the amplitude of the SAW piezoelectric potential (ϕ^{saw}). The sinusoidal spatial distribution of ϕ^{saw} can be approximated around the minimum of the electron energy (at $x = x_e$) by:

$$\phi^{saw}(x) = \phi_0 \cos(\mathrm{k_{SAW}} x) \approx \frac{1}{2}\phi_0 \mathrm{k}_{\mathrm{SAW}}^2 (x - x_e)^2, \tag{5.4}$$

where ϕ_0 is the SAW piezoelectric potential amplitude and $\mathrm{k_{SAW}} = 2\pi/\lambda_{\mathrm{SAW}}$. The average confinement distance can be estimated by:

$$x_c = 2\sqrt{\langle (x - x_e)^2 \rangle} = \frac{\lambda_{\mathrm{SAW}}}{\pi}\sqrt{\frac{2k_{\mathrm{B}}\mathrm{T}}{\phi_0}}, \tag{5.5}$$

with k_{B} as the Boltzmann constant. Using the numerical procedure described in chapter 2, we calculate ϕ_0 expected for our multilayer structure. Even for a low acoustic power of 5 W/m, we obtain $\phi_0 = 60$ mV, which at T=15 K corresponds to $x_c = 0.35$ μm $\ll \lambda_{SO}$.

---

[3] Note that we are adopting a lower limit for λ_{SO}, since the 1 nm assumed for the barrier penetration is, in general, the minimum expected value. For 2 nm penetration, for example, $\lambda_{SO} = 6.3$ μm.

In the collision dominated regime, the electron spin relaxation rates can be affected by changes in the momentum scattering time τ_p ($1/\tau_z \propto \tau_p$), which can be induced by changes on ϕ_0. The rise on the spin lifetimes with P_{SAW} observed in Fig. 5.13(a) can, therefore, be mainly attributed to the decrease on τ_p, which can be estimated by the ratio between x_c and the electron thermal velocity v_{T}. We obtain:

$$\tau_p = \frac{\lambda_{\mathrm{SAW}}}{\pi}\sqrt{\frac{m_0}{\phi_0}}. \tag{5.6}$$

In the range of P_{SAW} from 5 W/m to 60 W/m, ϕ_0 is calculated to lead to a relative decrease on τ_p by a factor 1.9, which agrees very well with the experimental variation of τ_z with P_{SAW} in this acoustic power range.

The spin lifetimes in Fig. 5.13(a) reach a maximum for $P_{\mathrm{SAW}} \approx 90$ W/m and decrease for higher values of P_{SAW}. Under these strong acoustic powers, we also have to consider spin relaxation processes associated with the SAW strain and piezoelectric fields. The effective magnetic field felt by the electrons can be obtained from the expected values for the Larmor frequency $\Omega_{\mathrm{s}}^{\mathrm{R}}$ associated with the strain [equation (3.27)] and $\Omega_{\mathrm{br}}^{\mathrm{R}}$ due to the Bychkov-Rashba field [equation (3.24)] presented in chapter 3.

Using the numerical procedure described in chapter 2 to calculate E_z and S_{xz}, we display in Fig. 5.15(a) the amplitude of these precession frequencies over a SAW cycle for a Rayleigh wave propagating along the [001] direction for $P_{\mathrm{SAW}} = 140$ W/m. The SAW piezoelectric field is displayed in the right vertical axis. The minimum of the electronic energy ($-e\phi^{saw}$), where the electrons are expected to be trapped during transport, coincides with a position where the piezoelectric and strain induced effective magnetic fields are expected to be close their maximum amplitudes. The amplitude of the total effective magnetic field induced by the SAW ($|\mathrm{B}_{\mathrm{SAW}}|$) can be estimated from the amplitude of the strain and piezoelectric Larmor frequencies at the minimum of ϕ^{saw} from the expression:

$$\mathbf{B}_{\mathrm{SAW}} = \frac{\hbar}{g_e\mu_B}[\Omega_{\mathrm{s}}^{\mathrm{R}} + \Omega_{\mathrm{br}}^{\mathrm{R}}]\ \hat{y} = -\frac{C_3\mathrm{S}_{xz} + r\mathrm{E}_z}{g_e\mu_B}\langle k_x\rangle\ \hat{y}, \tag{5.7}$$

where the average carrier momentum [$\langle k_x\rangle = m_0 v_x/\hbar$] is determined by the acoustic velocity $v_x = 2930$ m/s.

Figure 5.15(b) displays the values for $|\mathrm{B}_{\mathrm{SAW}}|$ as a function of P_{SAW} calculated at the position where the electrons are expected to the confined, i. e., at $x = x_e \approx 1.4\ \mu$m. As we observe, for high acoustic powers the effective magnetic field experienced by the electrons during tranport is expected to be of a few mT. As we show using Hanle effect measurements in the next chapter, fields with such magnitudes can affect the spin relaxation rates. Such field transforms the motional narrowing regime of the electron spins at low acoustic powers into a very slow precession motion around the average SAW-induced effective magnetic field, thus explaining the decrease of the spin lifetimes measured at $P_{\mathrm{SAW}} = 146$ W/m.

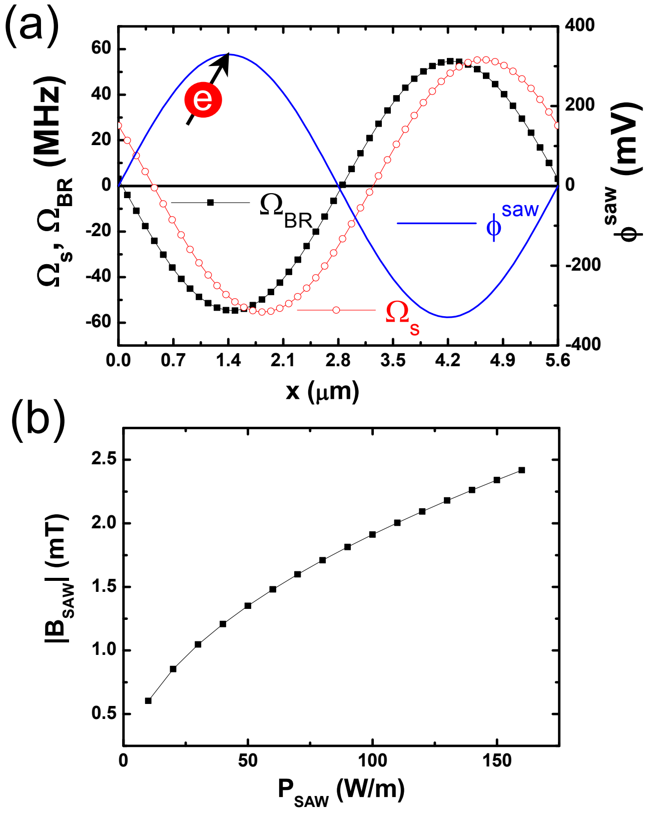

Figure 5.15: (a) Larmor precession frequencies $\Omega^{\mathrm{R}}_{\mathrm{s}}$ and $\Omega^{\mathrm{R}}_{\mathrm{br}}$ induced by the SAW strain and piezoelectric fields, respectively, over one SAW cycle. On the right vertical axis, the amplitude of the SAW piezoelectric field is displayed. (b) Calculated effective magnetic field induced by the SIA like contribution of the SAW fields to spin relaxation, analyzed at the minimum of the electronic energy $(-e\phi^{saw})$ in (a).

Chapter 6

Spin manipulation during acoustic transport

The very long spin lifetimes demonstrated in chapter 5 create ideal conditions for spin manipulation using external fields. In this chapter, we focus on the spin dephasing dynamics probed in sample A by time-resolved (TR) experiments. The TR analysis of the spin polarization shows that the confinement induced by the SAW potential allows for the transport of carriers with a well-defined average momentum, determined by the SAW propagation velocity. The spin relaxation times obtained under these conditions confirm the results obtained in the CW experiments presented in the previous chapter. Moreover, we show that the D'yakonov-Perel' mechanism delivers the main contribution to the spin dephasing under external magnetic fields. The well-defined velocity of the propagating spin packets allows for the study of the dependence of the SO-coupling on carrier momentum orientation. This is carried out by analyzing the spin dephasing dynamics under acoustic transport along the [001] and [$1\bar{1}0$] directions. The comparison between the theoretical model presented in chapter 3 with the data yields the average internal magnetic field associated with the BIA [$\langle \mathbf{B}_{\mathrm{int}} \rangle$], as well as the SO-coupling constant [γ] for GaAs.

Hanle effect experiments are also presented in order to describe the spin dephasing during acoustic transport in CW experiments. We obtain a good agreement between the Hanle effect model developed in chapter 3 and the TR experiments, thus demonstrating another possibility for studying the spin dephasing dynamics under external magnetic fields.

6.1 Coherent spin transport

In this section, we analyze TR acoustic transport experiments in the absence of external magnetic fields. As discussed in subsection 5.3.3, the carrier transport length does not dependent on the acoustic power over a wide rf-power range. The main question we address here is whether the carriers are transported coherently by the SAW, so that we can associate the spin transport lengths with the spin lifetimes. We show in the following that the spin packets indeed propagate with velocities very close to the SAW propagation velocities along the [001] and [$1\bar{1}0$] directions. This result supports the analysis of the spin relaxation mechanisms performed in section 5.2, where we assumed in some cases that the spin packets propagate with an average carrier momentum determined by the acoustic velocity.

6.1.1 Spin relaxation along the [001] direction

Figure 6.1(a) illustrates the TR carrier dynamics during SAW-induced transport. The PL intensity with right circular polarization (I_R) was integrated over the emission line of the *e-hh* transition. The experiment was performed at T = 15 K employing an rf-power P_{rf} = 20 dBm. The four images were obtained during transport along the $\hat{x} \parallel$ [001] direction for different delay times (Δt) between the laser excitation pulse and the PL detection (at Δt = 0.2, 4.2, 8.2, and 12.2 ns, respectively). Note that, within the time interval of approximately 12 ns, the spin packet propagates along the SAW path over a distance of ≈ 30 μm away from the generation spot G.

Figure 6.1(b) displays profiles of I_R and I_L integrated across the spectral width of the images shown in Fig.6.1(a). The spatial width of the packet exceeds the acoustic wavelength due to the size of the light excitation spot. This can be seen in the top image of Fig. 6.1(a) (Δt = 0.2 ns), which shows that the generation spot G has a diameter of approximately 10 μm ≈ $2\lambda_{\mathrm{SAW}}$.

The difference between the intensities of I_R and I_L in the profiles shown in Fig. 6.1(b) demonstrates again the transport of a net spin polarization along the SAW channel. The corresponding values of ρ_z as a function of Δt are displayed in Fig. 6.2(a) (squares). The spin polarization values were averaged over a short range of ± 1 μm around the mean packet position for every value of Δt. In this way, we are analyzing the polarization of spin packets transported within the same SAW cycle. The dashed line is a fit to an exponential decay, which yields a spin relaxation time $\tau_z = (22 \pm 2)$ ns. The mean packet position (x_c) is plotted as a function of Δt in Fig. 6.2(b). The solid line is a linear fit to the data, which yields a spin propagation velocity along the [001] direction of $v_x = (2930 \pm 100)$ m/s. This value is very similar to the one obtained from the calculations (2905.7 m/s) and from the IDT reflectance curve at room temperature ($v_{\mathrm{SAW}} = \lambda_{\mathrm{SAW}} f_{\mathrm{SAW}} =$

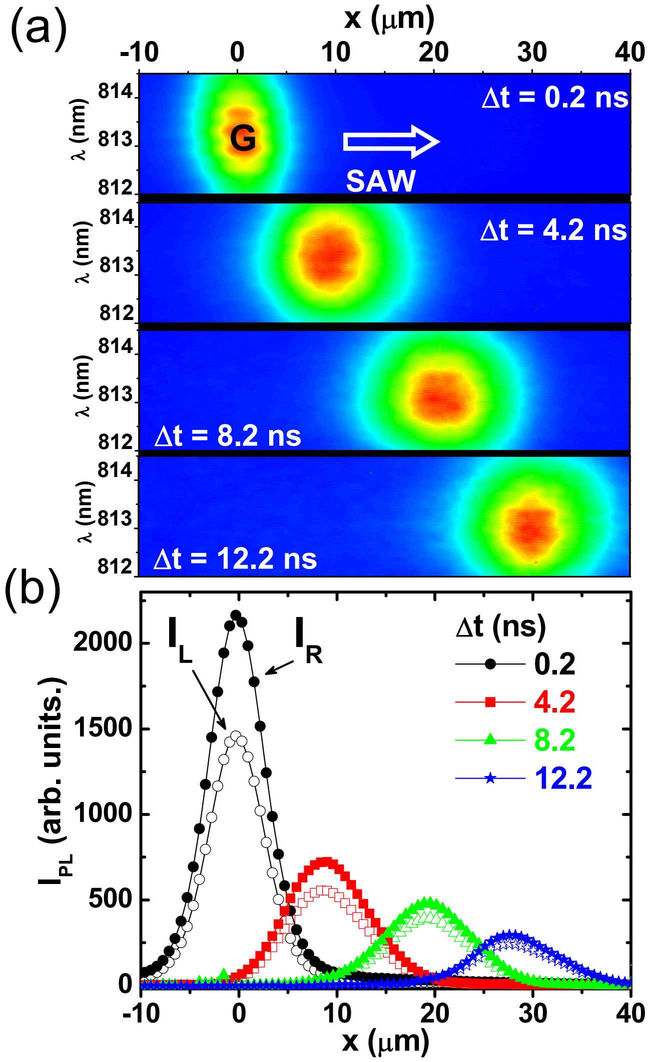

Figure 6.1: (a) Stroboscopic images showing the *e-hh* PL emitted during acoustic transport along the [001] direction at $\Delta t = 0.2$, 4.2, 8.2, and 12.2 ns. (b) PL intensity with right I_R (filled dot profiles) and left I_L (empty dot profiles) circular polarization measured for the delays Δt shown in (a).

2884 m/s), thus demonstrating that the packets are indeed transported with the SAW propagation velocity. In addition, we obtain $L_s = v_x \tau_z = (63 \pm 5)$ μm for the spin transport length, in agreement with the values obtained in the CW transport measurements presented in section 5.2.

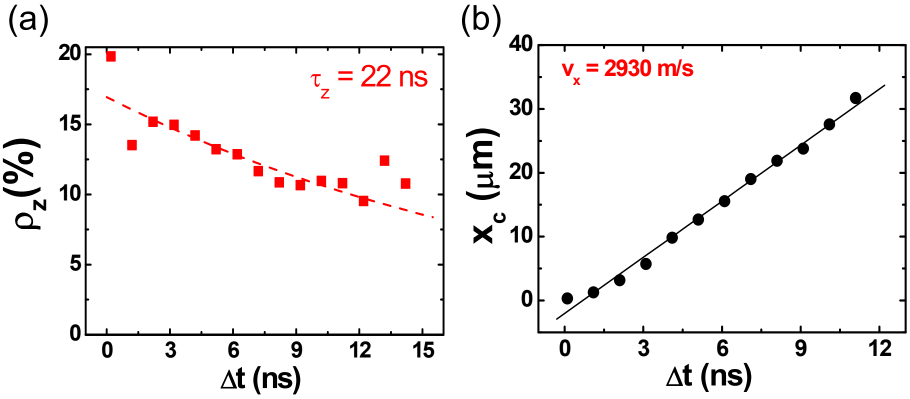

Figure 6.2: (a) Spin polarization decay as a function of time delay (Δt) for transport along the [001] direction. The dashed line is an exponential fit. (b) Mean position of the PL (x_c) emitted by the transported carriers as a function of Δt. The linear fit provides the spin transport velocity along the SAW propagation direction.

6.1.2 Spin relaxation along the $[1\bar{1}0]$ direction

Figure 6.3(a) summarizes the corresponding results for the spin polarization as a function of time obtained for transport along the $\hat{y} \parallel [1\bar{1}0]$ direction. The significant drop of the spin polarization ρ_z after Δt = 0 [which is also observed, but smaller in Fig. 6.2(a)] is attributed to an inefficient screening of the *e*-*hh* interaction close to the generation point G. There, the SAW piezoelectric field is screened due to the large number of carriers, which leads to fast spin relaxation via the Bir-Aronov-Pikus mechanism. Note that the experimental conditions are the same in Figs. 6.2 and 6.3 (i.e., T = 15 K and P_{rf} = 20 dBm). However, the carrier confinement by the piezoelectric potential of the Bleustein-Gulyaev wave propagating along the $[1\bar{1}0]$ direction is weaker than the one of the Rayleigh SAW along [001]. Therefore, the BAP mechanism at the generation spot is more effective for transport along the $[1\bar{1}0]$ direction. As observed in the results for different light excitation powers presented in Subsection 5.3.1, Fig. 6.3(a) confirms that during the long-range transport regime ρ_z decays with a much lower relaxation rate due to the absence of BAP relaxation. The polarization decays exponentially (dashed line) with a lifetime of (20 ± 2) ns. The spin propagation velocity is obtained from Fig. 6.3(b), where the linear fit to the mean packet position (y$_c$) as a function of Δt yields $v_y = (3180 \pm 100)$ m/s (the calculated value was 3310 m/s and the at room temperature $\lambda_{\mathrm{SAW}} f_{\mathrm{SAW}}$ = 3292 m/s). The corresponding spin transport distance associated with v_y is then $L_s = (64 \pm 6)$ μm.

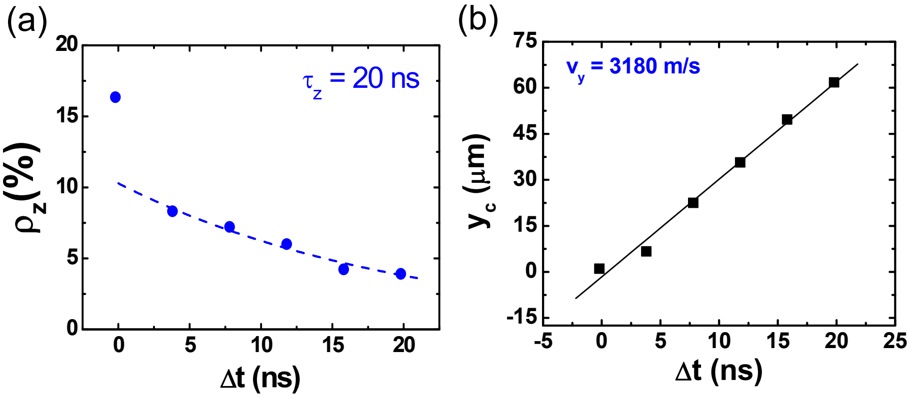

Figure 6.3: (a) Spin polarization decay as a function of time delay (Δt) relative to the excitation pulse for transport along the [1$\bar{1}$0] direction. The dashed line is an exponential fit. (b) Mean packet position (y$_c$) as a function of Δt, from which we obtain the spin transport velocity along this direction.

6.2 Spin transport anisotropy

The lifetimes of approximately 20 ns for the z-oriented spins obtained during acoustic transport in our GaAs (110) QW are comparable to the longest ones reported for GaAs (001) QWs. In the latter case, where the DP mechanism is the most effective one, the long spin lifetimes were achieved by exploiting motional narrowing induced by increasing of momentum scattering rates by doping [87, 88, 118] and by confining the spins in moving quantum dots [132]. The strikingly long spin lifetimes for the (110) QWs during acoustic transport also arise from the suppression of the DP mechanism for the z-oriented spins, which results from the QW crystal symmetry. We have also shown that the suppression of BAP relaxation and motional narrowing effects caused by spin scattering on the acoustic potential boundaries contribute to the enhancement of the spin lifetimes.

Until now, however, we have not performed a detailed study of the DP mechanism in our system. In this last section, we present additional evidence for the importance of this dephasing process. We demonstrate that the DP dephasing becomes "activated" when external magnetic fields are applied. In (110) QWs, when the spin vector is rotated away from the direction of the SO-field (the z-direction) it becomes extremely sensitive to carrier momentum fluctuations due to the dependence of the SO-field on electron momentum. Since momentum scattering occurs in a much shorter time scale than spin relaxation, the average spin vector of the ensemble is randomized very fast. Under these conditions, we show that the spin dynamics can be fully described in terms of the DP dephasing. The SIA effects induced by SAW are then shown to have minor contribution to the spin dephasing. The dependence of the SO-field due to DP mechanism on the carrier momentum direction will also be investigated by acoustic transport experiments along the [001] and [1$\bar{1}$0] directions under external magnetic fields. By taking into account the well-defined average momentum impinged on the carriers by the SAW, we show that the spin dephasing dynamics can be understood in terms of the SO-field dependence on carrier momentum.

6.2.1 Spin dephasing along the [001] direction

During transport along $\hat{x} \parallel [001]$, a magnetic field ($\mathbf{B}_{\text{ext}} \parallel \hat{y}$) perpendicular to the transport path was applied to induce coherent precession of the average spin vector in the x-z plane. The spin precession is reflected in the time (spatial) oscillations in ρ_z shown in Fig. 6.4. The triangles followed by the dashed line repeat the result for the spin polarization without external field, already shown in Fig. 6.2(a). The oscillations of ρ_z are strongly damped and decay within times much shorter than τ_z, vanishing for time delays longer than 10 ns.

The SIA contribution induced by the SAW strain and piezoelectric fields (as well as by asymmetries in the QW potential due to differences between the upper and lower interfaces) have minor effects on the spin dephasing. As we showed in chapter 3, the average values of SIA effective magnetic fields lie in the QW plane. These fields can, therefore, modify the resultant magnetic field which induces spin precession since they can add or subtract to the in-plane external applied field, depending on the relative orientation between both kind of fields. In the present case, however, this SIA contribution can be neglected based on the invariance of the spin dynamics under reversal of the applied field. This behavior is illustrated by the dots and circles in Fig. 6.4, which were measured under $B_{ext} = 17.6$ and -17.6 mT, respectively. We estimate that the SAW induced effective magnetic fields may have amplitude smaller than 1 mT and do not affect considerably the spin precession dynamics.

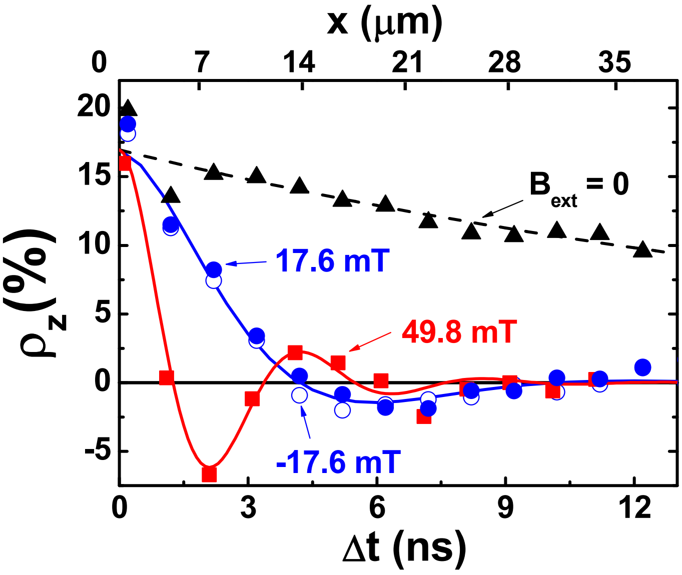

Figure 6.4: Spin polarization ρ_z during transport along $\hat{x}$ under different external magnetic fields B_{ext} applied along $\hat{y}$. The top horizontal axis shows the spatial coordinates ($x = v_x \Delta t$) corresponding to the delays Δt on the bottom axis. The dashed and solid lines are fits to exponential decay and to the spin dephasing model, respectively.

During acoustic transport, the carriers are confined along [001], but free to move along the SAW wave front direction $\hat{y}$ parallel to $[1\bar{1}0]$. The average carrier momentum along this direction is, therefore, equal to zero (i.e., $\langle k_y \rangle = 0$). According to equation (3.9), the average value of the DP internal magnetic field $\mathbf{B}_{\mathrm{int}}$ also vanishes. The dynamics of the spin packets moving along $\hat{x}$ becomes then similar to the one of static spin ensembles [45], where $\langle \mathbf{k} \rangle = 0$. Under external fields, the in-plane spin dynamics becomes strongly sensitive to the random thermal motion of the carriers along $\hat{y}$, which causes fluctuations on $\mathbf{B}_{\mathrm{int}}$ $[\langle B^2_{\mathrm{int}} \rangle \propto \langle k^2_y \rangle]$. The latter leads to the strongly dumped precession revealed by the data in Fig. 6.4. The solid lines in Fig. 6.4 were obtained by consistent fitting of the experimental data with equation (3.13) derived for the anisotropic spin dephasing model. Using the spin relaxation time $\tau_z = 22$ ns and the initial spin polarization $\rho_0 = 16.9\%$ (extracted from the exponential fit to the zero-field data), and $|g_e| = 0.36$, the fit yields $\tau_x = 1.2$ ns. The effective spin coherence time, determined by equation (3.16), is then $\tau_{\text{eff}} = 2.3$ ns.

The value of τ_x obtained from the fit allows us to estimate the momentum scattering time, as well as the electron mobility in our undoped QW. Using equation (3.17) and a spin-splitting constant $\gamma = 18$ eV$\mathring{A}^3$ (to be determined in the next subsection), we obtain $\tau_p \approx 6$ ps, at T = 15 K and $P_{\text{rf}} = 20$ dBm. As we showed in subsection 5.3.3, τ_p may change slightly with the acoustic power. Using $\mu = e\tau_p/m_0$, we estimate the electron mobility of our system $\mu \approx 15 \times 10^4$ cm^2/Vs. This value for the electron mobility is consistent with the high carrier transport efficiency in our experiments. In chapter 5, we demonstrated that the lowest acoustic power necessary to induce carrier transport was $P_{\text{rf}} = 8$ dBm. Therefore, the electron mobility has necessarily to be higher than $\mu_{min} = v_x/F_x \approx 3 \times 10^3$ cm^2/Vs, were $F_x \approx 1$ kV/cm for $P_{\text{rf}} = 8$ dBm.

The large difference between τ_x and τ_z reflects an intrinsic property related to the bulk inversion asymmetry of the GaAs matrix, which makes the lifetime of z-oriented spins very sensitive to in-plane magnetic fields. Even slow rotations of the spin vector away from z caused by weak fields create in-plane spin components which are extremely sensitive to fluctuations of the Dresselhaus field $\mathbf{B}_{\text{int}} \parallel z$. Note that the ratio $\tau_z/\tau_x \approx 18$ obtained in our experiments is much larger than the one reported for the local PL measurements in Ref. [45], although values for τ_x are similar in both cases. The difference is attributed to longer lifetimes τ_z, which arise from the suppression of the BAP relaxation and from the lateral carrier confinement during acoustic transport discussed in chapter 5.

Hanle Effect

Hanle effect experiments provide an alternative way to access the in-plane spin relaxation time τ_x using CW experiments, which up to now has been performed only by TR techniques [36, 45, 101, 121].

We have carried out the CW experiments using the same configuration of the TR ones, i.e., with the in-plane magnetic field $\mathbf{B}_{\text{ext}}$ applied along the $\hat{y} \parallel [1\bar{1}0]$ direction, while the carriers propagate along $\hat{x}$. The applied acoustic power was $P_{\mathrm{rf}} = 16$ dBm and the temperature T = 11 K. The spatial profiles of ρ_z for different external fields are displayed in Fig. 6.5(a). A significantly faster spin depolarization as $\mathrm{B}_{\mathrm{ext}}$ increases is again verified.

Figure 6.5(b) summarizes the dependence of the spin polarization on $\mathrm{B}_{\mathrm{ext}}$. The dots display the spatially averaged spin polarization $\bar{\rho}_z$ obtained by integrating the spin density along the transport direction. The solid line is a fit of the data with equation (3.19) for the corresponding average degree of spin polarization. We use the parameters previously determined from the CW experiments in Chapter 5, i.e., $\gamma_z = \tau_z^{-1} = v_x/L_s = 0.045\ ns^{-1}$, and $\gamma_{\mathrm{r}} = v_x/L = 0.0625\ ns^{-1}$ (with $L = 47\ \mu$m, see section 5.3.3). Taking again $|g_e| = 0.36$, the best agreement is found for an in-plane spin relaxation rate of $\gamma_x = 1$ ns^{-1}. The effective spin lifetime is then $\tau_{\mathrm{eff}} = 1.9$ ns.

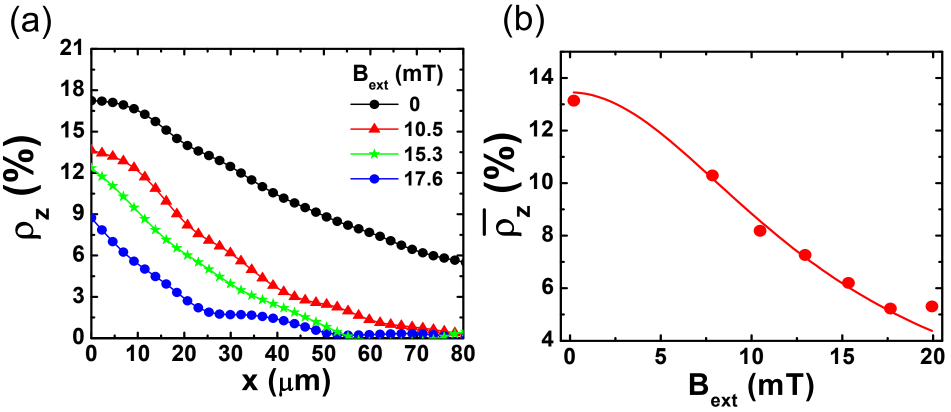

Figure 6.5: (a) Spatial dependence of the spin polarization decay under different external magnetic fields obtained in CW measurements. (b) Average value of $\bar{\rho_z}$ as a function of the applied field $\mathrm{B}_{\mathrm{ext}}$.

The expression for the Hanle effect derived in subsection 3.4.1 reproduces reasonably well the behavior of the experimental data. Furthermore, agreement is also found between the values obtained for γ_x from the CW and TR analysis. The values for τ_x obtained under acoustic transport also agree with the ones reported in Ref. [45], which were obtained in TR experiments at similar temperatures using an undoped (110) QW with similar thickness.

6.2.2 Spin dephasing along the $[1\bar{1}0]$ direction

We now analyze the spin dynamics under external magnetic fields during transport along the $[1\bar{1}0]$ direction. The TR measurements were performed under the same conditions as the ones along [001], i.e., $P_{\text{rf}} = 20$ dBm and T $= 15$ K. The external magnetic field was parallel to the transport direction $\mathbf{B}_{\text{ext}} \parallel \hat{y}$.

Figure 6.6 displays the time dependence of the spin polarization ρ_z measured under $\mathrm{B}_{\text{ext}} = 0$ (triangles) and under an external magnetic field of 17.6 mT (circles). The overall level of ρ_z reduces, but the decay time is not significantly affected by the external field. In contrast to the previous situation, motion along $\hat{y}$ induces a SO-field with a finite average value $\langle \mathbf{B}_{\text{int}} \rangle \neq 0$ [cf. equation (3.9)]. The spins are then forced to precess around a resultant field $\mathbf{B}_{\text{R}} = \mathbf{B}_{\text{ext}} + \langle \mathbf{B}_{\text{int}} \rangle$, which has a non-zero component along $\hat{z}$ [cf. inset in Fig. 6.6]. The solid line in Fig. 6.6 is a fit for $\mathrm{B}_{\text{ext}} = 17.6$ mT to the numerical solution of equation (3.20) (without the second term on the right), which yields the time dependence of the spin polarization degree $[\rho_z(\Omega_{\text{ext}}, t)]$ along the z-direction. Using $\tau_z = 20$ ns (determined from the $\mathrm{B}_{\text{ext}} = 0$ exponential decay) and assuming $\tau_x = \gamma_x^{-1} = 1.2$ ns, best agreement is found for $\tau_l = 18 \pm 2$ ns and $\langle B_{\text{int}} \rangle = (20 \pm 3)$ mT. Within the experimental accuracy, the longitudinal spin polarization lifetime τ_l [equation (3.21)] essentially coincides with the value of τ_z for the spin lifetime during transport in the absence of applied fields. The numerical solution for $\rho_z(\Omega_{\text{ext}}, t)$ shows two decay regimes, which can be identified in Fig. 6.6. The fast decay (for $\Delta t < 5$ ns) occurs due to the rapid loss of spin polarization in the direction transverse to the resultant magnetic field (indicated by s^t in the inset of Fig. 6.6). The long decay ($\Delta t > 5$ ns), describes the slow loss of the longitudinal spin polarization s^ℓ along the resultant field direction. While the time scale of s^t is of a few nanoseconds, similar to τ_{eff} for transport along $\hat{x}$, the decay of the longitudinal component s^ℓ is determined by τ_l.

The SO-splitting constant of GaAs can then be determined from the value of $\langle B_{\text{int}} \rangle$. Using equation (3.9) and assuming a barrier penetration depth of 1 nm at each QW interface, we obtain $\gamma = (18 \pm 3)$ eV$\mathring{A}^3$. This value is close to the one obtained by spin transport by mobile potential dots [132] and is in agreement with theoretical calculations [33, 46].

A comparison between the spin dephasing during acoustic transport under external fields for the [001] and $[1\bar{1}0]$ directions reveals significantly dis-

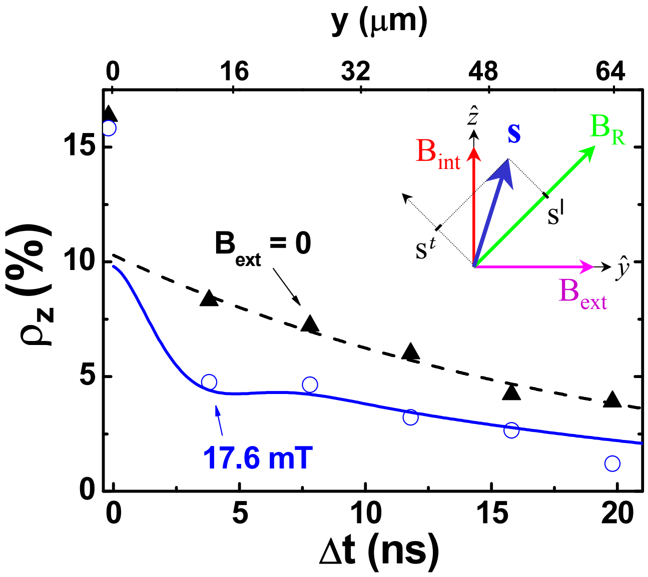

Figure 6.6: Spin polarization ρ_z during transport along $\hat{y} \parallel [1\bar{1}0]$ under external magnetic field. The dashed and solid lines are fittings to an exponential decay and to the spin dephasing model, respectively. The inset shows a vector scheme illustrating the longitudinal (s^ℓ) and transverse (s^t) spin polarization components relative to the direction of the resultant field $\mathbf{B}_R$.

tinct spin dynamics. While in the former case the average z-orientation of the spins is quickly lost, in the latter it is maintained for longer times due the non-vanishing average SO-field. A further confirmation of this transport anisotropy is provided by the dependence of $\rho_z(\Omega_{ext}, t)$ on B_{ext} measured for both transport directions at fixed time delays (or, equivalently, fixed transport distances) shown in Fig. 6.7. The strong reduction of ρ_z with increasing B_{ext} for $\Delta t = 12.2$ ns, which is observed for transport along $\hat{x}$ (circles), is again well-reproduced by the dephasing model described by equation (3.13) (dashed line) using the parameters determined in the previous section. Along $\hat{y}$, in contrast, the polarization shows a much weaker field dependence, as shown by the data for $\Delta t = 2.4$ ns (dots) and 4.8 ns (squares). This behavior is reasonably well reproduced by the solid lines superposed on the data, which were obtained by the substitution of the previously determined values of $\langle B_{int} \rangle$ and τ_l in equation (3.21) for the z-component of the longitudinal degree of spin polarization $\rho_z^\ell(\Omega_{ext}, t)$.

We have demonstrated in the previous paragraphs that the results pre-

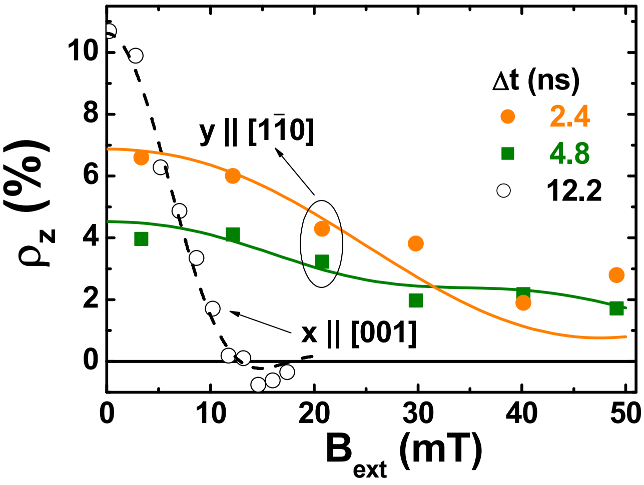

Figure 6.7: Magnetic field dependence of ρ_z measured at fixed delays Δt during transport along $\hat{x}$ (circles) and $\hat{y}$ (dots and squares). The dashed and solid lines are fittings to the dephasing models for motion along $\hat{x}$ and $\hat{y}$, respectively.

sented in Figs. 6.4, 6.6, and 6.7 can be understood solely based on the predictions for spin dephasing due to the D'yakonov-Perel' mechanism described in chapter 3. The DP mechanism provides the main contribution to the spin dephasing under external magnetic fields. Spin dephasing during precession takes place in a time scale of 1 - 2 ns, which is one order of magnitude shorter than the values of 20 ns, obtained in the absence of a field. Furthermore, the well-defined average carrier momentum determined by the SAW propagation velocity allowed us to address the **k**-momentum anisotropy of the Dresselhaus term for (110) III-V QWs, which is predicted by equation (3.8).

Chapter 7

Conclusions

In this work, we have investigated spin transport by surface acoustic waves in symmetric and undoped (110) GaAs QWs.

Spin ensembles were optically generated using circularly polarized light. The type-II spatial separation of electrons and holes induced by the SAW piezoelectric field enabled the successful demonstration of charge transport by the propagating wave. The spin dynamics during acoustic transport was analyzed by polarization-resolved PL measurements. We demonstrated long-range spin transport by the acoustic fields with spin transport lengths approaching 70 μm, corresponding to spin lifetimes longer than 20 ns. The spin dynamics was demonstrated to be independent of temperature up to liquid nitrogen temperatures. The long spin lifetimes and the invariance of the spin transport properties with temperature and light excitation power were attributed to the suppression of the D'yakonov-Perel' (related to the crystal symmetry of the system) and the Bir-Aronov-Pikus (induced by the spatial separation of electron and holes) spin relaxation mechanisms. An enhancement of the spin lifetimes with the applied acoustic transport was demonstrated and attributed to a progressive lateral confinement of carriers into narrow stripes with lateral widths smaller than the SAW wavelength. The suppression of spin relaxation by carrier confinement was understood in terms of motional narrowing effects associated with the spin scattering at the lateral confinement potential boundaries.

These achievements were accomplished due to the realization of a cooperative and well-succeeded group strategy. The optimization of the sample structural quality was decisive. The growth of (110) GaAs QWs at relatively lower temperatures (≈ 490°C) and the addition of annealing steps during growth were shown to be very important for the obtention of high-quality samples. The IDT design, which is required for the generation of high power/focusing acoustic beams, was demonstrated to produce very effective and narrow transport channels. The deposition of a piezoelectric ZnO layer on top of the III-V multilayer structure prior to the IDT manufacturing was also plays a crucial role for the efficiency of the carrier and spin transport, as compared to the case where no deposition was performed. In this way, very efficient carrier and spin transport, stable against small potential fluctuations along the SAW channel could be achieved. The high piezoelectric fields generated with the addition of the piezoelectric layer allowed for the strong carrier confinement required for the enhancement the spin lifetimes.

Spin manipulation using external magnetic fields was also studied. Performing spin transport along the [001] and $[1\bar{1}0]$ in-plane directions, the spin dephasing dynamics under these conditions could be entirely described in terms of the D'yakonov-Perel spin dephasing mechanism. The well-defined average velocity impinged by the acoustic wave on the carriers along the two directions allowed for the demonstration of a spin transport anisotropy in the QW plane, which occurs due to the dependence of the spin-orbit coupling on momentum direction. While along the [001] direction spins were shown to live for a few nanoseconds under external fields, the z-component of the spin vector was preserved during transport along the $[1\bar{1}0]$ direction for times one order of magnitude longer. The latter is due to the non-zero average value of the spin-orbit internal magnetic field, exactly as expected from the D'yakonov-Perel' mechanism. The comparison of the experimental data with the theoretical models yields a spin-orbit coupling constant for GaAs of $\gamma = (18 \pm 3)$ eV$\AA^3$.

The results demonstrated here open many possibilities for further studies on spin transport in (110) III-V structures. Increase of the material g-factor, for example, is interesting for spintronics applications. The optimized growth of (Al,Ga)As-based structures can possibly open the way for the obtention of high-quality (In,Al,Ga)As multilayers, which are expected to have higher g-factors due to the addition of In. Spin manipulation using the SAW strain and piezoelectric fields represent another promising application. Lateral confinement effects can be explored to achieve longer spin lifetimes by using acoustic beams with smaller wavelengths or by performing surface treatments to restrict the carrier diffusion along the SAW wavefront during transport. A more detailed investigation of the temperature dependence of the spin relaxation, aiming at higher temperature transport, is also needed. A promising approach, which is in development in our group, is the use of (110) optical microcavity structures to enhance the interaction of the incoming light with the QW, thus enabling PL measurements at high temperatures.

Bibliography

[1] T. Adachi, Y. Ohno, F. Matsukura, and H. Ohno. Spin relaxation in n-modulation doped GaAs/AlGaAs(110) quantum wells. *Physica E*, 10:36, 2001.

[2] L. T. P. Allen, E. R. Weber, J. Washburn, and Y. C. Pao. Device quality growth and characterization of (110) GaAs grown by molecular beam epitaxy. *Appl. Phys. Lett.*, 51:670, 1987.

[3] L. T. P. Allen, E. R. Weber, J. Washburn, Y. C. Pao, and A. G. Elliot. Characterization of surface faceting on (110)GaAs/GaAs grown by molecular beam epitaxy. *J. Crys. Growth*, 87:193, 1988.

[4] F. Alsina, P. V. Santos, H.-P. Schönherr, W. Seidel, R. Nötzel, and K. H. Ploog. Surface-acoustic-wave-induced carrier transport in quantum wires. *Phys. Rev. B*, 65:165330, 2002.

[5] F. Alsina, J. A. H. Stotz, R. Hey, and P. V. Santos. Radiative recombination during acoustically induced transport in GaAs quantum wells. *J. Vac. Science Technol. B*, 24:2029, 2006.

[6] T. Aono and S. Tamura. Surface and pseudosurface acoustic waves in superlattices. *Phys. Rev. B*, 58:4838, 1998.

[7] I. Appelbaum, B. Huang, , and D. J. Monsma. Electronic measurement and control of spin transport in silicon. *Nature*, 447:295, 2007.

[8] B. A. Auld. *Acoustic Fields and Waves in Solids.* Robert E. Krieger Publishing Company, Inc, Malabar, Florida, 1990.

[9] D. D. Awschalom. Manipulating and storing spin coherence in semiconductors. *Physica E*, 10:1, 2001.

[10] D. D. Awschalom and M. E. Flatté. Challenges for semiconductor spintronics. *Nature Phys.*, 3:153, 2007.

[11] D. D. Awschalom, D. Loss, and N. Samarth. *Semiconductor Spintronics and Quantum Computation.* Springer, Berlin, 2002.

[12] M. N. Baibich, J. M. Broto, A. Fert, F Nguyen Van Dau, F. Petroff, P. Eitenne, G. Creuzet, A. Friederich, and J. Chazelas. Giant magnetoresistance of (001)Fe/(001)Cr magnetic superlattices. *Phys. Rev. Lett.*, 61:2472, 1988.

[13] J. M. Ballingall and C. E. C. Wood. Crystal orientation dependence of silicon autocompensation in molecular beam epitaxial gallium arsenide. *Appl. Phys. Lett.*, 41:947, 1982.

[14] C. H. W. Barnes, J. M. Shilton, and A. M. Robinson. Quantum computation using electrons trapped by surface acoustic waves. *Phys. Rev. B*, 62:8410, 2000.

[15] G. Bastard, E. E . Mendez, L. L. Chang, and L. Esaki. Variational calculations of a quantum well in an electric field. *Phys. Rev. B*, 28: 3241, 1983.

[16] M. Beck. *Electron spin relaxation,transport and strain-induced precession in n-GaAs.* PhD thesis, Universität Erlangen-Nürnberg, 2004.

[17] M. Beck, C. Metzner, S. Malzer, and G. H. Döhler. Spin lifetimes and strain-controlled spin precession of drifting electrons in GaAs. *Europhys. Lett.*, 75:597, 2006.

[18] C. H. Bennett. Quantum cryptography: Uncertainty in the service of privacy. *Science*, 257:752, 2002.

[19] G. Binasch, P. Grünberg, F. Saurenbach, and W. Zinn. Enhanced magnetoresistance in layered magnetic structures with antiferromagnetic interlayer exchange. *Phys. Rev. B*, 38:4828, 1988.

[20] G. L. Bir, A. G. Aronov, and G. E. Pikus. Spin relaxation of electrons due to scattering by holes. *Sov. Phys. JETP*, 42:705, 1976.

[21] J. L. Bleustein. A new surface wave in piezoelectric materials. *Appl. Phys. Lett.*, 13:412, 1968.

[22] W. Braun, A. Trampert, L. Däweritz, and K. H. Ploog. Nonuniform segregation of Ga at AlAs/GaAs heterointerfaces. *Phys. Rev. B*, 55: 1689, 1997.

[23] V. M. Bright and W. D. Hunt. Bleustein-Gulyaev waves in gallium arsenide and other piezoelectric cubic crystals. *J. Appl. Phys.*, 66: 1556, 1989.

[24] V. M. Bright, Y. Kim, and W. D. Hunt. Study of surface acoustic waves on the (110) plane of gallium arsenide. *J. Appl. Phys.*, 71:597, 1992.

[25] Yu. A. Bychkov and E. I. Rashba. Oscillatory effects and the magnetic-susceptibility of carriers in inversion layers. *J. Phys. C*, 17:6039, 1984.

[26] Yu. A. Bychkov and E. I. Rashba. Properties of 2D electron gas with lifted spectral degeneray. *JETP Lett.*, 39:78, 1984.

[27] M. Cardona, N. E. Christensen, and G. Fasol. Relativistic band structure and spin-orbit splitting of zinc-blende-type semiconductors. *Phys. Rev. B*, 38:1806, 1988.

[28] C. A. Chang. Interface morphology studies of (110) and (111) Ge-GaAs grown by molecular beam epitaxy. *Appl. Phys.Lett.*, 40:1037, 1982.

[29] Cheng-Hung Chang, A. G. Mal'shukov, and K. A. Chao. Spin relaxation dynamics of quasiclassical electrons in ballistic quantum dots with strong spin-orbit coupling. *Phys. Rev. B*, 70:245309, 2004.

[30] Y.-H. Cho, F. Fedler, R. J. Hauenstein, G. H. Park, J. J. Song, S. Keller, U. K. Mishra, and S. P. DenBaars. High resolution x-ray analysis of pseudomorphic InGaN/GaN multiple quantum wells: influence of Si doping concentration. *J. Appl. Phys.*, 85:3006, 1999.

[31] L. A. Choldren. Zinc-oxide-on-silicon acoustically scanned imager with positive sensitivity and storage capabilities. *Appl. Phys. Lett.*, 27:6, 1975.

[32] N. E. Christensen. Electronic structure of GaAs under strain. *Phys. Rev. B*, 30:5753, 1984.

[33] N. E. Christensen and M. Cardona. Splitting of the conduction bands of GaAs for k along [110]. *Solid State Comm.*, 51:491, 1984.

[34] M. G. Cohen. Optical study of ultrasonic diffraction and focusing in anisotropic media. *J. Appl. Phys.*, 38:3821, 1967.

[35] O. D. D. Couto, Jr., F. Iikawa, J. A. H. Stotz, R. Hey, and P. V. Santos. Coherent spin transport by acoustic fields in GaAs quantum wells. *Phys. Status Solidi c*, 3:4307, 2006.

[36] O. D. D. Couto, Jr., F . Iikawa, J. Rudolph, R. Hey, and P. V. Santos. Anisotropic spin transport in (110) GaAs quantum wells. *Phys. Rev. Lett.*, 98:036603, 2007.

[37] O. D. D. Couto, Jr., R. Hey, and P. V. Santos. Spin dynamics in (110) GaAs quantum wells under surface acoustic waves. *Phys. Rev. B*, 78: 153305, 2008.

[38] S. A. Crooker, M. Furis, X. Lou, C. Adelmann, D. L. Smith, C. J. Palmström, and P. A. Crowell. Imaging spin transport in lateral ferromagnet/semiconductor structures. *Science*, 309:2191, 2005.

[39] T. C. Damen, L. Viña, and J. Shah. Subpicosecond spin relaxation dynamics of exciton and free-carriers in GaAs quantum wells. *Phys. Rev. Lett.*, 67:3432, 1991.

[40] S. Datta and B. Das. Electronic analog of the electro-optic modulator. *Appl. Phys. Lett.*, 56:665, 1990.

[41] E. A. de Andrada e Silva. Spin-orbit splitting of the electrons states in semiconductor asymmetric quantum wells. *Phys. Rev. B*, 55:16293, 1997.

[42] M. M. de Lima, Jr. and P. V. Santos. Modulation of photonic structures by surface acoustic waves. *Rep. Prog. Phys.*, 68:1639, 2005.

[43] M. M. de Lima, Jr., F. Alsina, W. Seidel, and P. V. Santos. Focusing of surface-acoustic-wave fields on (100) GaAs surfaces. *J. Appl. Phys.*, 94:7848, 2003.

[44] D. P. DiVincenzo and D. Loss. Quantum computers and quantum coherence. *J. Magn. Magn. Mater.*, 200:202, 1999.

[45] S. Döhrmann, D. Haegele, J. Rudolph, D. Schuh, M. Bichler, and M. Oestreich. Anomalous spin dephasing in (110) GaAs quantum wells: anisotropy and intersubband effects. *Phys. Rev. Lett.*, 93:147405, 2004.

[46] G. Dresselhaus. Spin-orbit coupling effects in zinc-blende structures. *Phys. Rev.*, 55:580, 1955.

[47] M. I. D'yakonov and V. Y. Yu. Kachorovskii. Spin relaxation of two-dimensional electrons in noncentrosymmetric semiconductors. *Sov. Phys. Semicond.*, 20:110, 1986.

[48] M. I. D'yakonov and V. I. Perel'. Spin relaxation of conduction electrons in noncentrosymmetric semiconductors. *Sov. Phys. Solid State*, 13:3023, 1972.

[49] M. I. D'yakonov and V. I. Perel'. Spin orientation of electrons associated with the interband absorption of light in semiconductors. *Sov. Phys. JETP*, 33:1053, 1971.

[50] M. I. D'yakonov and V. I. Perel'. Optical orientation in a system of electrons and lattice nuclei in semiconductors. Theory. *SPJETP*, 38: 177, 1974.

[51] M. I. D'yakonov, V. A. Marushchak, V. I. Perel', and A. N. Titkov. The effects of strain on the spin relaxation of conduction electrons in III-V semiconductors. *Sov. Phys. JETP*, 63:665, 1986.

[52] J. K. Elliot, R. L. Gunshor, R. F. Pierret, and K. L. Davis. Zinc oxide-silicon monolithic acoustic surface wave optical image scanner. *Appl. Phys. Lett.*, 27:179, 1975.

[53] R. J. Elliott. Theory of the effect of spin orbit coupling on magnetic resonance in some semiconductors. *Phys. Rev.*, 96:266, 1954.

[54] R. Eppenga and M. F. H. Shuurmans. Effect of bulk inversion asymmetry on [001], [110], and [111] GaAs/AlAs quantum wells. *Phys. Rev. B*, 37:10923, 1988.

[55] P. N. Fawcett, J. N. Neave, J. Zhang, and B. A. Joyce. Study of the epitaxial growth of GaAs(110) films by molecular beam epitaxy. *J. Vac. Sci. Technol. A*, 12:1201, 1994.

[56] R. Fiederling, M. Keim, G. Reuscher, W. Ossau, G. Schmidt, A. Waag, and L. W. Molenkamp. Injection and detection of a spin-polarized current in a light-emitting diode. *Nature*, 402:787, 1999.

[57] G. Fishman and G. Lampel. Spin relaxation of photoelectrons in *p*-type gallium arsenide. *Phys. Rev. B*, 16:820, 1977.

[58] C. M. Flannery, E. Chilla, S. Semenov, and H.-J. Fröhlich. Elastic properties of GaAs obtained by inversion of laser-generated surface acoustic wave measurements. In *Proceedings of the 1999 IEEE Ultrasonics Symposium*, page 501, New York, 1999. IEEE.

[59] M. Furis, D. L. Smith, S. Kos, E. S. Garlid, K. S. M. Reddy, C. J. Palmström, P. A. Crowell, and S. A. Crooker. Local Hanle-effect studies of spin drift and diffusion in *n*:GaAs epilayers and spin-transport devices. *New J. Phys.*, 9:347, 2007.

[60] S. Furuta, C. H. W. Barnes, and C. J. L. Doran. Single-qubit gates and measurements in the surface acoustic wave quantum computer. *Phys. Rev. B*, 70:205320, 2004.

[61] T. Gaebel, M. Domhan, I. Popa, C. Wittmann, P. Neumann, F. Jelezko, J. R. Rabeau, N. Stavrias, A. D. Greentree, S. Prawer, J. Meijer, J. Twamley, P. R. Hemmer, and J. Wrachtrup. Room-temperature coherent coupling of single spins in diamond. *Nature Phys.*, 2:408, 2006.

[62] J. G. E. Gardeniers, Z. M. Rittersma, , and G. J. Burger. Preferred orientation and piezoelectricity in sputtered zno films. *J. Appl. Phys.*, 83:7844, 1998.

[63] D. Gershoni, I. Brener, G. A. Baraff, S. N. G. Chu, L. N. Pfeiffer, and K. West. Anisotropic optical properties of (110)-oriented quantum wells. *Phys. Rev. B*, 44:1930, 1991.

[64] G. Giavaras, J. H. Jefferson, A. Ramsak, T. P. Spiller, and C. J. Lambert. Quantum entanglement generation with surface acoustic waves. *Phys. Rev. B*, 74:195341, 2005.

[65] Yu V. Gulyaev. *JETP Lett.*, 9:37, 1969.

[66] K. C. Hall, K. Gündogdu, E. Altunkaya, W. H. Lau, M. E. Flatté, T. F. Boggess, J. J. Zinck, W. B. Barvosa-Carter, and S. L. Skeith. Spin relaxation in (110) and (001) InAs/GaSb superlattices. *Phys. Rev. B*, 68:115311, 2003.

[67] K. C. Hall, W. H. Lay, K. Gündogdu, and M. E. Flatté. Nonmagnetic semiconductor spin transistor. *Appl. Phys. Lett.*, 83:2937, 2003.

[68] K. C. Hall, K. Gündogdu, J. L. Hicks, A. N. Kocbay, M. E. Flatté, T. F. Boggess, K. Holabird, A. Hunter, D. H. Chow, and J. J. Zinck. Room-temperature electric field controlled spin dynamics in (110) InAs quantum wells. *Appl. Phys. Lett.*, 86:202114, 2005.

[69] J. M. Hammer, D. J. Channin, M. T. Duffy, and J. P. Wittke. Low-loss epitaxial zno optical waveguides. *Appl. Phys. Lett.*, 21:358, 1972.

[70] R. Hanson, L. P. Kouwenhoven, J. R. Petta, S. Tarucha, and L. M. K. Vandersypen. Spins in few-electron quantum dots. *Rev. Mod. Phys.*, 79:1217, 2007.

[71] W. A. Harrison, E. A. Kraut, J. R. Waldrop, and R. W. Grant. Polar heterojunction interfaces. *Phys. Rev. B*, 18:4402, 1978.

[72] R. Hey, A. Trampert, and P. V. Santos. (In,Ga)As/(Al,Ga)As quantum wells on GaAs(110). *Phys. Status Solidi c*, 3:651–654, 2006.

[73] R. Hey, A. Trampert, U. Jahn, O. D. D. Couto, Jr., and P. V. Santos. Growth of (In,Ga)As/(Al,Ga)As quantum wells on GaAs(110) by MBE. *J. Cryst. Growth*, 301-302:158, 2007.

[74] A.W. Holleitner, V. Sih, R. C. Myers, A. C. Gossard, and D. D. Awschalom. Suppression of spin relaxation in submicron InGaAs wires. *Phys. Rev. Lett.*, 97:036805, 2006.

[75] Y. Horikoshi, M. Kawashima, and H. Yamaguchi. Low -temperature growth of GaAs and AlAs-GaAs quantum-well layers by modified molecular beam epitaxy. *Jap. J. Appl. Phys.*, 25:L868, 1988.

[76] M. J. Hoskins, H. Morkoç, and B. J. Hunsinger. Charge transport by surface acoustic waves in GaAs. *Appl. Phys. Lett.*, 41:332, 1982.

[77] X. Hu, R. de Souza, and S. Das Sarma. Decoherence and dephasing in spin-based solid state quantum computers. *cond-mat/0108339*, 2007.

[78] B. Huang, D. J. Monsma, and I. Appelbaum. Spin lifetime in silicon in the presence of parasitic electronic effects. *J. Appl. Phys.*, 102:013901, 2007.

[79] B. Huang, D. J. Monsma, and I. Appelbaum. Experimental realization of a silicon spin field-effect transistor. *Appl. Phys. Lett.*, 91:072501, 2007.

[80] K. A . Ingebrigtsen. Surface waves in piezoelectrics. *J. Appl. Phys.*, 40:2681, 1967.

[81] A. L. Ivanov and P. B. Littlewood. Acoustically induced Stark effect for excitons in intrinsic semiconductors. *Phys. Rev. Lett.*, 87:136403, 2001.

[82] O. Z. Karimov, G. H. John, R. T. Harley, W. H. Lau, M. E. Flatte, and M. Henini. High temperature gate control of quantum well spin memory. *Phys. Rev. Lett.*, 91:246601, 2003.

[83] M. Kataoka, R. J. Schneble, A. L. Thorn, C. H.W. Barnes, C. J. B. Ford, D. Anderson, G. A. C. Jones, I. Farrer, D. A. Ritchie, and M. Pepper. Single-electron population and depopulation of an isolated quantum dot using a surface-acoustic-wave pulse. *Phys. Rev. Lett.*, 98: 046801, 2007.

[84] Y. Kato, R. C. Myers, A. C. Gossard, and D. D. Awschalom. Coherent spin manipulation without magnetic fields in strained semiconductors. *Nature*, 427:50, 2004.

[85] Y. K. Kato, R. C. Myers, A. C. Gossard, and D. D. Awschalom. Observation of the spin Hall effect in semiconductors. *Science*, 306:1910, 2004.

[86] J. M. Kikkawa and D. D. Awschalom. Lateral drag of spin coherence in gallium arsenide. *Nature*, 397:139, 1999.

[87] J. M. Kikkawa and D. D. Awschalom. Resonant spin amplification in *n*-type GaAs. *Phys. Rev. Lett.*, 80:4313, 1998.

[88] J. M. Kikkawa, I. P. Smorchkova, N. Samarth, and D. D. Awschalom. Room-temperature spin memory in two-dimensional elesctron gases. *Science*, 277:1284, 1997.

[89] A. A. Kiselev and K. W. Kim. Progressive suppression of spin relaxation in two-dimensional channels of finite width. *Phys. Rev. B*, 61: 13115, 2000.

[90] C. Kittel. *Quantum Theory of Solids.* Wiley, New York, 1963.

[91] H. Kroemer, K. J. Polasco, and S. C. Wright. Polar heterojunction interfaces. *Appl. Phys. Lett.*, 36:763, 1980.

[92] L. S. Liu, W. X. Wang, Z. H. Li, B. L. Liu, H. M. Zhao, J. Wang, H. C. Gao, Z. W. Jiang, S. Liu, H. Chen, and J. M. Zhou. Influence of interface interruption on spin relaxation in GaAs (110) quantum wells. *J. Cryst. Growth*, 301:93, 2007.

[93] M. Lopez, Ikei T, Y. Takano, K. Pak, and Yonezu H. Initial growth mechanism of GaAs on Si(110). *Jpn. J. Appl. Phys.*, 29:551, 1990.

[94] M. Lopez, Y. Takano, K. Pak, and Yonezu H. Realization of low facet density and the growth mechanism of GaAs on GaAs(110) by migration-enhanced epitaxy. *Appl. Phys. Lett.*, 58:580, 1991.

[95] M. Z. Maialle, E. A. de Andrada e Silva, and L. J. Sham. Exciton spin dynamics in quantum wells. *Phys. Rev. B*, 47:15776, 1993.

[96] A. Malinowski, R. S. Britton, T. Grevatt, R. T. Harley, D. A. Ritchie, and M. Y. Simmons. Spin relaxation in GaAs/$\mathrm{Al}_x\mathrm{Ga}_{1-x}\mathrm{As}$ quantum wells. *Phys. Rev. B*, 62:13034, 2001.

[97] A. G. Mal'shukov and K. A. Chao. Waveguide diffusion modes and slowdown of D'yakonov-P'erel spin relaxation in narrow two-dimensional semiconductor channels. *Phys. Rev. B*, 61:2413, 2007.

[98] V. A. Marushchak, M. N. Stepanova, and A. N. Titkov. Spin relaxation of conduction electrons in moderately doped gallium arsenide crystals. *Sov. Phys. Solid State*, 25:2035, 1983.

[99] F. Meier and B. P. Zakharchenya. *Optical orientation.* North-Holland, Amsterdam, 1984.

[100] D. A . Miller, D. S. Chemla, T. C. Damen, A. C. Gossard, W. Wiegmann, T. H. Wood, and C. A. Burrus. Electric field dependence of optical absorption near the band gap of quantum-well strucutures. *Phys. Rev. B*, 32:1043, 1985.

[101] K. Morita, H. Sanada, S. Matsuzaka, C. Y. Hu, Y. Ohno, and H. Ohno. Strong anisotropic spin dynamics in narrow n-InGaAs/AlGaAs (110) quantum wells. *Appl. Phys. Lett.*, 87:171905, 2005.

[102] L. Munõz, E. Pérez, L. Viña, and K. Ploog. Spin relaxation in intrinsic GaAs quantum wells: Influence of excitonic localization. *Phys. Rev. B*, 51:4247, 1995.

[103] J.-H. Noh, S. Hasegawa, T. Suzuki, T. Arakawa, K. Tada, and H. Asahi. Migration-enhanced epitaxy (MEE) growth of five-layer asymmetric coupled quantum well (FACQW) and its cross-sectional STM observation. *Physica E*, 23:482, 2004.

[104] H. Ohno, D. K. Young, B. Beschoten, F. Matsukura, H. Ohno, and D. D. Awschalom. Electrical spin injection in a ferromagnetic semiconductor heterostructure. *Nature*, 402:790, 1999.

[105] Y. Ohno, R. Terauchi, T. Adachi, F. Matsukura, and H. Ohno. Spin relaxation in GaAs (110) quantum wells. *Phys. Rev. Lett.*, 83:4196, 1999.

[106] A. W. Overhauser. Paramagnetic relaxation in metals. *Phys.Rev.*, 89: 689, 1953.

[107] I. Petrov, V. Orlinov, and A. Misiuk. Highly oriented ZnO films obtained by d.c. reactive sputterring of a zinc target. *Thin Solid Films*, 120:55–67, 1994.

[108] S. Pfalz, R. Winkler, T. Nowitzki, D. Reuter, D. Wieck, D. Hägele, and M. Oestreich. Optical orientation of electron spins in GaAs quantum wells. *Phys. Rev. B*, 71:165305, 2005.

[109] G. E. Pikus, V. A. Marushchak, and A. N. Titkov. Spin splitting of energy bands and spin relaxation of carriers in cubic III-V crystals (review). *Sov. Phys. Semicond.*, 22:115, 1988.

[110] E. I. Rashba. Properties of semiconductors with an extremum loop 1. cyclotron and combinational resonance in a magnetic field perpendicular to the plane of the loop. *Fiz. Tverd. Tela*, 2:1109, 1960.

[111] L. Rayleigh. On waves propagated along the plane surface of an elastic solid. *Proc. London Math. Soc.*, 17:4, 1885.

[112] H. Riechert, S. F. Alvarado, A. N. Titkov, and V. I. Safarov. Precession of the spin polarization of photoexcited conduction electrons in the band-bending region of GaAs (110). *Phys. Rev. Lett.*, 52:2297, 1984.

[113] C. Rocke, S. Zimmermann, A. Wixforth, J. P. Kotthaus, G. Böhm, and G. Weimann. Acoustically driven storage of light in a quantum well. *Phys. Rev. Lett.*, 78:4099, 1997.

[114] C. Rocke, O. Govorov, A. Wixforth, G. Böhm, and G. Weimann. Exciton ionization in a quantum well studied by surface acoustic waves. *Phys. Rev. B*, 57:R6850, 1998.

[115] D. Royer and E. Dieulesaint. *Elastic Waves in Solids.* Springer, Heidelberg, 2000.

[116] J. Rudolph, R. Hey, and P. V. Santos. Long-range exciton transport by dynamic strain fields in a GaAs quantum well. *Phys. Rev. Lett.*, 99: 047602, 2007.

[117] H. Sanada, S. Matsuzaka, K. Morita, C. Y. Hu, Y. Ohno, and H. Ohno. Hysteretic dynamic nuclear plarization in GaAs/Al$_x$Ga$_{1-x}$As (110) quantum wells. *Phys. Rev. B*, 68:241303(R), 2003.

[118] J. S. Sandhu, A. P. Heberle, J. J. Baumberg, and J. R. A. Cleaver. Gateable suppression of spin relaxation in semiconductors. *Phys. Rev. Lett.*, 86:2150, 2001.

[119] P. V. Santos, M. Ramsteiner, and F. Jungnickel. Spatially-resolved photoluminescence in GaAs surface acoustic wave structures. *Appl. Phys. Lett.*, 72:2099, 1998.

[120] P. V. Santos, F. Alsina, J. A. H. Stotz, R. Hey, S. Eshlaghi, and A. D. Wieck. Band mixing and ambipolar transport by surface acoustic waves in GaAs quantum wells. *Phys. Rev. B*, 69:155318, 2004.

[121] L. Schreiber, D. Duda, B. Beschoten, G. Güntherodt, H.-P. Schönherr, and J. Herfort. Anisotropic electron spin lifetime in (In,Ga)As/GaAs (110) quantum wells. *Phys. Rev. B*, 75:193304, 2007.

[122] E. Ya. Sherman. Random-spin-orbit coupling and spin relaxation in symmetric quantum wells. *Appl. Phys. Lett.*, 82:209, 2003.

[123] J M Shilton, D R Macey, V I Talyanskii, Yu Galperin, M Y Simmons, M Pepper, and D A Ritchie. On the acoustoelectric current in a one-dimensional channel. *J. Phys.: Condens. Matter*, 8:L337, 1996.

[124] V. Sih, R. C. Myers, Y. K. Kato, W. H. Lau, A. C. Gossard, and D. D. Awaschalom. Spatial imaging of the spin Hall effect and current-induced polarization in two-dimensional electron gases. *Nature Phys.*, 1:31, 2005.

[125] V. Sih, H. Knotz, J. Stephens, V. R. Horowitz, A. C. Gossard, and D. D. Awschalom. Mechanical control of spin-orbit splitting in GaAs and $In_{0.04}Ga_{0.96}As$ epilayers. *Phys. Rev. B*, 73:241316(R), 2006.

[126] S.H. Simon. Coupling of surface acoustic waves to a two-dimensional electron gas. *Phys. Rev. B*, 54:13878, 1996.

[127] Jairo Sinova, Dimitrie Culcer, Q. Niu, N. A. Sinitsyn, T. Jungwirth, and A. H. MacDonald. Universal intrinsic spin Hall effect. *Phys. Rev. Lett.*, 92(12):126603, 2004.

[128] C. P. Slichter. *Principles of Magnetic Resonance.* Springer-Verlag, Berlin, 1990.

[129] T. Sogawa, P. V. Santos, S. K. Zhang, S. Eshlaghi, A. D. Wieck, and K. H. Ploog. Transport and lifetime enhancement of photoexcited spins in GaAs by surface acoustic waves. *Phys. Rev. Lett.*, 87:276601, 2001.

[130] R. Stoneley. The propagation of surface elastic waves in a cubic crystal. *Proc. Roy. Soc. A*, 232:447, 1955.

[131] J. A. H. Stotz, R. Hey, P. V. Santos, and K. H. Ploog. Enhanced spin coherence via mesoscopic confinement during acoustically induced transport. *New J. Phys.*, 10:093013, 2008.

[132] James A. H. Stotz, Rudolph Hey, Paulo V. Santos, and K. H. Ploog. Coherent spin transport via dynamic quantum dots. *Nature Materials*, 4:585, 2005.

[133] D. Sun and E. Towe. Molecular beam epitaxial growth of (Al,Ga)As/GaAs heterostructures and Si doping characterization study on vicinal (110) GaAs substrates. *J. Cryst. Growth*, 132:166, 1993.

[134] D. Sun, E. Towe, P.H. Ostdiek, J.W. Grant, and G.J. Vansuch. Polarization control of vertical-cavity surface-emitting lasers through use of an anisotropic gain distribution in [110]-oriented strained quantum-well structures. *IEEE J. of Selected Topics in Quantum Electronics*, 1: 674, 1995.

[135] A. Tackeuchi, T. Kuroda, S. Muto, Y. Nishikawa, and O. Wada. Electron spin relaxation dynamics in GaAs/AlGaAs quantum wells and InGaAs/InP quantum wells. *Jpn. J. Appl. Phys.*, 38:4680, 1999.

[136] Y. Tanaka and S. Tamura. Surface acoustic waves in two-dimensional periodic elastic structures. *Phys. Rev. B*, 58:7958, 1998.

[137] W. J. Tanski, S. W. Merritt, R. N. Sacks, D. E. Cullen, E. J. Branciforte, R. D. Carroll, and T. C. Eschrich. Heterojunction acoustic charge transport devices on GaAs. *Appl. Phys. Lett.*, 52:18, 1987.

[138] E. S. Tok, T. S. Jones, J. H. Neave, J. Zhang, and B. A. Joyce. Is the arsenic incorporation kinetics important when growing GaAs(001), (110), and (111)A films? *Appl. Phys. Lett.*, 71:3278, 1997.

[139] W. I. Wang. Instabilities of (110) III-V compounds grown by molecular beam epitaxy. *J. Vac. Sci. Technol. B*, 1:630, 1983.

[140] C. P. Weber, J. Orenstein, B. Andrei Bernevig, Shou-Cheng Zhang, Jason Stephens, and D. D. Awschalom. Nondiffusive spin dynamics in a two-dimensional electron gas. *Phys. Rev. Lett.*, 98:076604, 2006.

[141] J. Z. Wilcox and R. E. Brooks. Time-fourier transform by a focusing array of phased surface acoustic wave transducers. *J. Appl. Phys.*, 58: 1148, 1985.

[142] J. Z. Wilcox and R. E. Brooks. Frequency-dependent beam steering by a focusing array of surface acoustic wave transducers: Experiment. *J. Appl. Phys.*, 58:1160, 1985.

[143] R. Williams. *Modern GaAs processing methods.* Artech House, Norwood, 1990.

[144] R. Winkler. *Spin-Orbit Coupling Effects in Two-Dimensional Electron and Hole Systems*, volume 191. Springer, Berlin, 2003.

[145] S. A. Wolf, D. D. Awschalom, R. A. Buhrman, J. M. Daughton, S. von Molna, M. L. Roukes, A. Y. Chtchelkanova, and D. M. Treger. Spintronics: a spin-based electronics vision for the future. *Science*, 294: 1488, 2001.

[146] S. L. Wright, W. Kroemer, and M. Inada. Molecular beam epitaxial growth of GaP on Si. *J. Appl. Phys.*, 55:2916, 1984.

[147] G. Yang, F. Iikawa, O. D. D. Couto, Jr., R. Hey, and P. V. Santos. Acoustically induced spin transport and manipulation in (110) GaAs quantum wells. *in preparation*, 2007.

[148] M. Yoshita, H. Akiyama, L. N. Pfeiffer, and K. W. West. Quantum wells with atomically smooth interfaces. *Appl. Phys. Lett.*, 81:49, 2002.

[149] P. Yu and M. Cardona. *Fundamentals of Semiconductors: Physics and Materials Properties.* Springer, Heidelberg, 1995.

[150] D. M. Zumbühl, J. B. Miller, C. M. Marcus, K. Campman, and A. C. Gossard. Spin-orbit coupling, antilocalization, and parallel magnetic fields in quantum dots. *Phys. Rev. Lett.*, 89:276803, 2002.

[151] I. Zutić, J. Fabian, and S. Das Sarma. Spintronics: Fundamentals and applications. *Rev. Mod. Phys.*, 76:323, 2004.

Appendix A

Parameters

A.1 Fundamental constants

Symbol	Value	Description
c	2.99792×10^{8} m/s	vacuum speed of light
e	1.60218×10^{-19} As	elementary charge
m	9.10939×10^{-31} kg	free electron mass
$\hbar$	1.05457×10^{-34} Js	Planck constant
k_B	1.38066×10^{-23} J/K	Boltzmann constant
μ_B	9.274×10^{-24} J/T	Bohr magneton

A.2 Material parameters for GaAs

Symbol	Value	Description
a_0	5.64 $\AA$	lattice constant [149]
m_0	0.067 m	electron effective mass [149]
m_0^h	0.45 m	hole effective mass [15]
E_g	1.516 eV (at 15 K)	band gap energy [16]
Δ_0	0.341 eV	spin orbit splitting of valence band [144]
a_{CB}	-9 eV	conduction band deformation potential [149]
a_{VB}	0.5 eV	valence band deformation potential [149]
b_{VB}	-2 eV	valence band uniaxial deformation potential [149]
C_3	0.8 eV$\AA$	spin splitting parameter in the presence of strain [125]
r	5.206 $e\AA^2$	Rashba coefficient [144]

Abbreviations

Abbreviation	Description
BAP	Bir-Aronov-Pikus
BEP	beam equivalent pressure
BIA	bulk inversion asymmetry
CB	conduction band
CW	continuum wave
DP	D'yakonov-Perel'
e-*h*	electron-hole
EY	Elliott-Yafet
hh	heavy hole
IDT	interdigital transducer
ISR	intersubband spin relaxation
lh	light hole
MBE	molecular beam epitaxy
MEE	migration enhanced epitaxy
NIA	native inversion asymmetry
NMR	nuclear magnetic resonance
PL	photoluminescence
QW	quantum well
SAW	surface acoustic wave
SIA	structural inversion asymmetry
SO	spin-orbit
TR	time-resolved
UHV	ultra high vacuum
VB	valence band

Acknowledgements

Firstly, I thank Prof. Ploog and Dr. Paulo Santos. I am really thankful for been given the opportunity to make part of your group at the Paul Drude Institute.

Thanks Dr. Hey, without whom nothing in this work would have been possible.

I also thank Profs. V. Bonačić-Koutecky, O. Benson, and W. Nolting from the Graduiertenkolleg.

Thanks Prof. Iikawa for the fruitful cooperation we have had along this time.

Thanks my many friends and colleagues at the Paul-Drude-Institute.

I would also like to thank my working group friends. In the lack of an objective criterium to list them, I chose the weight. So, firstly, thank you Maurício for the friendship and for nice working atmosphere you always brought us. Thank you James for the advises and for guiding me during my first steps into the lab. Thanks Jörg, for the friendship, but also of course for the "discussions". Pablo, maybe I thank you tomorrow! Thanks Markus, mainly for trying to teach skiing for a Brazilian. At least you had a lot of fun! Thanks also Herr Klaus, Hugo, Edgar, Esperanza (virtual group member), Shujie, and (E)Sne for the nice time we have had during these last months.

I would also like to thank some special persons, who have brought me a lot of happiness in the last three years. Thank you Lú, for been so important during this time. You're wonderful! Thanks Bia for making me laugh endlessly in order to keep my abdomen always in shape. Thank you Pedro, for the friendship and the very good time we had in Berlin.

There also some friends, who close or far way, I can't forget. Thank you Dupyckles, Dracena, David, Cris, Wagner, Chico, and Piccin.

Family, thank you. Thanks for supporting and encouraging me during

all this time we have been apart. Mae, pai, Wesley e Lívia, amo vocês.

Finally, why not, I would like to thank Germany for offering scientists one the best research infra-structures in the world, with the plus of serving them a marvelous beer.

Selbständigkeitserklärung

Hiermit erkläre ich, die vorliegende Arbeit selbständig ohne fremde Hilfe verfasst zu haben und nur die angegebene Literatur und Hilfsmittel verwendet zu haben.

Odilon D. D. Couto Jr.
26. Mai 2008